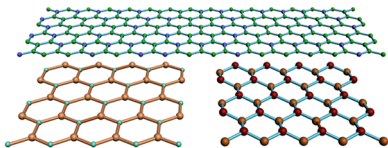


Graphene-Like Two-Dimensional Materials

Mingsheng Xu,* Tao Liang, Minmin Shi, and Hongzheng Chen

State Key Laboratory of Silicon Materials, MOE Key Laboratory of Macromolecular Synthesis and Functionalization, Department of Polymer Science and Engineering, Zhejiang University, Hangzhou 310027, People's Republic of China



CONTENTS

1. Introduction	3766
2. Hexagonal Boron Nitride Sheets	3767
2.1. Electronic and Magnetic Properties of Pristine <i>h</i> -BN Sheets	3767
2.2. Functionalization of <i>h</i> -BN Sheets	3768
2.3. Synthesis of <i>h</i> -BN Sheets	3769
3. Layered Transition Metal Dichalcogenides	3772
3.1. Electronic and Magnetic Properties of Pristine TMDs	3772
3.2. Strain Effect on the Electronic Properties of TMDs	3773
3.3. Functionalization of TMDs	3774
3.4. Monolayer and Few-Layer TMD FETs	3774
3.5. Synthesis of TMD Sheets	3776
3.6. Analysis of the Existence of Monolayer TMD Sheets	3778
4. Layered Group-IV and Group-III Metal Chalcogenides	3779
4.1. Structural and Electronic Properties of Layered Group-IV Metal Chalcogenides	3779
4.2. Synthesis of Layered Group-IV Metal Chalcogenides	3780
4.3. Structural and Electronic Properties of Layered Group-III Metal Chalcogenides	3781
4.4. Electronic Properties of Single Tetralayer GaSe	3782
4.5. Synthesis of Layered Group-III Metal Chalcogenides	3782
5. Van der Waals Epitaxy of Layered Metal Chalcogenides	3782
6. Silicene and Germanene	3783
6.1. Structural and Electronic Properties of Pristine Silicene and Germanene	3783
6.2. Functionalization of Silicene and Germanene	3785
6.3. Synthesis of Silicene Nanosheets	3785
7. Layered Binary Compounds of Group-IV Elements and Group III–V	3788
8. Valley Physics and Spin Effect in Monolayers of 2D Sheets	3788
8.1. Valley Physics in Monolayer TMDs	3788
8.2. Quantum Spin Hall Effect in Silicene and Germanene	3789
9. Concluding Remarks and Outlook	3790

Author Information	3791
Corresponding Author	3791
Notes	3791
Biographies	3791
Acknowledgments	3792
Abbreviations	3792
References	3792
Note Added in Proof	3798
Note Added after ASAP Publication	3798

1. INTRODUCTION

Graphene is composed of a single layer of carbon atoms arranged in a two-dimensional (2D) honeycomb lattice. It is a fundamental building block for a range of well-known carbon materials such as three-dimensional (3D) graphite, one-dimensional (1D) carbon nanotubes, and zero-dimensional (0D) fullerene. The identification of graphene among mechanically exfoliated graphite sheets and the subsequent discovery of its unusual electronic properties¹ have led to an extraordinary amount of interest from both academia and industry. Many extraordinary properties, such as its 2.3% absorption in the white light spectrum, high surface area, high Young's modulus, and excellent thermal conductivity, have all been reported. Because of its remarkable properties,^{2,3} applications using graphene in a wide range of areas, including high-speed electronic⁴ and optical devices,⁵ energy generation and storage,^{5–7} hybrid materials,^{8,9} chemical sensors,^{2,11} and even DNA sequencing,^{12–14} have all been explored. A variety of proof-of-concept devices have also been demonstrated.^{3a,15} However, pristine graphene itself is unlikely to be used for the fabrication of logical circuits operated at room temperature with low standby power dissipation because graphene has no band gap (E_g). The result is a small current on/off ratio in graphene field-effect transistors (FETs).¹⁶ The prerequisite for such applications is the mass production of graphene in a controlled manner because the number of graphene layers as well as the defects in these graphene layers significantly influence the subsequent transport properties. Methods such as mechanical exfoliation, liquid-phase exfoliation, reduction of graphene oxide, chemical vapor deposition (CVD), surface segregation,¹⁷ and molecular beam epitaxy (MBE)¹⁸ have been developed in order to make suitable graphene layers. Despite these efforts, the fine control of the number and structure of graphene sheets over an entire substrate remains a major challenge.¹⁹ Hence the search to optimize the manufacturing process with a view to the realization of distinct properties of graphene layers is ongoing. Another important challenge pertaining to graphene applica-

Received: July 1, 2012

Published: January 3, 2013



tions in optoelectronics is its integration into the current Si-based technology.

Since the discovery of the exotic properties of graphene, 2D layered materials such as metal chalcogenides, transition metal oxides, and other 2D compounds have gained renewed interest. Transition metal dichalcogenides (TMDs) consist of hexagonal layers of metal atoms (M) sandwiched between two layers of chalcogen atoms (X) with a MX₂ stoichiometry. Depending on the combination of chalcogen (typically S, Se, or Te) and transition metal (typically Mo, W, Nb, Re, Ni, or V),²⁰ TMDs occur in more than 40 different categories. Together with layered transition oxides²¹ such as MoO₃ and La₂CuO₄,²² insulator hexagonal boron nitride (*h*-BN),²³ and topological insulators of Bi₂Te₃, Sb₂Se₃, and Bi₂Se₃,^{24,25} the common feature of these layered materials is that the bulk 3D crystals are stacked structures. They involve van der Waals interactions between adjacent sheets with strong covalent bonding within each sheet. Such materials span the entire range of electronic structures, from insulator to metal, and display interesting properties. These include the topological insulator effect,^{26,27} superconductivity,²⁸ and thermoelectricity.²⁹ Furthermore, a strong interest in group-IV graphene-like 2D buckled nanosheets has recently emerged. Silicene and germanene, the silicon- or germanium-based counterparts of graphene, have progressed from theoretical predictions³⁰ to experimental observations³¹ in only a few years. They are found to exhibit electronic characteristics similar to graphene.³²

Because of their distinct properties and high specific surface areas, these 2D materials are important in various applications such as optoelectronics, spintronics, catalysts, chemical and biological sensors, supercapacitors, solar cells, and lithium ion batteries. Previous research has shown that the field-effect mobility of graphene transistors built on mechanically exfoliated *h*-BN and gated by a thin top *h*-BN dielectric layer have a comparable mobility to suspended graphene. This is attributed to an ultraflat and charged impurity-free *h*-BN surface.³³ In contrast to the zero band gap of pristine graphene itself and the band gaps (a few hundred meV) introduced in bilayer graphene and in complexly processed graphene nanoribbons, a single-layer MoS₂ sheet is a direct band gap semiconductor. The result is that MoS₂ is a promising material that has the potential to be incorporated into digital circuits³⁴ and light-emitting diodes.³⁵ For instance, the current on/off ratio of single-layer MoS₂ transistors exceeds 10⁸ at room temperature.³⁶ This is much higher than that (approximately 100) of graphene transistors.³⁷ Indeed graphene-like silicene-based technologies might have the major advantage of easy integration into existing circuitry because Si is currently the basis of most of the electronics industry. Although diverse types of semiconductor devices with individual 1D structures are possible, their practical application in high-yield, scalable systems faces formidable engineering challenges with respect to assembly and other aspects of the manufacturing process because they come with different diameters, different lengths, and even different electronic properties. Using 2D sheets would avoid these limitations, because 2D geometries are directly compatible with established device designs and processing approaches already used in the semiconductor industry. 2D sheets with finite-size and quantum characteristics in their electronic and optical properties can be made both uniformly and reproducible in size and thickness by many methods currently used in conventional material synthesis.

Some remarkable changes in the electronic properties of layered materials as their thickness is reduced down to single or only a few layers are common among these 2D layered crystals based on the known study. Recognizing the uniqueness of the 2D structure, one may expect that such materials will reveal new and unexpected properties providing a number of innovative opportunities. In this comprehensive review, the present status of graphene-like 2D materials, which is a fairly new field, will be discussed by focusing on theoretical and experimental studies of their structural and electronic properties reported to date. In order to keep this review concise, we restrict ourselves to 2D nonoxide materials and will not cover nanomembranes³⁸ and other dimensional nanostructures.^{39,40} There are reviews that solely address silicon nanostructures including silicene,^{41–43} layered oxides,²¹ and boron nitride nanomaterials including *h*-BN nanosheets.²³ We hope to cover not only the latest understanding of silicene and *h*-BN sheets but also metal chalcogenides sheets, other group-IV graphene-like 2D element sheets and their honeycomb binary compounds, as well as the honeycomb group III–V binary compounds. Nanoribbons with 2D structures also lie outside the scope of this review. Instead, we focus on the major progress and advantages common to 2D sheets. Since there are many relevant studies^{7–9,11,12,14,19,44–49} by our own research group, we also present the purpose and significance of the development of such 2D materials. There will be a special emphasis on the electronic properties of the pristine and chemically functionalized monolayer, bilayer, and multilayer sheets of graphene-like 2D systems as well as the latest synthetic achievements for producing 2D nanosheets. To the best of our knowledge there are only a few reports on other properties such as mechanical^{50,51} of these 2D materials. Clearly it is the unique electronic properties of graphene that are in fact stimulating the discovery of its other extraordinary properties. Notably absent in graphene itself, the valley physics and quantum spin Hall effects found in 2D monolayer sheets will be highlighted. Finally, we will also address future directions yet to be explored for novel 2D materials intended for various practical applications as well as more basic research investigating their fundamentally distinct properties.

2. HEXAGONAL BORON NITRIDE SHEETS

2.1. Electronic and Magnetic Properties of Pristine *h*-BN Sheets

Boron nitride has been found to consist of a similar structural lattice as that found for the carbons of graphene in that it consists of equal numbers of boron and nitrogen atoms. Sheets of *h*-BN are composed of alternating boron and nitrogen atoms in a honeycomb arrangement consisting of sp²-bonded 2D layers (see Figure 1a). This structure means that *h*-BN powder is traditionally used as a lubricant. The pristine BN sheets are intrinsically insulators or wide band gap semiconductors (approximately 5.9 eV).⁵² Because of its good electrical insulation property, *h*-BN has been applied as a charge leakage barrier layer for use in electronic equipment. It also shows far ultraviolet light emission, which can be possibly attributed to the direct wide band gap.

Recently, 2D *h*-BN sheets are attracting a great deal of attention not only because of the popularity of graphene technologies but also their superb chemical stability and intrinsic insulation. The use of *h*-BN thin films as a thin top dielectric layer to gate graphene and as an inert flat substrate for

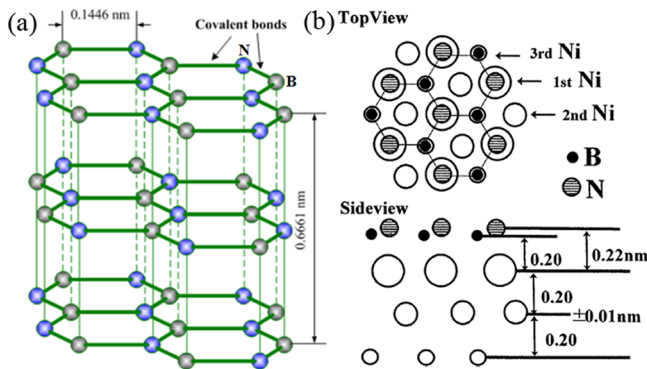


Figure 1. (a) Structure of *h*-BN layers. (b) Atomic structure of monolayer *h*-BN on Ni(111) substrate with a commensurate (1×1) periodicity revealed by LEED intensity analysis. Reproduced with permission from ref 100. Copyright 1997 American Physical Society.

graphene transistors has been shown to significantly improve device performance.⁵³ The use of high-quality graphene in a BN-graphene-BN sandwich, which was attached to a substrate and topped with a second graphene layer, was reported to be insulating.⁵³ In such a configuration, the second graphene layer screens the electron–hole puddles⁵⁴ in the sandwiched graphene. This causes the puddles to be much shallower and transforms the other graphene layer into an insulator. With a similar lattice constant to graphene and the same hexagonal structure, *h*-BN offers one of the best and most advanced platforms for future graphene electronics by enhancing the graphene stability and quality.

In general, both charged impurities and disorder induced by high-*k* dielectrics can degrade the field-effect mobility and other properties of FETs, and control of the thickness and uniformity of an ultrathin gate dielectric layer is particularly important for their reliability and long-term stability. Although the band gap (approximately 5.9 eV) of single and few-layer *h*-BN sheets is similar to that of bulk *h*-BN single crystals, the breakdown voltage of *h*-BN sheets depends on the number and the crystalline nature of *h*-BN layers. Using conductive atomic force microscopy,^{55,56} Lee et al. studied the breakdown behaviors of *h*-BN sheets as a function of the number of layers.⁵⁷ Low-bias conductance was observed on the mono-, bi-, and trilayer *h*-BN samples due to direct tunneling, whereas thicker samples were insulating at low bias.⁵⁷ At high bias, Fowler-Nordheim tunneling was found to occur for all the samples. A barrier height for tunneling of approximately 3.07 eV and a dielectric breakdown strength of approximately 7.95 MV/cm of the *h*-BN sheets were obtained. These values are comparable to SiO₂, whose barrier height is approximately 3.25 eV and its breakdown strength is 8–10 MV/cm. Furthermore, the tunneling current map showed uniformity across micrometer scale areas. This clearly indicates that high-quality *h*-BN layers, with an absence of pinholes and defects, can easily be obtained for use in ultrathin insulators and gate dielectrics. Such a defect-free *h*-BN dielectric with a high breakdown field also offers potential for use in field-effect tunneling transistors.⁵⁸

2.2. Functionalization of *h*-BN Sheets

The chemical functionalization of graphene has been extensively explored with a view to tuning the band gap of graphene. Graphane is a stoichiometric derivative of graphene with a hydrogen atom attached to each carbon. This changes the hybridization of the carbon atoms from sp² to sp³, and the

result is an insulator with a band gap of approximately 3.43 eV.^{59,60} When half of hydrogens in a graphane sheet are removed, the resulting semihydrogenated graphene, called graphone, becomes a ferromagnetic semiconductor with an indirect band gap of approximately 0.46 eV.⁶¹ This value is much smaller than 2.79 eV, which is the value for a chairlike graphane reported by Kharche et al.⁶² They carried out a theoretical study of the effect on the band gap of graphone caused by using *h*-BN as the supporting substrate. However, the hydrogenation of graphene is reversible, and this results in an unstable material.^{60,63} Fluorographene is a more stable graphene derivative with a fluorine atom attached to each carbon, which is analogous to Teflon. Fluorographene is a high-quality insulator with an optical gap of 3.0 eV.⁶⁴ The studies described above have stimulated strong interest in the functionalization of *h*-BN sheets and other 2D materials.

Bulk *h*-BN itself is an insulator with a direct band gap of 5.97 eV.⁵² The optical band gap of a single-layer *h*-BN sheet synthesized on Cu foil by the CVD method was found to be approximately 6.07 eV (Table 1). This is slightly larger than the

Table 1. Summary of the Band Gaps of Typical Layered TMDs and *h*-BN Materials

2D sheets	theoretical E _g (eV)	experimental E _g (eV)
graphene	0	0
bilayer graphene	0	0
bulk <i>h</i> -BN		5.97 [ref 52]
monolayer <i>h</i> -BN		6.07 [ref 65]
fully hydrogenized <i>h</i> -BN	3.05 [ref 66]	
2–5 layers <i>h</i> -BN		5.92 [ref 105.]
bulk MoS ₂	1.20 (indirect ^b) [refs 35, 139]	1.0–1.29 (indirect) [refs 35, 139]
monolayer MoS ₂ ^a	~1.90 (direct ^b) [ref 140]	~1.90 (direct) [ref 140]
bulk WS ₂	~1.30 (indirect ^b) [refs 35, 147]	~1.35 (indirect) [refs 35, 147]
monolayer WS ₂ ^a	~2.10 (direct ^b) [ref 147] ~1.80 (direct ^c) [ref 148]	
monolayer MoSe ₂	~1.44 (direct ^c) [ref 148]	
monolayer MoTe ₂	~1.07 (direct ^c) [ref 148]	

^aBilayer MoS₂ and WS₂ are indirect band gap semiconductors.^{150,151}

^bFirst-principles calculations were performed on the basis of density functional theory (DFT) as implemented in the CRYSTAL09 code. The exchange and correction terms were described using general gradient approximation (GGA) in the scheme of PBE (Perdew–Burke–Ernzerhof). ^cSpin-polarized DFT.

value for the bulk and few-layer *h*-BN because of the absence of interlayer coupling.⁶⁵ First-principles computational studies showed that the most stable fully hydrogenated monolayer of a BN sheet prefers to adopt a regular chairlike structure with the hydrogen atoms linked to the B atoms on one side and the other hydrogen atoms linked to the N atoms on the other side.⁶⁶ Both the B and N atoms in the fully hydrogenated BN single layer have typical sp³ hybridization, and density functional theory (DFT) calculations showed that the 2D fully hydrogenated BN single layer is an insulator with a direct band gap of approximately 3.05 eV.⁶⁶

In order to modulate the electronic properties of BN sheets, Ataca et al.⁶⁷ used first-principles plane-wave calculations to investigate the structural, electronic, and magnetic properties of *h*-BN sheets functionalized by adatom adsorption and the effects of substituting other atoms for the B and N atoms. Of

the many atoms considered, such as Sc, Ti, V, Cr, Mn, Fe, Mo, W, Pt, H, C, Si, B, N, O, Ca, Cu, Pd, Ni, and Zn, results indicate that Cr, Mn, Mo, W, H, N, Ca, and Zn cannot in fact bind to a 2D BN sheet. At high coverage of specific adatoms, the insulating bare BN monolayer can be tuned to have a magnetic metallic or half-metallic ground state. One remarkable observation is that when B or C is on 2D BN sheets, they undergo a (4 × 4) reconstruction and have a band gap smaller than the parent 2D BN. Oxygen-covered 2D BN was found to be a ferromagnetic metal and a small band gap semiconductor. At low coverage, the bands associated with the adsorbed atoms are flat, and the band structure of the parent BN was not affected significantly. DFT computation results predicted that charge transfer can occur between the BN sheets and either an acceptor (tetracyanoquinodimethane, TCNQ) or a donor (tetraphiafulvalene, TTF).⁶⁸ The charge transfer between the BN sheets and the TCNQ or TTF was found to significantly reduce the band gap of the BN sheets and resulted in a *p*- or *n*-type semiconductor, respectively.

Boron–carbon–nitrogen (B–C–N) layers have band gaps and electronic properties that are intermediate between those of pure graphene and *h*-BN. Separation into either graphene islands in a planar BN matrix⁶⁹ or BN islands in a graphene matrix⁷⁰ was observed in the B–N–C layers depending on the B–N–C stoichiometry. It was experimentally determined that the electron-beam-induced substitutional carbon doping preferably occurred at the defective sites and caused the insulating BN sheets to become conducting.⁷¹

As well as the interest in introducing a band gap in graphene by nanoribbon engineering, there is also great interest in the electronic and magnetic properties of bare,⁷² hydrogenated,⁶⁶ or hydrogen-terminated^{72,73} BN nanoribbons. Here the electronic and magnetic properties of the zigzag BN nanoribbons can be modulated by controlling the hydrogenation ratio. However, controlling the formation of the nanoribbons is quite complicated.

2.3. Synthesis of *h*-BN Sheets

Mechanical and liquid-phase exfoliations are two common methods used to separate individual sheets from stacked 2D layered crystals by breaking the weak van der Waals bonds between the layers. Mechanical exfoliation can result in sheets with perfectly crystalline structures,⁷⁴ and therefore the sheets produced by this method are used to explore the intrinsic properties of the materials. However, the yield from mechanical exfoliation is very low. To produce BN nanosheets based on mechanical peeling on a large scale, Li et al. tailored ball-milling conditions to generate a gentle shear force.⁷⁵ Using benzyl benzoate as the milling agent, *h*-BN nanosheets with a lateral size of hundreds of nanometers and a thickness of a few nanometers were obtained. Despite the high efficiency, the ball-milling causes point defects in the BN atomic planes and introduces impurities. The defects introduced into the BN sheets, however, can improve the reaction efficiency of the resulting BN sheets by the presence of the organic molecules. For instance, Lin et al. functionalized *h*-BN sheets, which were generated by ball-milling, with a long alkyl chain amine *via* Lewis acid–base interactions between the amino groups and the boron atoms of *h*-BN.⁷⁶

Liquid-phase exfoliation creates dispersions of 2D layered materials in various solvents or aqueous surfactant solutions with the assistance of sonication. Here sonication results in the exfoliation of the layered crystals into single-layer and

multilayer sheets stabilized by interactions with the solvent or a surfactant. Such dispersion can easily form films by vacuum filtration with thicknesses that range from nanometers to tens of micrometers. Compared with mechanical exfoliation, solution-based exfoliation is an efficient method for producing large quantities of layered materials.^{77–79} Although it should be noted that control of the number of layers and the lateral size is difficult, such liquid exfoliation methods also allow easy functionalization of the individual sheets^{8,80} and the formation of novel composite materials.^{77,78,81}

Han et al.⁸² chemically exfoliated *h*-BN crystals into few-layer *h*-BN sheets. During their preparation, the *h*-BN crystals were sonicated in a 1,2-dichloroethane solution of poly(*m*-phenylenevinylene-co-2,5-dicetoxy-*p*-phenylenevinylene) for 1 h to disperse and break up the *h*-BN crystals. The layer number of the resultant *h*-BN sheets was determined by transmission electron microscopy (TEM), and no monolayer *h*-BN sheets were obtained. The authors suggested that the duration of sonication is an important factor that requires optimization for the yield and for minimization of any damage of the *h*-BN sheets produced. The solvent 1,2-dichloroethane was used to generate few-layer *h*-BN sheets with micrometer-sized dimensions.⁸³ The advantage of using this solvent over other solvents, such as *N,N*-dimethylformamide (DMF), for the chemical exfoliation of *h*-BN is its lower boiling point, which allows rapid and simple removal of the solvent.

Zhi et al. used the strong polar solvent such DMF to exfoliate *h*-BN microsized particles. The *h*-BN powder was sonicated for 10 h and then centrifuged at 5000–8000 rpm to remove residual large BN particles. The number of layers for the *h*-BN sheets generated was generally four, but other numbers were produced as well.⁸⁴ Taking the low yield of the DMF-based exfoliation of *h*-BN into consideration, Wang et al. used methanesulfonic acid (MSA) as the solvent to exfoliate *h*-BN.⁸¹ This process resulted in *h*-BN sheets with thicknesses less than 3 nm, and the yield of MSA-based exfoliation was approximately 10 times greater than that found for the DMF-based exfoliation yield.

Lin et al.⁸⁵ found that using lipophilic or hydrophilic amine molecules can simultaneously functionalize and exfoliate *h*-BN into few-layer *h*-BN sheets. Octadecylamine (ODA) and an amine-terminated polyethylene glycol (PEG, *O,O'*-bis(3-aminopropyl)polyethylene glycol) were used as Lewis bases during the functionalization and exfoliation procedures. The mixture of *h*-BN powder with ODA or PEG was heated to between 160 and 180 °C for 4–6 days. After cooling, tetrahydrofuran (THF) was added to the ODA solution or water was added to the PEG solution, and then the solution was briefly sonicated. After centrifugation, few-layer (3–20 layers) ODA-BN or PEG-BN sheets could be successfully collected from the supernatants. The functionalization was found to have little effect on the electronic properties of the BN sheets.⁸⁵ Furthermore, Lin et al. exfoliated *h*-BN in deionized water using a bath sonicator for 8 h. The process resulted in the presence of monolayer *h*-BN sheets with lateral sizes of 200 nm or less. These were different from the few-layer *h*-BN sheets with lateral sizes larger than 200 nm produced by exfoliation with DMF. This comparison indicates that in addition to the sonication-assisted solvent polarity effect, the hydrolysis of *h*-BN under sonication participates in the exfoliation and is the main cause of the formation of small but monolayers of the *h*-BN sheets.⁸⁶

In addition to the above solution-based exfoliation, wet chemical reactions were also explored as a means to synthesize *h*-BN sheets. For instance, Nag et al.⁸⁷ synthesized few-layer BN sheets using the reaction between boric acid with urea at 900 °C under an N₂ atmosphere. The resultant BN sheets exhibited high CO₂ adsorption but negligible H₂ adsorption.

In contrast with either the exfoliation methods or wet chemical reactions, in which control of the layer number and the lateral size of *h*-BN sheets is difficult, a dry CVD method has also been extensively explored. The aim was to synthesize 2D layered materials on a large scale^{88,89} with the promise of fine control over the number of layers and the crystalline structures. Prior to the present intense interest in *h*-BN sheets, there have been many reports of the synthesis of *h*-BN thin films using various precursors based on CVD methods. Independent boron and nitrogen precursors such as BF₃/NH₃,⁹⁰ BCl₃/NH₃,⁹¹ and B₂H₆/NH₃⁹² were used to synthesize *h*-BN layers. In such systems, control of the ratio between the boron source and NH₃ is critical for obtaining stoichiometric *h*-BN layers. A single precursor such as borazine (B₃N₃H₆),⁹³ hexachloroborazine (B₃N₃Cl₆),⁹⁴ or trichloroborazine (B₃N₃H₃Cl₃)^{95,96} has the advantage of having a 1:1 B/N stoichiometry for the synthesis of an *h*-BN thin film *via* pyrolysis of the precursor.

Monolayer *h*-BN sheets were synthesized on single crystal Ru(001),⁹⁷ Ni(111), Pd(111), and Pt(111)^{98,99} substrates by a CVD method using borazine as the precursor. Prior to the growth, the substrate was mechanically polished and then cleaned in an ultrahigh vacuum (UHV) by Ar ion sputtering and annealing at approximately 800 °C. Borazine gas was introduced into the chamber and decomposed on the substrate at 700–800 °C to form a monolayer *h*-BN. The growth rate of additional layers on the first monolayer of *h*-BN by the thermal decomposition of borazine is extremely small because of the strong reduction reaction on the surface.^{97,98} The growth of BN did not proceed in a layer-by-layer fashion after the formation of the first monolayer but grew according to the Stranski-Krastanov mode. This is the preferred method for the synthesis of monolayer *h*-BN sheets. As revealed by low-energy electron-diffraction (LEED), the N atoms are located on top of the outmost Ni atoms, and the B atoms occupy face-centered cubic adsorption sites of the Ni(111) (Figure 1b). This indicates weak corrugation¹⁰⁰ in the commensurate monolayer *h*-BN on the Ni(111) surface. Although the bonding of monolayer *h*-BN with the Ni(111) surface is relatively strong compared to the bonding between *h*-BN on the Pd(111) or Pt(111), the interaction between the *h*-BN and the three substrates (Ni(111), Pd(111), and Pt(111)) is much weaker compared to the interaction between graphene and the substrates. The difference between *h*-BN and graphene originates from their different electronic structures. The B and N electronic states do not contribute to the Fermi sea of the substrate surface, and the monolayer *h*-BN remains an insulator.⁹⁹ In contrast with the formation of *h*-BN nanomeshes on Rh(111),¹⁰¹ the three substrates do not facilitate the formation of the BN nanomesh. Morscher et al.¹⁰² synthesized *h*-BN on both single crystal and thin-film Pd(111) substrates by the CVD method. Moiré patterns of the monolayer *h*-BN on the substrates were observed, and these were attributable to comparable lattice mismatch (approximately 9%) between the *h*-BN and Pd(111). However, it was found that the *h*-BN sheets on the single crystal and the film substrates have no obvious structural differences. In addition, Cavar et al. found that the

nucleation and growth of *h*-BN on Pt(111) are strongly dependent on the atmospheric pressure of the borazine.¹⁰³

Hexagonal BN films with thicknesses between 5 and 50 nm were synthesized on polycrystalline Ni films in an ambient pressure CVD system.¹⁰⁴ The process involved borazine vapor being carried by N₂ gas, introduced to the substrate and dehydrogenated in the temperature range from 400 to 700 °C. This was followed by a postannealing process at 1000 °C. The optical band gap of the resultant 5 nm thick *h*-BN films was found to be 5.92 eV. This is similar to the results for the synthesis of graphene on Cu foil. Here *h*-BN films consisting of 2–5 layers were prepared on Cu foil using ammonia borane (NH₃–BH₃) as the precursor.¹⁰⁵ It was sublimated at approximately 120 °C and then delivered onto a 25 μm thick Cu foil at 1000 °C using an Ar/H₂ gas flow. The resultant *h*-BN films showed an optical band gap of 5.5 eV and a 2D elastic modulus in the range of 200 to 500 N/m. By optimizing the growth parameters of such a surface-mediated process, it is possible to synthesize single-layer *h*-BN on Cu foils.⁶⁴ The optical band gap of the monolayer *h*-BN was determined to be 6.07 eV. Taking into consideration the higher air and moisture stability of decaborane (B₁₀H₁₄) with respect to borazine, Chatterjee et al.¹⁰⁶ chose decaborane/ammonia as the precursors for the synthesis of BN films on Ni and Cu foils using the CVD method. The thickness of the BN films on Ni and Cu foils was approximately 2 nm and 4–6 nm, respectively. In the absence of a metallic catalyst, Qin et al.¹⁰⁷ successfully synthesized BN sheets on a Si substrate using a microwave plasma CVD from a BF₃–H₂–N₂ gas mixture. The growth of the BN sheets on the substrate was attributed to the etching effect of the fluorine-containing BF₃. By using metal organic chemical vapor deposition with triethylboron and ammonia as the B and N precursors and with biscyclopentadienyl-magnesium as a Mg dopant, Mg-doped *h*-BN layers were synthesized on a 20 nm thick BN buffer layer that was deposited on a sapphire substrate.¹⁰⁸ The Mg-doped *h*-BN epitaxial layer showed *p*-type semiconducting behavior with a Hall mobility of approximately 0.5 cm²/(V s) and a hole concentration of approximately 1.1 × 10¹⁸ cm⁻³.

It has been reported that low precursor pressure¹⁰⁹ and hydrogen partial pressure¹¹⁰ in the CVD process are two key factors for growing large-area graphene domains. Sutter et al.¹¹¹ investigated the influence of such factors on the growth of *h*-BN on a Ru(0001) surface using borazine as the precursor. Low-energy electron microscopy (LEEM) was used to show that at low precursor pressure, individual *h*-BN domains nucleated sparsely and grew to large sizes of tens of micrometers. The addition of hydrogen was found to reduce the *h*-BN nucleation density and growth rate. Furthermore, atomic H was found to etch the *h*-BN edges and lead to the disappearance of *h*-BN.

Surface segregation like the CVD method is another feasible method for the large-scale synthesis of graphene. It has the potential to control the number of graphene layers^{19,112} and hence was also used to synthesize *h*-BN layers.¹¹³ Recently, we obtained triangular *h*-BN sheets (as shown in Figure 2) on a polycrystalline Fe–Cr–Ni alloy predoped with B and N *via* simple surface segregation.⁴⁸ The doped Fe–Cr–Ni alloy was heated at 1000 °C for 5 min in an UHV chamber, and then the sample was cooled to room temperature by turning off the power supply. We found the formation of monolayer and few-layer *h*-BN sheets *via* an intermediate B–N–S layer based on the line shape of the N KLL Auger electron and the presence of

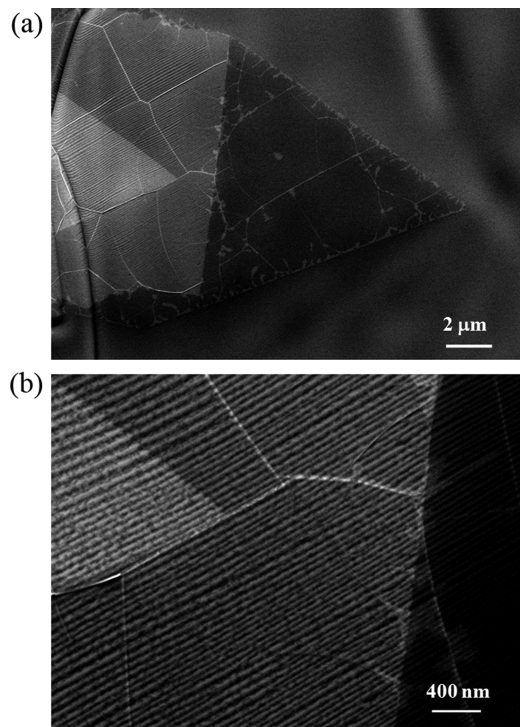


Figure 2. Typical scanning electron microscopy (SEM) image of triangle *h*-BN sheets synthesized by surface segregation from Fe–Cr–Ni alloy predoped with B and N. Waveline-like morphology may result from the substrate. Image (b) is a zoom-in image from (a).

S atoms in the layer. We believe that it is possible to control the *h*-BN coverage on the substrate by optimizing the growth parameters. In an extended study of surface segregation by Suzuki et al., they obtained even more uniform ultrathin *h*-BN films.¹¹⁴ In their study, an amorphous BN layer (30 nm) as boron and nitrogen source was sandwiched between a polycrystalline metal (Co or Ni) layer and the SiO₂ substrate. After the sample was heated in a vacuum (approximately 1 ×

10^{−4} Pa) at approximately 930 °C for 10–30 min and then cooling it down, atomically thin *h*-BN films were formed on both the top and bottom surface of the metal layer. Because the CVD growth of *h*-BN films unusually involves explosive and toxic chemical and gases, this kind of surface segregation approach is much simpler and safe.

Layers of *h*-BN are reported to be a superior platform for graphene transistors. Hence research efforts are currently focused on methods of directly synthesizing graphene on *h*-BN substrates. For example, few-layer graphene¹¹⁵ or graphene with single-layer coverage up to 90% was grown on mechanically exfoliated *h*-BN layers.¹¹⁶ It was found that *h*-BN films could also grow on mechanically exfoliated graphene using the CVD method.¹¹⁵ However, it should be noted that the uniformity and the structure of the layers need to be improved.

The interest in *h*-BN as a promising substrate for high-quality graphene electronics lies in its atomically smooth surface that is relatively free of dangling bonds and charge traps. Thus, the crystal quality and homogeneity rather than the number of *h*-BN layers is more critical for practical applications. Lee et al. investigated the effect of the surface morphology of Cu foils on the structural homogeneity of *h*-BN sheets synthesized by the CVD process.¹¹⁷ They found that thermal annealing and chemical polishing of the Cu foil can lead to an increase in grain size and surface flatness of the Cu substrate. This in turn resulted in a reduction in the amount of allotropes (amorphous BN and cubic BN) and impurities found in the synthesized *h*-BN sheets. In a typical process, the Cu foils were first annealed at 1020 °C for 2 h in an Ar atmosphere to increase the grain size of the Cu foils. They were then rubbed with a Cu etchant (Transent, type 1) to smoothen the surface of the Cu foils. The mobility and the on/off current ratio of the graphene transistors built on such synthesized *h*-BN sheets with 6–8 atomic layers was increased 3 times and 2 times, respectively, as compared to that without the *h*-BN sheets.

Graphene now is attracting great interest in ultrafast and inexpensive DNA sequencing. The using of graphene may

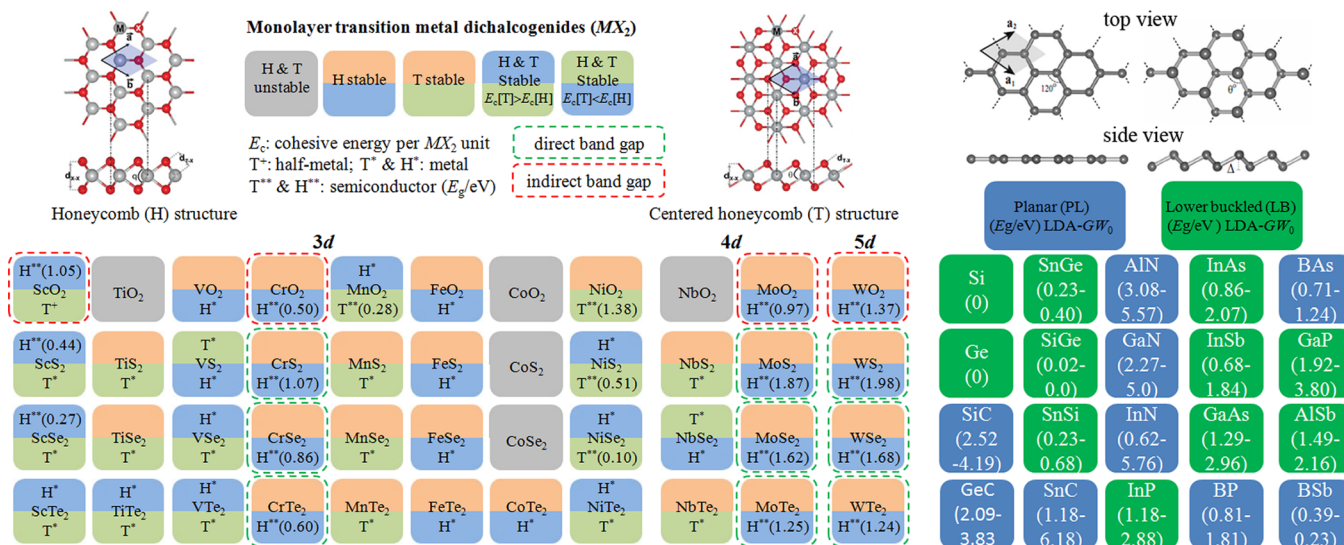


Figure 3. Summary of stability analysis and semiconducting properties of 44 different MX₂ compounds and binary compounds of group-IV elements and group III–V. Transition metal atoms indicated by M are divided into 3d, 4d, and 5d groups. MX₂ compounds shaded light gray form neither stable H (2H-MX₂) nor T (1T-MX₂) structure. In each box, the lower-lying structure (H or T) is the ground state. The resulting structures (T or H) can be half-metallic (+), metallic (*), or semiconducting (***) with direct or indirect band gaps.

achieve single-base resolution in electronic DNA sequencing due to the atomic thickness of the graphene plane as well as its ultrasensitivity to conductance change.^{12–14} This idea was proposed in 2009 by Xu et al.,¹² and later numerical simulations revealed that graphene-based nanopores of approximately 1.0–1.6 nm can rapidly read out sequences of individual DNA molecules with 100% accuracy.^{118,119} Nanopore-based DNA sequencing technologies may soon allow the entire DNA sequence to be read in one go, rather than cut apart, deciphered in brief fragments, and painstakingly reassembled.¹²⁰ It has been shown that the ionic current passing through the graphene nanopores is sensitive to the nanopore diameter.¹²¹ Surely, it could be argued that the detection of ionic current blockade based on the nanopores is much simpler than the detection of the tunneling current of the bases in a DNA strand using conducting probes.^{122,123} Taking into consideration the $\pi-\pi$ interaction of the DNA molecules with the graphene plane¹²⁴ and the edge effect,¹²⁵ we are now exploring *h*-BN nanopores for DNA sequencing based on an *ionic current blockade strategy* by using a monolayer thickness of 0.34 nm, and the inert, insulating, and flat properties of *h*-BN. In principle, all layered 2D sheets could be exploited for DNA sequencing if the thickness of the monolayer, bilayer, or few-layer of the 2D layers matches the resolution as well as other requirements.

3. LAYERED TRANSITION METAL DICHALCOGENIDES

3.1. Electronic and Magnetic Properties of Pristine TMDs

3D MX₂ compounds constitute one of the most interesting classes of materials. They display a wide range of important properties such as semiconductivity, half-metallic magnetism,¹²⁶ superconductivity,¹²⁷ or charge density wave,¹²⁸ as well as having applications in various areas including lubrication,¹²⁹ catalysis,¹³⁰ photovoltaics,¹³¹ supercapacitors,¹³² and rechargeable battery systems.^{133,134} Layered TMD crystals have two hexagonal lattices of MX₂ sandwiches which depend on the coordination of the transition metal atom by the chalcogens.²⁰ In 2H-MX₂, the coordination (honeycombs) is trigonal prismatic with a D_{3h} point group symmetry and the coordination in 1T-MX₂ is octahedral (centered honeycombs) with a C_{3v} symmetry¹³⁵ (see Figure 3).

Depending on the coordination and oxidation state of the metal atoms, layered TMDs can be semiconducting (e.g., M = Mo, W) or metallic (e.g., M = Nb, Re). MoS₂ is one such prototypical TMD material. Unlike graphite and *h*-BN, the layers of MoS₂ are made up of hexagons with the Mo and S₂ atoms located at alternating corners (Figure 4). MoS₂ is

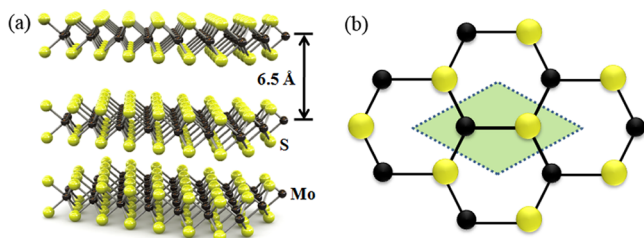


Figure 4. (a) The atomic structure of layered MoS₂. Different sheets of MoS₂ are composed of three atomic layers S–Mo–S, where Mo and S are covalently bonded. Reproduced with permission from ref 36. Copyright 2011 Nature Publishing Group. (b) A top view of the honeycomb lattice, emphasizing the inversion symmetry breaking.

important for dry lubrication, as a hydrodesulfurization catalyst used to remove sulfur compounds from oil,¹³⁶ and for hydrogen evolution.^{137,138} Because of its strong absorption in the solar spectral region, bulk MoS₂ has also attracted interest for its use in photovoltaic¹³⁹ and photocatalytic¹⁴⁰ materials. The quantum confinement effect on the electronic structures and optical properties were previously observed in MoS₂ nanoplates¹⁴¹ and nanotubes.¹⁴² The most striking feature of MoS₂ that is different from zero band gap graphene and insulating *h*-BN is that bulk MoS₂ is a semiconductor with an indirect band gap of 1.29 eV.¹⁴³

Several studies^{35,144,145} have confirmed a transition from an indirect band gap ($E_g = 1.29$ eV) to a direct band gap ($E_g = 1.90$ eV) for the MoS₂ material as the thickness of the MoS₂ decreased to a monolayer (Table 1). This accounts for more than a 10⁴-fold enhancement of the photoluminescence (PL) quantum yield observed in monolayer MoS₂ (Figure 5a). The unusual electronic structure of monolayer and few-layer MoS₂ and the resulting unique optical properties originate from characteristics of the d-electron orbitals that comprise the conduction and valence bands of MoS₂.^{35,144} The valence maximum at the Γ point shifts downward to the K point of the Brillouin zone as the number of layers decreases to a monolayer (Figure 5b). However, structural changes in the chemically exfoliated MoS₂ thin films (<5 nm) induced by Li intercalation during chemical exfoliation caused the PL to disappear. However, the PL was restored after the thin films were thermally annealed.^{146a} The observed thermal effect is beyond the scope of classic temperature-dependent PL behavior of semiconductors.

In general, the intensity of PL of semiconductors decreases as the PL peak broadens with increase in temperature. This phenomenon is typically attributed to the exponential enhancement of nonradiative electron–hole recombination. This model applies well to monolayer MoS₂ and MoSe₂ ($E_g = 1.55$ eV) but fails to the bilayer and few-layer MoSe₂ that have indirect bandgaps but with almost degenerate direct and indirect bandgap values.^{146b} It was observed that the intensity of PL of mechanically exfoliated bilayer and few-layer MoSe₂ was enhanced with temperature from –195 to 178 °C.^{146b} And the enhancement is due to thermally decoupling adjacent layers *via* interlayer thermal expansion of the layers, in which bandgap crossover easily goes from indirect to direct gaps. This leads to bandgap degeneracy in bilayer and few-layer MoSe₂. On the contrary, bandgap degeneracy cannot be thermally driven in bilayer MoS₂ since the indirect and direct gaps are well separated. The unusual PL behavior in bilayer and few-layer MoSe₂, strikingly different from monolayer MoSe₂ and MoS₂ as well as bilayer and few-layer MoS₂, highlights the uniqueness of semiconducting TMDs.

Kuc et al.¹⁴⁷ performed an extended study of the influence of quantum confinement on the electronic structures of monolayer and few-layer MS₂ (M = W, Nb, Re) using first-principles calculations. They found that WS₂, which is similar to MoS₂, exhibits an indirect (bulk, $E_g = 1.3$ eV) to direct (monolayer, $E_g = 2.1$ eV) band gap transition (Figure 6). In contrast, independent of the number of layers, NbS₂ and ReS₂ remain metallic. Quantum confinement-induced indirect to direct band gap crossover is also exhibited in MoSe₂ and MoTe₂ monolayer sheets (Table 1) with a direct band gap of 1.44 and 1.07 eV, respectively.¹⁴⁸ These values were calculated by using spin-polarized DFT calculations. It is worth noting that the direct band gap of the monolayer WS₂, estimated by

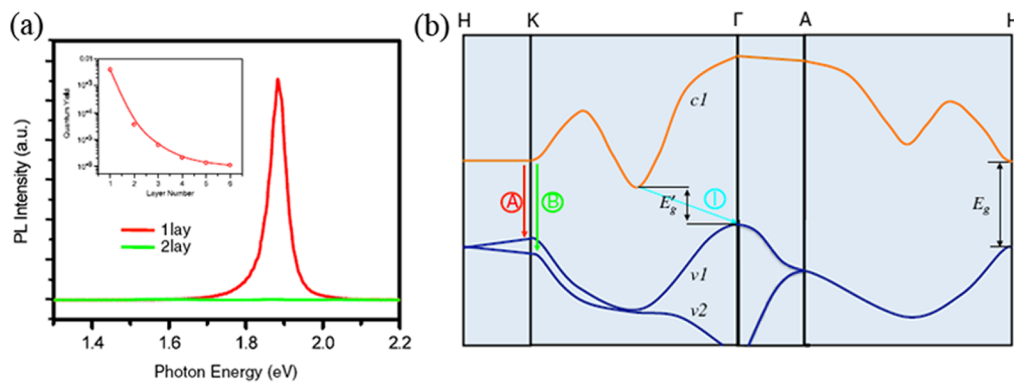


Figure 5. (a) PL spectra for mechanically exfoliated monolayer and bilayer MoS₂ samples in the photon energy range from 1.3 to 2.2 eV. Inset: PL quantum yield of MoS₂ samples with 1–6 monolayer MoS₂. (b) Simplified band structure of bulk MoS₂, showing the lowest conduction band *c*1 and the highest split valence bands *v*1 and *v*2. *A* and *B* are the direct-gap transitions, and *I* is the indirect-gap transition. *E'*_g is the indirect gap for the bulk, and *E*_g is the direct gap for the monolayer. Reproduced with permission from ref 35. Copyright 2010 American Physical Society.

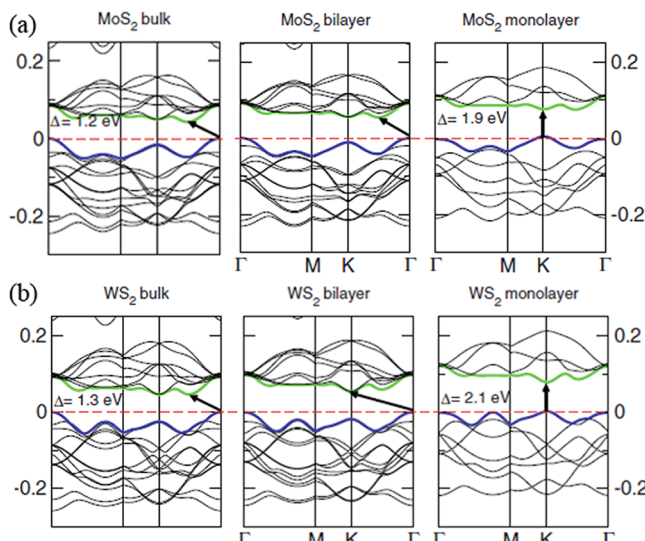


Figure 6. Band structures of (a) bulk MoS₂, its monolayer, and bilayer; (b) bulk WS₂, its monolayer, and bilayer, calculated at the DFT/PBE level. The horizontal dashed lines indicate the Fermi level. The arrows indicate the fundamental band gap (direct or indirect) for a given system. The top of valence band (blue/dark gray) and bottom of conduction band (green/light gray) are highlighted. Reproduced with permission from ref 147. Copyright 2011 American Physical Society.

Ma et al.¹⁴⁸ was 1.80 eV, which is smaller than the value calculated by Kuc et al.¹⁴⁷

In the case of bilayer MoS₂, WS₂, MoSe₂, and MoTe₂, DFT calculations showed that their fundamental indirect band gaps (1.0 to 1.5 eV)^{149,150} can be continuously driven to zero by applying external electric fields (2 to 3 V/nm) perpendicular to the layers. The result is that the range of gap tunability is much larger than in bilayer graphene (approximately 250 meV). As a general trend for MoX₂, the critical electric field for the semiconductor to metal transition decreases in the order S to Se to Te (Figure 7). This observation was attributed to the increasingly diffuse nature of the valence p_z orbitals in transitioning from S to Te, which facilitates greater charge transfer from the chalcogen to Mo under the same electric field conditions. However, the effect of switching the transition metal from Mo to W, while retaining the chalcogen (S), appears not to be significant.¹⁵¹

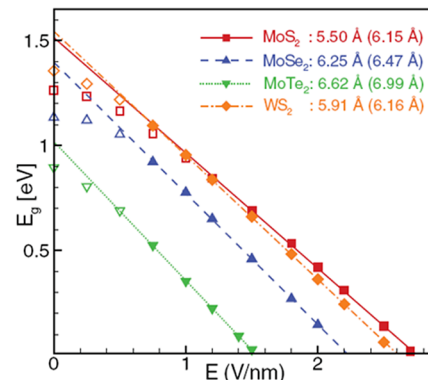


Figure 7. Band gap *E*_g versus applied electric field *E* for MoS₂, MoSe₂, MoTe₂, and WS₂. The lines are fits to the linear portion of the curve indicated by solid symbols. Hollow symbols are within the region of nonlinear response and are excluded from the fits. The GSE coefficients (magnitudes of the slopes of the linear fits) are indicated; interlayer spacings are in parentheses. Reproduced with permission from ref 151. Copyright 2011 American Physical Society.

3.2. Strain Effect on the Electronic Properties of TMDs

The controlled introduction of strain into semiconductors offers an important degree of flexibility in studies involving basic materials as well as device engineering. Strain in a crystalline solid modifies the lattice constants and reduces the crystal symmetry, leading to significant shifts in the energy band edges. This is often accompanied by a splitting of the degenerate states, and to changes in the relevant effective masses.¹⁵² The use of strain to modify the electronic, optical, and structural properties of graphene and MoS₂ is an emerging field.^{153–155} This is particularly relevant due to the zero band gap of pristine graphene.¹⁵⁶ Yun et al. studied strain effects on the electronic structures of monolayer 2H-MX₂ sheets (M = Mo, W; X = S, Se, Te).¹⁵⁷ By using first-principles calculations, they found that even a slightly different lattice value from the bulk optimum value could induce the direct-to-indirect band gap transition to changing the gap energy and the positions of the valence band maximum (VBM) as well as the conduction band minimum (CBM) of the single-layer sheets. For instance, the direct band gap of monolayer MoS₂ was maintained only within the quite narrow range of −1.3% to 0.3% which had deviated from the lattice parameter optimum value of *a* (= 3.16 Å). Any further increase in the value, more than approximately

9.8%, led the sheet to be metallic. As shown in Figure 8, the reduced lattice constant of 3.10 Å (-1.9% , compressive stress)

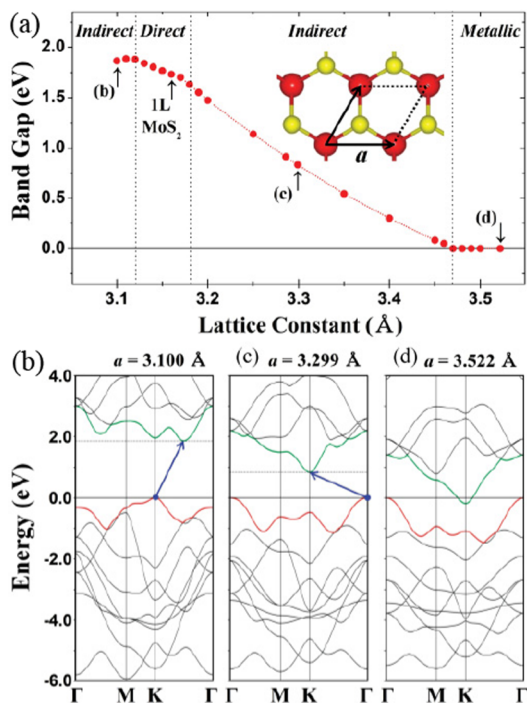


Figure 8. (a) Strain dependence of band gap energies of monolayer (1L) MoS₂ (constant lattice $a = 3.160 \text{ \AA}$). (b) The representative band structures for the compressive (left) and tensile (middle and right) stresses are displayed, respectively. Inset indicates the hexagonal structure consisting of Mo (red balls) and S (yellow balls) from the top views. Reproduced with permission from ref 157. Copyright 2012 American Physical Society.

increased E_g from 1.73 to 1.86 eV by changing the position of the CBM to the midpoint from the K point. Accordingly, the effective hole mass at the Γ and K points and the electron effective mass at the K point increased by approximately 128%, 10%, and 21%, respectively, compared to those of the unstrained monolayer MoS₂. An increased lattice of 3.299 Å (4%, tensile stress) reduced the E_g of the monolayer MoS₂ to 0.83 eV, and any further increase in the tensile stress could lead it to become metallic. The position of the VBM changed from the K point to the Γ point, while the CBM was retained at the K point. As a result, the hole and electron effective masses were reduced. These results clearly suggest that the electronic properties are sensitive to the strain and have implications for how the direct band gap can be maintained if PL feature is desirable.

3.3. Functionalization of TMDs

The influence of impurities or defects on the electronic and magnetic properties^{158,159} of both semiconducting and non-magnetic 3D and 2D MoS₂ has been investigated by first-principles calculations. For example, Fuhr et al. found that Fe and V induce magnetic moments when substituted for the S atoms on the surface of 3D MoS₂. On the other hand, neither substitutional doping of Pd or Au or S vacancy defects on the MoS₂ surface induces a magnetic moment.¹⁶⁰

Taking into consideration the fact that magnetism based on the sp orbitals of nonmetallic elements yields stronger long-range exchange coupling interactions than interactions based

on the d and f orbitals of the transition metal atoms, He et al. investigated the electronic and magnetic properties of H-, B-, C-, N-, O-, and F-absorbed MoS₂ monolayers.¹⁶¹ The theoretical predictions showed that all the atoms studied could chemically absorb onto the monolayer MoS₂ surface at room temperature. The H and N atoms that absorbed onto the top of the S atoms lead to n- and p-type semiconducting behaviors, respectively, in the monolayer MoS₂ sheets. Large spatial extensions of spin density and long-range antiferromagnetic coupling were observed in H- and F-absorbed MoS₂ monolayers. H-absorbed WS₂, MoSe₂, and MoTe₂ monolayers and F-adsorbed WS₂ and MoSe₂ monolayers also showed long-range antiferromagnetic coupling.¹⁴⁸

Ataca et al.¹⁶² studied the functionalization of single-layer MoS₂ structures through adatom adsorption (i.e., C, Co, Cr, Fe, Ge, Mn, Mo, Ni, O, Pt, S, Sc, Si, Ti, V, and W) as well as vacancy defect creation (S and Mo single vacancies, S₂ and MoS double vacancies, and MoS₂ triple vacancies) by first-principles plane-wave calculations. It was possible to attain local magnetic moments through the adsorption of specific 3d transition-metal atoms as well as Si and Ge atoms. Each MoS₂ triple vacancy created in single-layer MoS₂ induced a net magnetic moment, whereas other vacancy defects did not result in a magnetic moment. Significant charge transfer was observed upon the adsorption of C and O onto single-layer MoS₂. Among the possible native vacancies, i.e., either an M or X vacancy, in semiconducting MoSe₂, MoTe₂, and WS₂ monolayers, only the Mo vacancy in MoSe₂ induced spin-polarization and long-range antiferromagnetic coupling.¹⁴⁸ Local magnetic moments in S-terminated monolayer MoS₂ nanoribbons were significantly influenced by the coverage of S atoms at the edge.¹⁶³

It was found that the magnetic moments and strength of magnetic coupling of monolayer VX₂ (X = S, Se) sheets increased rapidly with isotropic strain. It was proposed that the strain-dependent magnetic moment was related to the strong ionic-covalent bonds. However, both the ferromagnetism and the variation in magnetic coupling strength with the strain were believed to arise from the combined effects of through-bond and through-space interactions.¹⁶⁴ The existence of magnetic behavior in pristine monolayer MX₂ sheets is quite different from graphene.^{165,166} These studies suggest the possibility of using 2D MoS₂ as well as other semiconducting TMDs in nanoelectronics and spintronics applications.

3.4. Monolayer and Few-Layer TMD FETs

In contrast to pristine graphene, which does not have a band gap, monolayer MoS₂, which has a direct band gap of approximately 1.90 eV, has attracted interest for use in building FETs and integrated circuits for logic applications.^{34,167} Electrical characterizations of single-layer MoS₂ have shown n-type conductivity with a room temperature mobility in the range of 0.5–3 cm²/(V s).^{168,169} Compared to the mobility (200–500 cm²/(V s))¹⁷⁰ of bulk MoS₂, the mobility of the single-layer MoS₂ sheets is rather low.

By using the high-k gate dielectric, hafnium oxide (HfO₂), in a top-gated device, a room-temperature mobility of larger than 200 cm²/(V s) and current on/off ratio of approximately 1×10^8 for monolayer MoS₂ FETs (Figure 9) were demonstrated.³⁶ The recovered mobility of monolayer MoS₂ was attributed to screening impurities by the high-k dielectric and/or modifications of MoS₂ phonons in the top-gated sample. Kaasbjerg et al. calculated the deformation potentials and Frohlich

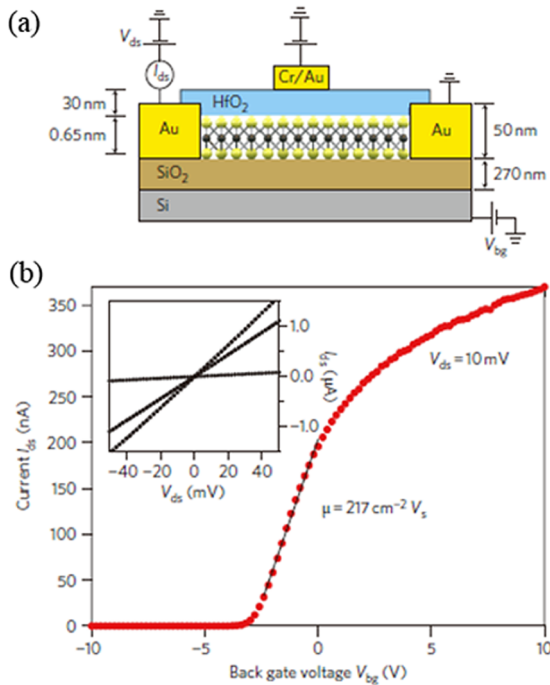


Figure 9. (a) Cross-sectional view of the structure of a monolayer MoS₂ FET. A single layer of MoS₂ (thickness, 6.5 Å) was mechanically exfoliated on a degenerately doped silicon substrate with 270 nm thick SiO₂. The substrate acts back gate. The monolayer is separated from the top gate by 30 nm of HfO₂ grown by atomic-layer-deposition technique. (b) Room-temperature transfer characteristic for the FET with 10 mV applied source-drain bias voltage V_{ds} . Back-gate voltage V_{bg} was applied to the substrate and the top gate was disconnected. Inset: current–voltage (I_{ds} – V_{ds}) curve acquired for V_{bg} values of 0, 1, and 5 V. Reproduced with permission from ref 36. Copyright 2011 Nature Publishing Group.

interaction in single-layer MoS₂, as well as the mobility from first-principles.¹⁷¹ The room temperature mobility of approximately $410 \text{ cm}^2/(\text{V s})$ was found to be dominated by the optical phonon scattering (Coulomb scattering) and was weakly dependent on the carrier density. In contrast, Yun et al.¹⁵⁷ suggested that the reason for the reduction in mobility^{168,169} in the single- or few-layer MoS₂ sheets was mainly due to the decrease in carrier concentration and the increase in the effective mass of the carriers on lowering the number of layers. A complete understanding of the microscopic picture of the transport in monolayer or few-layer MoS₂ devices remains unclear. On the basis of low-temperature electrical transport experiments of MoS₂ transistors fabricated on SiO₂/Si, Ghatak et al.¹⁶⁹ suggested that the electron transport in single- or few-layer MoS₂ occurred in a wide band of localized states originating from trapped charges in the substrate. In other words, variable range hopping transport, rather than direct excitation to CBM or mobility edge from the Fermi energy. As a result, Ghatak et al. suggested that the Coulomb potential from trapped charges in the substrate is the dominant source of disorder in single- or few-layer MoS₂ FETs, which also leads to carrier localization.

The mobility of single-layer MoS₂ devices is comparable to that of graphene nanoribbons but much lower than that of either pristine graphene or Si transistors.¹⁶ In addition, the band gap of monolayer MoS₂ is too large. The key features of MoS₂ transistors include (i) a large on/off current ratio ($>10^{10}$), (ii) a high degree of immunity to short channel effects

(drain-induced barrier lowering of approximately 10 mV/V), (iii) abrupt electrical switching with a subthreshold swing that can be as low as 60 mV/decade,¹⁷² and (iv) photoswitching.¹⁷³ Because of their lower mobility, MoS₂ transistors have been proposed as being better for low-power applications compared to Si transistors,¹⁷⁴ rather than for high-performance applications.¹⁷²

Similar to the dielectric/semiconductor interface, the electrical contact at the interface between the semiconductor and source/drain electrodes plays an important role in FETs performance. The use of large band gap semiconductors with ultrathin bodies is essential for minimizing the short channel effects at extreme scaling limits. It has been reported that the characteristic length of a 5 nm thick MoS₂ transistor built on a 300 nm thick SiO₂ gate oxide was 34.6 nm. This characteristic length would be 2 nm if the SiO₂ gate dielectric layer were replaced by using a 6 nm thick HfO₂, which is far beyond the technique consideration of a 10 nm node with alternative channel materials for logic applications.¹⁷⁵ This result suggests a superior immunity to short channel effects for MoS₂ transistors. However, there is some difficulty in forming ohmic metal contacts with large band gap semiconductors, and thus the Schottky barrier formed at the channel material/metal interface limits the field-effect characteristics of short channel ultrathin FETs. On the other hand, the presence of a Schottky barrier can make a device exhibit ambipolar behavior, accumulation of electrons (*n*-FETs) for positive gate voltage and of holes (*p*-FETs) for negative gate voltage. Such ambipolar behavior was observed by the FETs using chemically synthesized WS₂ with a thickness of 13 nm. Here the WS₂ layer was deposited onto 30 nm thick Al₂O₃/*p*-Si and the source and drain electrodes were Ti/Au (5/100 nm).¹⁷⁶ As mentioned above, MoS₂ exhibits high-performance *n*-type behavior. However, for complementary digital logical applications, *p*-type FETs are required. Bulk WSe₂ FETs revealed an intrinsic hole mobility of up to $500 \text{ cm}^2/(\text{V s})$. However, the bulk devices exhibited poor on/off current ratios (less than 10) at room temperature, along with ambipolar behaviors.¹⁷⁷ In order to lower the Schottky barriers with monolayer WSe₂, high work-function Pd and contact doping with NO₂ strategies were used to achieve hole transport (*p*-FET) in mechanically exfoliated monolayer WSe₂ FETs with a channel length of approximately 9.4 μm .¹⁷⁸ Used together with 17.5 nm ZrO₂ (dielectric constant of approximately 12.5), the FETs exhibited a hole mobility of approximately $250 \text{ cm}^2/(\text{V s})$ and on/off current ratio of larger than 10^6 .

In order to realize complementary logic circuits based on 2D semiconductors, lateral patterns of *n*-type and *p*-type semiconductors may be required. These would be realized by using patterned syntheses of both *n*-type and *p*-type semiconductors on the same substrate or by selective doping. Recently, lateral heterostructures based on graphene and *h*-BN have been reported.¹⁷⁹ Stacked structures consisting of alternate *n*-type and *p*-type semiconductors can also act as possible circuit layouts. The major challenges include identifying the correct substrates that can be used for synthesizing both *n*-type and *p*-type high-quality semiconductors, such as MoS₂ and WSe₂, on the same substrate under similar synthesis conditions, fabrication of stacked devices, and finally the isolation and connection of the individual devices. Electron irradiation-induced defects during the patterning need to be taken into consideration.^{46,180} Also transferring 2D semiconductors from the synthesis substrate to a target substrate may be necessary. Currently,

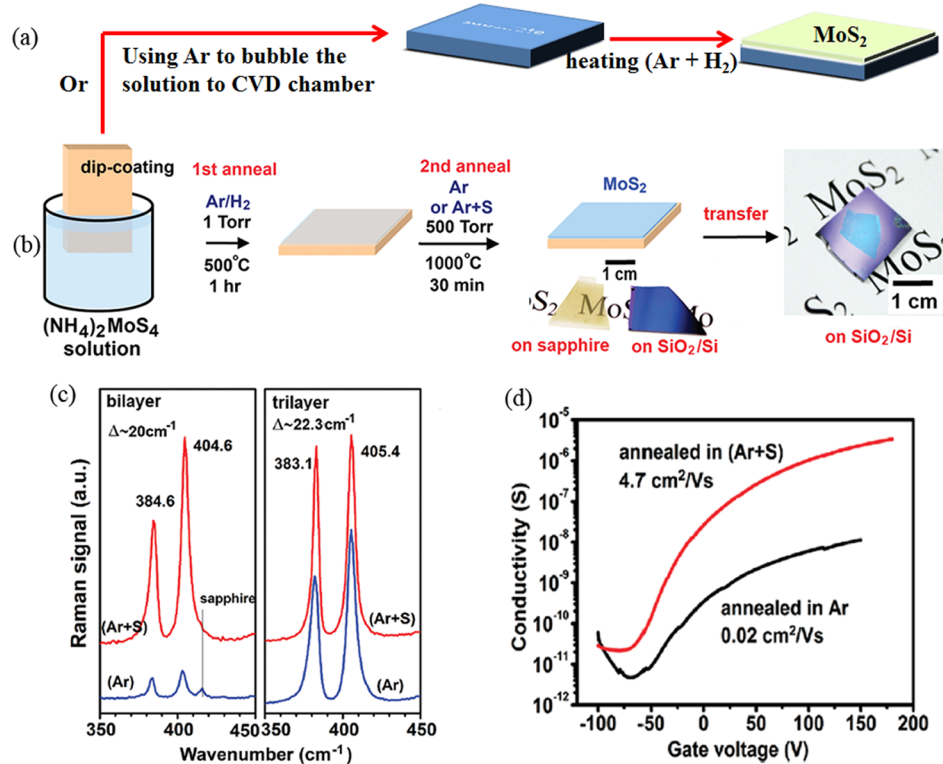


Figure 10. (a) Schematic illustration of CVD synthesis of MoS₂ thin films from solution precursor ((NH₄)₂MoS₄). (b) Two-step thermolysis process for the synthesis of MoS₂ thin layers on insulating substrates. The precursor (NH₄)₂MoS₄ was dip-coated on a substrate followed by the two-step annealing process. The as-grown MoS₂ film can be transferred onto other arbitrary substrates. (c) Raman spectra for the bilayer and trilayer MoS₂ sheets grown on sapphire substrates (excitation laser: 473 nm), where the labels (Ar) and (Ar + S) represent the MoS₂ sheets separately prepared in pure Ar and in the mixture of Ar and sulfur during the second annealing. Reproduced with permission from ref 194. Copyright 2012 American Chemical Society.

the damage-free transfer of graphene from the metal substrate used for the synthesis to an arbitrary substrate remains a great challenge with respect to achieving the electronic applications of graphene.¹⁸¹

The application of mechanically exfoliated monolayer, bilayer, trilayer, and quadrilayer MoS₂ FETs for NO gas sensing has also been exploited.¹⁸² Results showed that single-layer MoS₂ exhibited a rapid and dramatic response upon exposure to NO, but the signal was found to be unstable. In contrast, the MoS₂ FETs comprised of other numbers of layers exhibited both stability and sensitivity to the gas. Detection limits of 0.8 ppm were found.¹⁸² Because of the energy gap modulation by the number of MX₂ layers, it is possible to exploit such characteristics for selective light detection. It was shown that phototransistors consisting of trilayer MoS₂ exhibited excellent photodetection capabilities for red light, while those with monolayer and bilayer turned out to be useful for green light detection.¹⁸³

3.5. Synthesis of TMD Sheets

Mechanical exfoliation remains the best method for separating layered TMD crystals with a view to investigating their inherent physical properties. The typical characteristics of FETs and PL of MoS₂ layers that have been demonstrated to date are mainly derived from mechanically exfoliated MoS₂ sheets.^{35,36,144,169} Solution-based exfoliation can be used to easily produce bulk mixtures of single-layer and multilayered TMD materials. Such a process can involve organic solvents,^{77,79} lithium ion intercalation,^{78,146,184} or surfactants.⁷⁸ Coleman et al.⁷⁷ reported that a surfactant-free liquid-exfoliation method can

produce few-layer TMD materials including MoS₂ and WS₂. More than 20 solvents have been investigated to study the dispersibility of TMDs in this range of solvents, chosen because of their surface tension and precedence for dispersing carbon nanotubes and graphene. Furthermore, Zhou et al.⁷⁹ discovered that using low-boiling-point solvent mixtures containing water and ethanol, suspensions comprising few-layer MoS₂, WS₂, or BN sheets can be efficiently formed. The solvents can easily be removed because of their low boiling points. When exfoliation was carried out in aqueous surfactant solutions, the result led to large-scale few-layer TMD sheets.⁷⁸ One of the disadvantages of liquid exfoliation, in both organic solvents and aqueous surfactant solutions, is the difficulty in preparing monolayer TMD sheets. As discussed above, the monolayer semiconducting TMD sheets have unique electronic and optical properties that are different from bilayer, few-layer, and bulk TMDs. Thus, a method that can prepare single-layer sheets is highly desirable. Ion intercalation is an effective method for preparing single-layer sheets. For example, Zeng et al.¹⁸⁴ reported the high-yield production of single-layer TMDs, which included MoS₂, WS₂, TiS₂, and ZrS₂, through a relatively complex lithiation process. That is compared to the simple lithium intercalation process reported by Eda et al.¹⁴⁶ However, ion intercalation is time-consuming and environmentally sensitive. The greatest disadvantage of the intercalation procedure is the structural deformation of the original TMD materials induced by the ion intercalation.⁷⁸ For instance, exfoliation of MoS₂ does not give monolayer MoS₂ but monolayer Li_xMoS₂. The structural changes that occur during

ion intercalation can dramatically affect the electronic and optical properties of the pristine monolayer TMD sheets.¹⁴⁶

Other than exfoliation methods for the preparation of the 2D layered TMDs, there are a growing number of reports regarding the synthesis of monolayer or few-layer TMD sheets by other methods. Previously, techniques such as sputtering,^{185,186} chemical reactions,¹⁸⁷ pulse laser deposition,¹⁸⁸ CVD,¹⁸⁹ and thermal evaporation¹⁹⁰ have all been used to prepare 3D MoS₂, WS₂, and other TMD thin films. These methods could be explored to prepare single- and few-layer TMDs sheets. Using the electron beam deposition of molybdenum on a thiophenol-precoated Cu(111) surface, Kim et al.¹⁹¹ reported the formation of MoS₂ monolayer islands with lateral sizes of tens of nanometers.

Zhan et al. demonstrated the vapor-phase growth of single- and few-layer MoS₂ sheets by direct elemental chemical reaction.¹⁹² In a typical procedure, a thin layer (1–5 nm) of Mo was predeposited on SiO₂ using an electron-beam evaporator. The reaction took place in a quartz tube, where pure sulfur (1–2 g) was placed in the upwind low-temperature zone, a little above the melting point of sulfur (113 °C). Prior to reaction, the tube was purged by N₂. The temperature at the Mo film zone was first increased to 500 °C over 30 min, and then heated to 750 °C over 90 min and was then kept at 750 °C for 10 min before being cooled down to room temperature over 120 min. The resistivity of the resulting synthesized ultrathin MoS₂ films (single- or few-layer) on SiO₂ was approximately $2.0 \times 10^4 \Omega/\square$ and was about 2 orders of magnitude higher than that of CVD-grown graphene (approximately $125 \Omega/\square$). In addition, the typical room-temperature mobility of the single- or few-layer MoS₂ sheets was in the range from 0.004 to 0.04 cm²/(V s); much lower than mechanically exfoliated MoS₂ flakes. The cause of the poor electrical properties of the synthesized MoS₂ was not addressed by the authors. However, one possibility is that this may be due to the poor structural homogeneity and impurities in the MoS₂ films. This is supported by Raman spectroscopic evidence in the relatively large peak width but small peak intensity of the E¹_{2g} Raman mode of the synthesized MoS₂ sheets.

Lee et al.¹⁹³ reported the synthesis of monolayer or few-layer MoS₂ sheets on chemically reduced graphene oxide, perylene-3,4,9,10-tetracarboxylic acid tetrapotassium salt, or perylene-3,4,9,10-tetracarboxylic dianhydride modified SiO₂ substrate by using the reactants MoO₃ and sulfur at 650 °C in a N₂ flow. It was found that the surface treatment promoted growth of the MoS₂ sheets. The mobility of the synthesized MoS₂ sheets in bottom-gated transistors on a SiO₂/Si platform was approximately 0.02 cm²/(V s). This is similar to the value reported by Zhan et al.¹⁹²

Using the thermolysis of ammonium thiomolybdates (NH₄)₂MoS₄ in Ar/H₂ atmosphere and further annealing in sulfur vapor, Liu et al. synthesized large-area, high-quality, mostly trilayer, MoS₂ thin layers.¹⁹⁴ In contrast to conventional CVD methods (Figure 10a), a substrate such as sapphire or SiO₂/Si was immersed in the (NH₄)₂MoS₄ solution using DFM as the solvent to form a thin (NH₄)₂MoS₄ film on the substrate. This was followed by baking on a hot plate at 120 °C for 30 min (Figure 10b). The (NH₄)₂MoS₄ film on the substrate was first annealed in a quartz tube furnace flowing with Ar/H₂ (flow rate = 4/1, at 1 Torr) gas at 500 °C and then annealed at 1000 °C in Ar gas mixed with sulfur vapor at 500 Torr. The annealing at 1000 °C in Ar was found to improve the MoS₂ crystal structure, and the addition of sulfur to the annealing

process further improved the crystallinity and electrical performance of the MoS₂ ultrathin layers. The main reason for the improved crystallinity of the trilayer MoS₂ films made with sulfur vapor was attributed to the removal of oxygen species according to transmission electron microscopy-based energy dispersive spectroscopic analysis (TEM-EDS). The Raman (Figure 10c) and PL spectra of trilayer MoS₂ films all suggested that the quality of MoS₂ layers grown on sapphire is superior over that grown on SiO₂/Si. The annealing with sulfur significantly improved the electrical properties of the MoS₂ devices with SiO₂ as the dielectric layer. The electron mobility and on/off current ratio of trilayer MoS₂ devices, synthesized on sapphire with sulfur and Ar as the annealing atmosphere, was increased to approximately 4.7 cm²/(V s) and 1.6×10^5 from 10^{-2} cm²/(V s) and 2.4×10^3 of that synthesized without sulfur during annealing (Figure 10d). These parameters are comparable to the mechanical exfoliated MoS₂ sheets, and the method can be scaled up for large-area batch preparation.

Besenbacher's group elucidated the structure and morphology of single-layer and multilayer MoS₂ nanoclusters using ultrahigh vacuum scanning tunneling microscopy (STM).^{195,196} The crystalline MoS₂ nanoclusters were prepared by depositing Mo on Au(111) or a highly oriented pyrolytic graphite (HOPG) substrate in an H₂S atmosphere of approximately 7.5×10^{-7} Torr at 127 °C. Subsequently, the sample was annealed at 400 °C for the Au(111) substrate and 727 or 927 °C for the HOPG substrate while maintaining the H₂S background pressure to facilitate full sulfidation and crystallization. After being cooled to 127 °C in an H₂S atmosphere, the sample was analyzed using STM at room temperature. It was found that the pristine HOPG(0001) surface did not support a high dispersion of MoS₂ due to weak interaction between MoS₂ and the surface. But with a small density of defects in the surface introduced by the ion bombardment, highly dispersed MoS₂ nanoclusters could be successfully synthesized on the graphite. The 2H-MoS₂ nanoclusters preferentially adopted a hexagonal morphology on both the Au(111) and graphite substrates but with various shapes and stacking of these nanoclusters which depended on the substrate and the subsequent annealing temperature. In the case of the MoS₂ nanoclusters synthesized on the Au(111) surface,^{195,197} single-layer triangular shape MoS₂ nanoclusters were formed with the basal (0001) plane oriented parallel to the Au(111) surface. Combined with DFT calculations, it was observed that the Mo-edge covered with S atoms terminated the triangular MoS₂ nanoclusters; the S atoms at the edge were out of registry with the S atoms in the hexagonal lattice of the basal plane, which was shifted by half a lattice constant along the edge. The edge termination of the single-layer triangular MoS₂ nanoclusters is different from that found for bulk MoS₂ nanoclusters which should be determined by two types of edge terminations, S-edge and Mo-edge. The termination of triangular MoS₂ is believed to have significant implications for catalytic reactions since MoS₂ nanoclusters constitute the basis of hydrotreating catalysts used to clean up sulfur-containing molecules from oil products in the hydrodesulfurization process.^{198,199}

In the case of the graphite substrate,¹⁹⁶ single-layer MoS₂ nanoclusters were synthesized at 727 °C, and multilayer (2–5 layers) nanoclusters were synthesized at 927 °C. The latter had lower cluster coverage than that of the former due to the stacking produced by keeping the same total amount of Mo. It was also found that a lower annealing temperature, even with the same H₂S pressure, led to a relatively poor crystalline order

of the MoS₂ nanoclusters. In contrast to the triangular shape of the MoS₂ nanoclusters on Au(111) terminated with Mo-edge, the MoS₂ nanoclusters synthesized on HOPG display a hexagonally truncated shape terminated with both Mo-edge and S-edge. This was attributed to a lower chemical potential of sulfur at elevated temperature and a stabilizing effect of hydrogen on the S-edge. The Moiré pattern²⁰⁰ arising from rotation and lattice mismatch between single-layer MoS₂ nanoclusters and HOPG was observed with a varied rotation angle of the MoS₂ relative to the HOPG from cluster to cluster. This indicates that the interaction between the MoS₂ basal plane and the HOPG lattice is rather weak (due to van der Waals interactions). This also suggests that the defects introduced by ion bombardment play an important role in the bonding of the MoS₂ nanoclusters, predominantly through the edge sites of the nanoclusters, to graphite at elevated temperatures. The preferential 3D growth of stacked MoS₂ nanoclusters at 927 °C reflects the fact that the adhesion of the topmost layers of the MoS₂ nanoclusters on the lower layers was larger than that on the HOPG(0001) or on defects on the substrates. The stacking of the multilayer MoS₂ nanoclusters was most likely facilitated by interlayer bonding at sites near the cluster perimeter due to the presence of electronic edge states localized at the two outermost atomic rows instead of the common interlayer van der Waals bonding. Two types of low-index MoS₂ edges were identified for multilayer MoS₂, i.e., the Mo-edge fully saturated with sulfur and the fully sulfide S-edge (with approximately 50% coverage of hydrogen). Such edge termination is believed to be catalytically important. These results together with the above three recent synthesis strategies^{192–194} should shed new light on how to achieve large-area high-quality single- or few-layer MoS₂ sheets by controlling experimental factors such as temperature, growth time, precursors, annealing atmosphere, and substrate surface.

There has also been some effort to synthesize other TMDs. 2D WS₂ nanosheets down to 2–3 layers were synthesized through the chemical reaction of tungsten oxide (W₁₈O₄₉) nanorods with carbon disulfide (CS₂) in a hot hexadecylamine solution.²⁰¹ In a typical procedure, tungsten oxide nanorods (40 mg) and hexadecylamine (1.45 g, 6 mmol) were added to a 50-mL three-neck round-bottom flask under Ar. The reaction mixture was first heated to 100 °C to remove water and was subsequently heated to 250 °C. After injecting CS₂ (0.12 mL, 2 mmol), the resulting solution was further heated to 330 °C. During the reaction, the initially blue solution gradually became dark brown, indicating when the reaction was finished. In another approach, the decomposition of (NH₄)₂MoS₄ or (NH₄)₂WS₄ single-source precursors containing metal and sulfur in oleylamine under a N₂ atmosphere at 360 °C, MoS₂ or WS₂ nanosheets coated with oleylamine were reported.²⁰²

3.6. Analysis of the Existence of Monolayer TMD Sheets

Although single- and few-layer examples of MoS₂, WS₂, TiS₂, and ZrS₂ have been synthesized, it was found that not all of the possible 88 different combinations of MX₂ compounds can be stable in free-standing, single-layer honeycomb-like structures as predicted by using first-principles structure optimization and phonon calculations based on DFT.²⁰³ The results, according to Ataca et al., of stability analysis and electronic properties of 44 stable monolayer MX₂ sheets are summarized in Figure 3.²⁰³ The stable single-layer MX₂ sheets can be semiconductor, ferromagnetic, or nonmagnetic metals. Semiconducting single-layer 2H-MX₂ sheets display rather different band structures.

Transition metal oxides (i.e., M = Sc, Cr, Mo, W; X = O) differ from the other group (i.e., M = Cr, Mo, W; X = S, Se, Te) by their relatively smaller band gaps and lower band-edge state densities. All MO₂ honeycomb structures are indirect band gap semiconductors, while the other group usually consists of direct semiconductors. For all single-layer MX₂ semiconductors, the band gap generally increases as M goes from Sc to W. In the case of MX₂ (X = O, S, Se, Te), similar band structures as M goes from V to W were also found; essentially they are either metal or semiconductor depending on the number of s and d valence states of the free M atoms. Some other examples are worthy of mention: 2H-VX₂ or FeX₂ (X = O, S, Se, Te) are ferromagnetic metals with magnetic moments locating at the d orbital of the transition metal atoms, whereas in the case of ScX₂ (X = O, S, Se) the magnetic moment is located at the site of the chalcogen atoms because in this case a crucial amount of charge, originating from a relatively lower electronegativity of Sc with respect to the chalcogen atoms, is transferred from Sc to X. The mechanical properties of the single-layer MX₂ sheets were evaluated by using in-plane stiffness instead of Young's modulus. The calculated in-plane stiffness values of the single-layer MX₂ are in the range 250 to 9 N/m. This is smaller than the corresponding value for graphene (357 N/m, experimental value 340 ± 50 N/m) and BN (267 N/m) sheets.

In contrast with the intensive research efforts being expended in the study of graphene, the electronic and other relevant properties of layered TMD materials, in particular, materials other than MoS₂, remain largely unexplored. A suitable method for the large-scale synthesis of continuous high-quality single- or few-layer MoS₂ or related semiconductors is yet to be developed. Of necessity it will be required to be suitable for the fabrication of optoelectronic devices that exploit properties originating from nonzero band gap semiconductors. It should be noted that the conventionally used quartz-tube-based furnaces are not suitable for continuous and massive production of high-quality, large-scale homogeneous graphene sheets. This is due to the nonuniform distribution of gaseous carbon precursors, the thermal field between the rolled copper foils^{89a} as well as the trapping of reaction byproducts in the copper foils. Roll-to-roll process was reported to grow graphene on flexible Cu foils by atmospheric CVD.^{89b} However, the mechanical endurance of Cu foils at approximately 1000 °C must be considered during the roll-to-roll processing. A lower synthetic temperature (approximately 400 °C) by microwave plasma CVD produced poor quality graphene films with sheet resistance of 1×10^4 to $7 \times 10^5 \Omega/\square$,^{89c} 2–3 orders higher than normal ones.^{89a} Furthermore, the treatment of substrates and the preparation of metal catalysts onto the substrates cannot be accomplished by these systems. We have production systems^{89d} for continuous and scalable growth of 2D materials including graphene.^{89e} Instead of the winder/unwinder of a roll-to-roll system,^{89b,c} our systems utilize wheel arrays to controllably convey substrates along the production line, from the feeding of substrates, the treating of substrates, the depositing of catalysts on the substrates, and to the forming of 2D films.

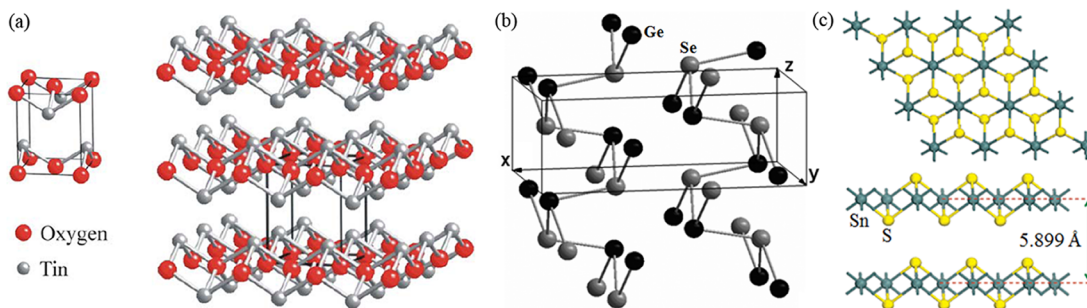


Figure 11. (a) Ball-and-stick model for litharge structure of SnO. Reproduced with permission from ref 214. Copyright 2005 Elsevier. (b) The Pnma62 orthorhombic structure of GeSe. Reproduced with permission from ref 216. Copyright 2007 IOP Publishing. (c) Top view of SnS₂ where Sn and S atoms form a honeycomb network with an Sn atom located at the center of each honeycomb and side view of S–Sn–S layers separated by 5.94 Å. Reproduced with permission from ref 219. Copyright 2005 American Chemical Society.

Table 2. Lattice Parameters (*a*, *c*), Spacing Distance (*d*), and Experimental and Theoretical Bang Gaps of Typical Metal Chalcogenides

compounds	<i>a</i> (Å)	<i>c</i> (Å)	<i>d</i> (Å) spacing	crystal system/symmetry space group	<i>E_g</i> (eV) direct ^a	<i>E_g</i> (eV) indirect ^a	<i>E_g</i> (eV) direct ^b	<i>E_g</i> (eV) indirect ^b
SnO ²⁰⁸	3.80	4.84	2.52	tetragonal <i>P4/nmm</i>	3.0		2.9	0.2
SnS ^{208,232}	11.14	4.34		orthorhombic <i>Pnma</i>		1.41	2.1	1.5
SnSe ^{208,232}	11.50	4.45		orthorhombic <i>Pnma</i>	1.27	0.89	1.3	0.9
GeS ^{208,232}	10.470	4.297		orthorhombic <i>Pnma</i>	1.65	1.56	1.12	1.1–1.3
GeSe ²³²	4.40	10.82		orthorhombic <i>Pnma</i>	1.21	1.14	1.50	1.08
SnS ₂ ^{221,222}	3.648	5.899	5.899	CdI ₂ -type	2.44, 2.07	2.29, 2.88	2.66, 2.44	2.48, 2.31
SnSe ₂ ^{222,224}	3.81	6.14	6.137	CdI ₂ -type	1.62	0.97	1.63, 1.40	1.44, 1.26
GaS ^{c263,270,278}	3.587	15.49	7.60		3.0	2.53	3.04	2.59
GaSe ^{c263,264}	3.75	15.99	7.97		2.11	1.995	2.1	2.0

^aExperimental value. ^bTheoretical value. ^cDifferent types of the GaS or GaSe have differences in the stacking sequences, atomic positions and as consequence, differences in interlayer interactions and distances.

4. LAYERED GROUP-IV AND GROUP-III METAL CHALCOGENIDES

4.1. Structural and Electronic Properties of Layered Group-IV Metal Chalcogenides

Currently, there are only a few reports on single- or few-layer group IV–VI and III–VI layered compounds. Hence, the 2D characteristics of these materials are to a large extent unknown. However, these bulk metal chalcogenides exhibit various electrical and optical properties suitable for numerous applications in the fields of catalysis, nanotribology, optoelectronics,²⁰⁴ and lithium ion batteries.²⁰⁵ They could be expected to show distinct properties since they are capable of reaching thicknesses down to only single- or few-layer. Here we provide a survey of our knowledge to date of the basic structural and electronic properties of these bulk materials. The particular focus will be on tin and gallium chalcogenides in the hope of attracting greater interest in the search to discover the hidden 2D properties of such layered metal chalcogenides.

Tin monochalcogenides, SnX (X = O, S, Se, or Te), have an electron configuration of 4d¹⁰5s²5p⁰ for Sn²⁺, in which the chalcogen (ns²np⁶) is always the most electronegative element and thus “captures” two electrons from the tin atom. In cases where the oxidation state is +2, the Sn 5s electrons do not take part in the bonding, but constitute a lone-pair. This is defined as an intermediate state between an inert spherical s²-type orbital that is centered on the nucleus and a nonbonded hybridized-orbital lobe that is nonspherical but localized far from the atomic nucleus.²⁰⁶ The result is distortion of the atomic arrangement around the tin atoms. The main contribution to the VBM for SnS and SnSe is from the p

orbitals of S²⁻ or Se²⁻ (with some degree of hybridization with the cation s band),²⁰⁷ while the CBM is mainly from the empty p orbitals of Sn²⁺ (refs 208–212). The lone-pair behavior in SnO differs from that in SnX (X = S, Se, Te).²⁰⁸ In the case of SnO, the lone-pair points toward the interlayer space, creating a van der Waals gap, whereas it is less active in SnS and SnTe. Here it pushes away its Sn neighbors, thus creating a distortion relative to the cubic NaCl structure. The structure of SnX compounds evolves from a 3D SnTe structure to a 2D SnO with an intermediate dimension for SnS and SnSe. In layered SnO (see Figure 11a), the structure is layered in the [001] crystallographic direction with a Sn_{1/2}–O–Sn_{1/2} sequence and the van der Waals gap between adjacent Sn planes is 2.52 Å (Table 2); oxygen atoms are tetrahedrally bonded to Sn ones. The Sn atoms are situated at the apex of regular square-based pyramid of oxygen atoms with a Sn–O distance of 2.224 Å. The symmetry space group is *P4/nmm* and the lattice constants are *a* = *b* = 3.80 Å and *c* = 4.84 Å.^{213,214}

The sp interaction of the group IV–VI chalcogenides tends to destabilize the cubic structure and to decrease the average gap between the valence and the conduction bands.²¹⁵ As a result, SnTe and PbX (X = S, Se, or Te) crystallize with a cubic NaCl structure and GeTe and SnTe have a rhombohedral structure. In contrast, SnS, SnSe, GeS, and GeSe all adopt orthorhombic structures²¹⁶ (Figure 11b) with large band gaps. This orthorhombic *Pnma* structure is viewed as a highly disordered NaCl rock salt structure that is comprised of zigzag double planes of the metal monochalcogenide separated by a van der Waals gap of approximately 1.0 Å. The local atomic distribution around the tin atoms is a chalcogen-distorted

octahedron with Sn–X or Ge–X angles slightly deviating from 90° and with three short and three long Sn–X or Ge–X bonds. SnS, SnSe, GeS, and GeSe exhibit polymorphic phase transitions with temperature. This typical crystalline structure results in strong anisotropic optical properties at low energies and more isotropic optical properties at higher energies. All of which makes them interesting materials intermediate in character between 2D and 3D semiconductors. For example, the anisotropic photoresponse properties of GeSe nanosheets were recently observed.²¹⁷ It was found that the on/off photoswitching ratio of chemically synthesized GeSe nanosheets in the direction parallel to the crystal *a* axis was 3.5 times higher than that in the direction perpendicular to the *a* axis.

Tight binding (TB) calculations predict that bulk SnS, SnSe, GeS, GeSe, and SnO have band gaps for both direct and indirect transitions. On the other hand, SnTe is a direct gap semiconductor with a gap of approximately 1.1 eV.²⁰⁸ SnO has an indirect gap Γ -M of 0.2 eV, and a direct gap with transition at the M points of 2.64 eV; experimental results span range from 2.5 to 3.0 eV (see Table 2).

The oxidation state of Sn can also adopt the +4 state. This is attributed to the versatile coordinating characteristics of tin and sulfur.²¹⁸ SnS₂ adopts a CdI₂-type layered structure with a hexagonal unit cell. Here the Sn atoms are located in the octahedral sites between two hexagonally close-packed S slabs to form a sandwich structure²¹⁹ (Figure 11c). The SnS₂ layer can be viewed as composed of all-edge-sharing octahedral SnS₆ building units with the sulfurs exhibiting three-coordination and local trigonal-pyramidal symmetry. The SnS₂ layers are then stacked on top of one other along the crystallographic *c*-axis and held together by weak van der Waals forces. SnS₂ also exhibits polytypism depending on how the layers are stacked. All the polytypes have the same hexagonal close-packed structure within the layer, and therefore an identical unit cell parameter *a* of 3.647 Å. However, they exhibit a different parameter *c* orthogonal to the layer which is an integral number of the interlamellar spacing 5.899 Å.^{218,220} Measurement of the optical absorption of single crystal SnS₂ (*a* = 3.639 Å, *c* = 5.884 Å) showed that SnS₂ is an indirect semiconductor^{221,222} with a band gap of approximately 2.21 eV (Table 2). It was reported that the band gap of polytypic SnS₂ decreases with increasing polytype periodicity.²²³ SnSe₂ shows a similar structure to SnS₂ but has a smaller band gap^{222,224} (Table 2). In contrast to layered SnO, SnO₂ is not a layered material. SnO₂ has a wide band gap of approximately 3.6 eV and exhibits *n*-type behavior due to its intrinsic nonstoichiometry which arises from oxygen vacancies.²²⁵

4.2. Synthesis of Layered Group-IV Metal Chalcogenides

Compared to toxic Pb, Cd, and Hg compounds,^{226–229} the environmentally friendly SnS, SnSe, GeS, and GeSe compounds have band gaps in the range of 0.5–1.6 eV. These overlap well with the solar spectrum, and the absorption coefficient near the fundamental absorption edge is approximately 10⁴ cm^{−1}. This allows light absorption at narrow thickness,²³⁰ which makes such compounds efficient absorbers of incident solar radiation. They also exhibit multiple exciton generation, which leads to improvement in solar cell efficiency.²³¹ Nanocrystals with various shapes and sizes are being intensively investigated with a view to potentially reducing production cost for optoelectronic applications, such as for solution processable thin film transistors²⁰⁴ and photovoltaic applications.²³² The field-effect mobility of metal chalcogenide film transistors are generally

higher than transistors incorporating organic or polymeric semiconducting thin films.^{233,234} However, the power conversion efficiency of solar cells incorporated with metal chalcogenide materials remains poor (less than 3.0%). Despite intensive study related to the synthesis of 0D and 1D nanocrystals and the exploitation of their applications,^{235–247} there are still only a few reports of 2D nanosheets of these metal chalcogenides. In particular, because of their high electrical conduction and the high surface area of their 2D sheets, metal sulfur nanostructures are currently attracting more and more attention for lithium ion batteries with the potential to enhance the effective interaction between the active materials and the electrolyte and shorten the diffusion length of the charge carriers.^{243–247}

Zhang et al.²⁴⁸ reported the synthesis of single crystal SnS nanosheets *via* the pyrolysis of a presynthesized precursor of Sn(Ddtc)2(Phen) (Ddtc = diethyldithiocarbamate, Phen = 1,10-phenanthroline) at 300 °C under a N₂ atmosphere. The thickness of the nanosheets was approximately 20 nm. Vaughn et al.^{249a} synthesized GeS nanosheets by mixing GeI₄, hexamethyldisilazane (HMDS), oleylamine, oleic acid, and dodecanethiol as the sulfur source at 320 °C for 24 h. In the case of the synthesis of GeSe nanosheets, trioctylphosphine selenide was used as the selenium source. The thickness of orthorhombic GeS and GeSe nanosheets oriented along the [100] direction were 3–20 nm and 5–200 nm, respectively. The indirect and direct band gaps of GeS (GeSe) nanosheets estimated from diffuse-reflectance spectroscopy by a Perkin-Elmer Lambda 950 system were approximately 1.58 eV (1.14 eV) and 1.61 eV (1.21 eV), respectively. SnSe nanosheets with average dimensions of the order 500 nm × 500 nm and with a thickness down to 10 nm were reported as orienting along the [100] direction. The colloidal SnSe nanosheets were synthesized by slowly heating a mixture of SnCl₂, oleylamine, tri-*n*-octylphosphine (TOP), selenium powder, and HMDS to 240 °C for 30 min. The proposed growth mechanism of the nanosheets is that lateral growth occurred first, followed by subsequent growth in the vertical direction. A film of the SnSe nanosheets deposited on a glass substrate showed a direct band gap of approximately 1.0 eV and an indirect band gap of approximately 0.9 eV.²⁵⁰

Because of a high theoretical capacity of 645 mAh/g for lithium ion batteries,²⁰⁵ SnS₂ nanosheets are attracting attention with attempts to overcome the large volume change and quick capacity fading during the charge–discharge processes. The reaction of SnCl₄·SH₂O with solid sulfur in the presence of ethylene glycol (C₂H₆O₂) as the reducing agent at approximately 160–200 °C led to the formation of SnS₂ nanosheets with a thickness of approximately 2.0 nm.²⁵¹ Du et al.²⁵² synthesized hexagonal SnS₂ nanoplatelets with a thickness of 7–10 nm using a solvothermal process with SnCl₄·SH₂O and CS₂ as the precursors at 180 °C for 24 h. Because of the existence of oleylamine as a capping reagent, the optical band gap of the as-synthesized SnS₂ nanoplatelets was approximately 1.91 eV, compared to 2.35 eV for bulk SnS₂. Compared to bulk SnS₂ materials, the nanoplatelets showed improved photocatalytic degradation on rhodamine B (RhB). Hexagonal SnS₂ nanosheets with a thickness of approximately 5 nm and a lateral size of approximately 60 nm were prepared by the reaction of tin(IV) chloride penta-hydrate (SnCl₄·5H₂O) with thioacetamide as the sulfur precursor at 160 °C for 12 h.²⁵³ SnS₂ nanoplates were also synthesized by the reaction of SnO₂ on graphene oxide sheets with H₂S in an Ar atmosphere at 300

$^{\circ}\text{C}$.²⁵⁴ The thickness of the synthesized SnS_2 nanoplates was approximately 6.9 nm. SnS_2 films comprising nanosheets with 2–5 SnS_2 monolayers have also been reported.²⁵⁵ The SnS_2 film was directly grown onto Sn foil by a biomolecule-assisted method first *via* the oxidation of Sn to Sn^{2+} , and then the formation of $\text{Sn}(\text{l-cysteine})^{2+}$. An elevated temperature was found to transform SnS to SnS_2 . According to the Raman spectrum, the as-synthesized film contained the SnS phase. The optical band gap of the as-synthesized film was approximately 2.55 eV. The film exhibited improved performance for lithium ion batteries compared to bulk SnS_2 materials.²⁵⁶ The films also showed an enhanced photocatalytic performance on the photodegrading RhB compared to the SnS_2 nanoplatelets synthesized by Du et al.²⁵² In addition, improved field emission performance with a turn-on voltage of 6.9 V/ μm was observed. These improved performances were attributed to the atomic scale morphology of the films.

Apart from the above chemical reaction synthesis of the metal chalcogenides, GeS nanosheets with lateral dimension of 40–100 μm and thickness of 30–50 nm were prepared by vapor deposition method.^{249b} To synthesize the nanosheets, GeS powder was sublimated into gaseous GeS molecules at temperature of 400–500 $^{\circ}\text{C}$, rather than decomposing into Ge or S atoms, and then the GeS vapor carried by 10–30 sccm Ar gas at a vacuum of 20–40 Torr was deposited onto Si or SiO_2/Si substrate kept at 290–330 $^{\circ}\text{C}$. It was found that the growth of high-quality GeS nanosheets was subject to strong influences of the diffusion of gaseous source materials through the boundary layer of gas flows. The diffusion was found to be the rate-determining step of the nanosheet growth under the experimental conditions, with a rapid growth rate of 3–5 $\mu\text{m}/\text{min}$. The diffusion flux was dependent on the partial pressure of source material vapor, the flow rate of the carrier gas, and the total pressure in the synthetic system. The boundary layer diffusion mechanism in the growth of GeS nanosheets is in stark contrast with the synthesis of other nanomaterials, such as nanowires, nanotubes, and graphene, which is typically reaction-limited. The diffusion-limited mechanism is also substantially different from the vapor deposition growth of high-quality thin films which also is typically reaction-limited. However, when the substrate was kept at a lower temperature, for example at 270 $^{\circ}\text{C}$, the growth of GeS nanosheets was not limited by the boundary layer diffusion, but the growth reaction instead, and the quality of the such grown GeS nanosheets was poorer than that grown at a higher substrate temperature.

4.3. Structural and Electronic Properties of Layered Group-III Metal Chalcogenides

Similar to the group just discussed above, the layer-structured group III–VI semiconductors, such as InSe, GaS, and GaSe, generally referred to as layered (GaSe-type) chalcogenides, have attracted considerable attention and show promise in photovoltaic, optoelectronic, nonlinear optical, and terahertz (THz) generation and tuning devices. Their 2D peculiarity is caused by the high anisotropy of the interlayer and intralayer bonds. Its crystal structure consists of covalently bonded stacks of four atomic layers. For example, Se–Ga–Ga–Se, which are held together by weak van der Waals interactions. Depending on how the quadruple layers stack on top of each other, there are typically three different crystal structures²⁵⁷ (β , ϵ , and γ) (Figure 12); ϵ and γ phases show close similarity of crystallographic structures but with different atoms in the primitive cell (e.g., four Ga and four Se for ϵ polytype as well as

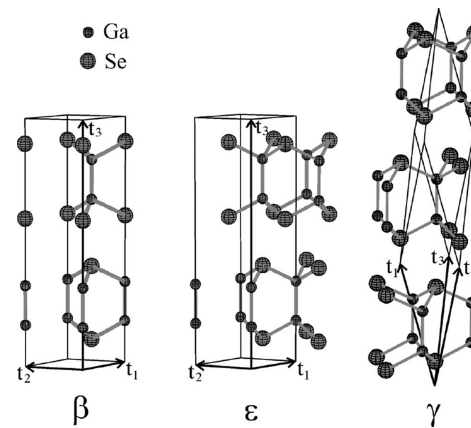


Figure 12. Unit (primitive) cells for β -GaSe (left), ϵ -GaSe (middle), and γ -GaSe (right). Reproduced with permission from ref 257. Copyright 2003 American Physical Society.

β polytype, two Ga and two Se for γ polytype). The polytypes can be identified using Raman or infrared spectroscopy. Both the β and the ϵ polytypes have a unit cell which extends over two layers and contains four formula units. The only difference is the relationship between two adjacent layers. Here the vertical translation is followed by a 60° rotation for the β phase and followed by an in-plane translation for the ϵ phase, leading to an equivalent relationship to each other in the β phase but a different one in the ϵ phase.²⁵⁸ A single tetralayer consists basically of a 2D structure, with the point group D_{3h}^1 .²⁵⁹ The β polytype has the D_{6h}^4 point group and γ polytype has the C_{3v}^5 space group.^{260,261} However, the polytypism has a rather limited effect on the electronic properties of the same compound. Except in the case of GaSe where electronic structure differences have been observed which are due to charge transfer between adjacent interlayers originating from ionic layer–layer bonds.²⁶² In the case of GaSe, the band structure of the β and ϵ polytypes are very similar but that of the γ polytype is different.²⁵⁷ Despite the polytypism, the experimental band gap of these polytypic GaSe compounds is approximately 2.1 eV.²⁶¹ It originates mainly from the Ga–Ga dimer geometry present in all the polytypes.²⁶³ The bond distances of the hexagonal layered GaS structure for the Ga–Ga and Ga–S are 2.48 Å and 2.37 Å, respectively. Accordingly the thickness of one formula unit is approximately 0.75 nm (Table 2); those for hexagonal layered GaSe are 2.45 Å for the Ga–Ga bond, 2.46 Å for the Ga–Se, and 0.79 nm for the unit thickness.²⁶⁴

Bulk GaSe has a direct band gap of approximately 2.1 eV with transition at the Γ point.²⁶⁵ Both direct- and indirect-gap excitons were observed in GaSe with the indirect excitons having slightly lower energies (approximately 25 meV). There are two- and three-dimensional types of excitons in GaSe. The 2D exciton is associated with the indirect transition and is characterized by the effective mass tensor having a very large value along the (unique) z axis, and the 3D exciton has an approximately isotropic effective mass, with a Bohr radius of 31 Å.²⁶⁶

GaSe is also a material with great potential for nonlinear optical applications.²⁶⁷ This is due to its wide transparency range of 0.65 – 18.0 μm with an absorption coefficient less than 0.3 cm⁻¹ and a large nonlinear coefficient d_{22} (10.6 μm) = 86 ± 17 pm/V, corresponding to $(2.0 \pm 0.4) \times 10^{-7}$ esu. These features may facilitate the practical implementation of GaSe in

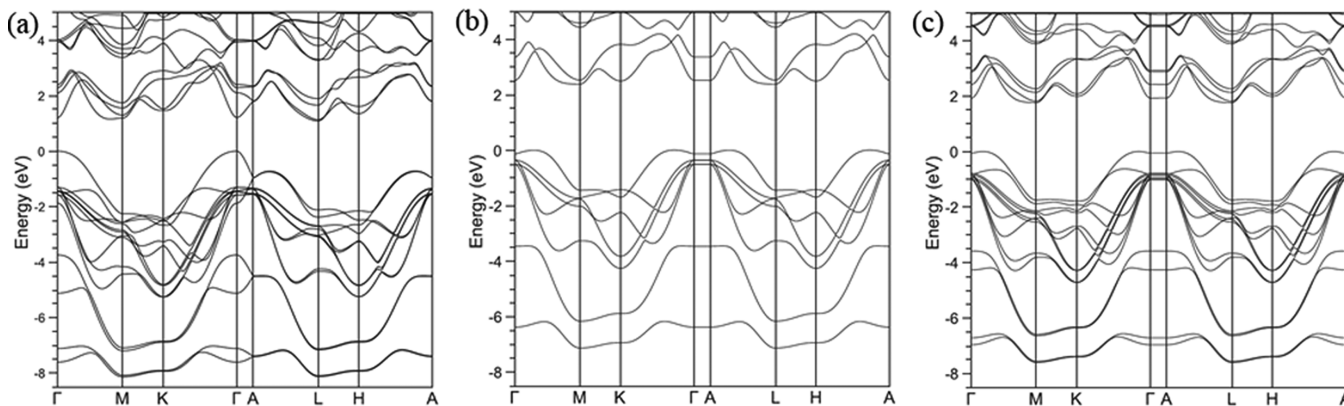


Figure 13. Layer-dependent band structures of GaSe calculated using a DFT-LDA method. (a) Bulk GaSe, (b) a single GaSe tetralayer, and (c) two GaSe tetralayers. The zero of the energy scale was adjusted to the valence band maximum. The lowest two Se s bands are not shown. Although the energy band dispersion of the 2D system along the A-H direction has no physical meaning, all the band structure plots were made over the 3D Brillouine zone to make the direct comparison between bulk and thin structures. Reproduced with permission from ref 271. Copyright 2011 American Physical Society.

nonlinear devices and THz (1 THz = 10^{12} Hz, corresponding to a quantum energy of 4.1 meV) generation and tuning devices.²⁶⁸ However, one challenge is that the mechanical hardness of GaSe should be enhanced.

GaS possesses an indirect gap at approximately 2.59 eV and a direct band gap at approximately 0.45 eV higher in energy.²⁶⁹ By using optical absorption and piezoreflectance measurements, Ho et al. suggested that GaS single crystals synthesized by the chemical vapor transport method are an indirect semiconductor with a gap of approximately 2.53 eV at room temperature. Also the CBM is positioned at the M point while the VBM is at the Γ point. In addition, the indirect gap transition comes from the mixed states of the Ga–S and S–S bonds.²⁷⁰

4.4. Electronic Properties of Single Tetralayer GaSe

It was reported that the electronic structures of layered GaSe crystals are dependent on the number of GaSe tetralayers²⁷¹ as well as the sizes of GaSe particles.²⁷² Calculations using the DFT local density approximation (LDA) (DFT-LDA) method²⁷¹ showed that unlike the bulk crystal, the VBM of the single GaSe tetralayer is not located at the Γ point, but is shifted to the K and M points. The CBM is located at the M point (Figure 13). The highest occupied energy band is formed by the p_z and s orbitals of the Se and Ga atoms. Furthermore, the addition of the second tetralayer could lead to a splitting of the energy bands due to the interlayer interactions. The splitting of the energy bands with an increase in the tetralayers shifts the top of valence band to the Γ point. The result of such a shift changes the band gap value. The 2D thin GaSe crystals have a larger band gap than bulk GaSe, and the calculated difference between the band gaps of a single tetralayer and bulk GaSe is 1.55 eV.

4.5. Synthesis of Layered Group-III Metal Chalcogenides

With respect to non-2D nanostructures, there are more reports on the synthesis of nanostructured GaSe, such as nanowires²⁷³ and nanowalls,²⁷⁴ than on GaS structures.^{274–277} Hexagonal GaS nanobelts with a width of 20–50 nm and a thickness of a few nanometers were prepared by the thermal evaporation of S and Ga precursors using Au as the catalyst.²⁷⁸ It was reported that the Au catalyst was the energetically favored site for the absorption of Ga and S vapor to form the stable GaS phase. The growth direction of the nanobelts was along the [002] axis and the stacking of the GaS unit cells comprised monolayers of

S–Ga–Ga–S along the *c* axis. Field-emission investigations showed that the GaS nanobelts had a low turn-on field of 2.9 V/ μ m and a high field-enhancement factor of approximately 2.0×10^4 . However, to date, there are only a few reports^{279–281} addressing monolayer or few-layer 2D group-III metal chalcogenides. One of these reported on isolating 2D GaS and GaSe sheets from bulk materials by mechanical exfoliation. The thickness of the sheets was measured by atomic force microscopy.²⁷⁹ The field-effect characteristics of these single GaS or GaSe sheets were further investigated.²⁸¹ Built on a SiO₂ dielectric layer, the GaS single-sheet FETs show *n*-type behavior with a mobility of $0.1 \text{ cm}^2/(\text{V s})$ and an on/off ratio of 10^4 . On the other hand, the GaSe material exhibited *p*-type behavior with a mobility of $0.6 \text{ cm}^2/(\text{V s})$ and an on/off ratio of 10^5 . The mobilities are comparable to that of single-layer MoS₂ FETs built on SiO₂. The field-effect properties might be improved by reducing trapping and impurity states at the channel interface and improving source/drain electrical contacts. Another report showed that photodetectors consisting of mechanically exfoliated few-layer GaSe nanosheets exhibited a higher responsivity of 2.8 A/W and a higher external quantum efficiency of 1367% at 254 nm than other 2D nanosheet devices, such as MoS₂ and graphene.²⁸⁰

5. VAN DER WAALS EPITAXY OF LAYERED METAL CHALCOGENIDES

A unique characteristic of 2D metal chalcogenides is that the interlayer interactions along the crystallographic *c* axis consist mainly of weak van der Waals forces, stemming from the chemically saturated chalcogen atoms. As a result, there is no dangling bond at the layer-terminated surfaces and almost no strain between two layered compounds and interfaces between such materials, irrespective of the size of the lattice mismatch. This feature has significant implications for the properties of optoelectronic devices since the interface states typically have critical impact on both the electrical and optical properties at the junctions.

Epitaxy growth is a method of depositing a monocrystalline film on a monocrystalline substrate. It includes liquid phase epitaxy, vapor phase epitaxy, and MBE. MBE is a technique for producing high-quality epitaxial structures made of semiconductors, metals, or insulators with monolayer control at UHV. In MBE, ultrapure elements are heated in separate

effusion cells to create a “molecular beam” of a material; the gaseous elements then condense onto a substrate, subsequently reacting with each other to form epitaxial films. The resulting gallium arsenide, indium phosphide, nitrides, and diamond epitaxial films have a number of technologically important uses including quantum-well lasers for semiconducting systems, and giant magneto-resistance for metallic systems. Despite the conceptual simplicity, an essential requirement for the production of high-quality epitaxial layers is that the substrate and the epilayer must have the same symmetry and very nearly the same lattice constant. Any deviation from these conditions produces a heterointerface with strain and dislocations which degrades the performance of the device. The strain energy in heteroepitaxy (i.e., when a material is deposited over a different substrate) due to the difference in lattice constants is an increasing function of the growth thickness. Typically, this energy is low enough to allow a pseudomorphic, layer-by-layer growth in the first stages. Here the in-plane lattice constant of the overlayer adapts to that of the substrate. However, as growth proceeds, a critical thickness is reached above which the strain energy is relaxed through formation of misfit dislocations or the development of three-dimensional islands.

The van der Waals epitaxy first introduced by Koma et al.²⁸² can almost remove the lattice matching constraint when layered compounds (Figure 14), such as metal chalcogenides, are

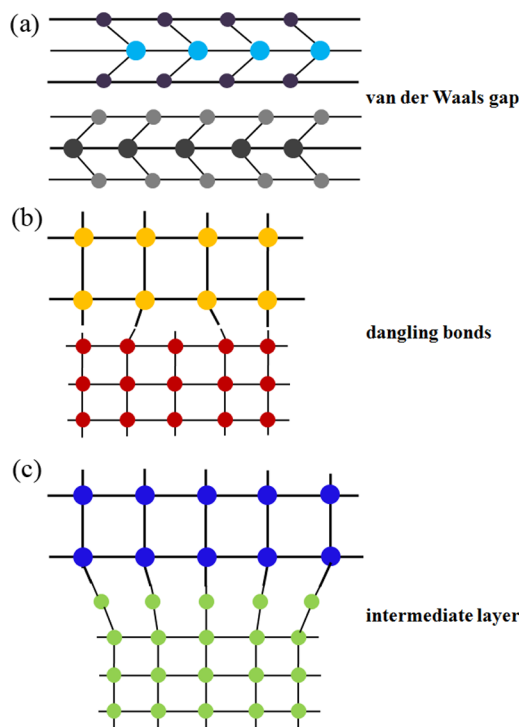


Figure 14. Interfaces connected by (a) a van der Waals gap, (b) covalent bonds, and (c) ionic bonds.

grown onto the cleaved face of other layered materials having no dangling bonds; this is possible even under the existence of a lattice mismatch as large as 50%.^{283,284} van der Waals epitaxy of layered materials can also be grown on an ordinary substrate, such as GaAs²⁸⁵ and Si,²⁸⁶ if the surface dangling bonds on the substrate are regularly terminated. In most cases, the heterointerface is atomically abrupt and epitaxial layers are formed which grow with their bulk lattice constants.²⁸⁷

By using van der Waals epitaxy, one, two, and few unit layers of metal chalcogenides can be formed in a layer-by-layer manner.^{224,270,288} For example, SnSe₂ and SnS₂ films were grown on different layered substrates such as HOPG and MoS₂.²²⁴ Using coevaporation of Sn and the respective chalcogenide (FeS₂ for S and SnSe₂ for Se) on HOPG from thermally heated Knudsen cells, triangular shaped SnS₂ islands were formed and aligned to each other in a more ideal layer-by-layer mode than a SnSe₂ layer which exhibited round structures without any alignment. The different growth behaviors were attributed to the different surface diffusion rates of the materials due to the growth temperatures. These are relevant to the different thermal stabilities of the materials; for SnS₂ this is around 500 °C and that for SnSe₂ at about 350 °C. By using (NH₄)₂MoS₄ dissolved in DMF as the precursor, MoS₂ thin films with a thickness of 2 - 5 nm were successfully synthesized on a graphene surface²⁸⁹ (Figure 10a).

There have also been studies on the interface electronic properties of the van der Waals epitaxial heterojunctions.²⁹⁰ Investigation using X-ray standing-wave techniques showed that the interface structure of ultrathin γ -GaSe films grown on hydrogen-terminated Si(111), 7×7 -Si(111), and $\sqrt{3} \times \sqrt{3}$ Ga-Si(111) surfaces by MBE consists of a GaSe half-layer.²⁸⁶ The Ga atoms were covalently bonded with the Si top atoms of the substrates. Beyond the interface, the growth proceeded layer-by-layer and not in an atomic-plane-by-atomic-plane fashion. The first complete layer above the interface was almost relaxed with respect to the Si substrate. It was reported that a interface-induced gap states (IFIGSs) continuum is the primary mechanism that determines the band lineup at abrupt interfaces involved layered compounds.²⁸³ The character of IFIGSs derived from the bulk bands change across the band gap from more *donor-like* near to the valence band to predominantly *acceptor-like* closer to the conduction band. Although there is no strong bonding between the epilayer and the substrate, the van der Waals interaction at the heterointerface of two materials with different lattice constants can result in a periodic distortion. This induces a unique Moiré pattern as observed by STM.^{291,292} Actually, the interaction at heterointerfaces relies on both the layered compounds and the substrate. For example, the interaction of graphene or monolayer *h*-BN with the underlying substrate is dependent on the chemical activity of the substrate.^{293–295} The van der Waals epitaxy could be used for achieving controllable growth of the metal chalcogenide sheets for device fabrication.

6. SILICENE AND GERMANENE

6.1. Structural and Electronic Properties of Pristine Silicene and Germanene

The structural and electronic properties of the group-IV element graphene-like 2D sheets, such as those formed from Si and Ge, have attracted interest both for their fundamental physical and chemical properties and for their technological applications both current and envisioned for the future. 2D Si and Ge sheets are expected to offer an easily implemented alternative for the enhancement of the performance and scalability of the present silicon-based electronics. Silicene and germanene have 2D hexagonal lattices. Even before the isolation of graphene, first-principles local-density functional methods, based on the minimization of the total energy, predicted that in contrast with the planar honeycomb lattice of

graphene a buckled honeycomb structure of Si and Ge could exist.^{30,296}

On the basis of the first-principles calculations of structural optimization, phonon modes, and finite temperature molecular dynamics, it was reported that although the planar and high-buckled structures of Si and Ge are unstable (Figure 15), the

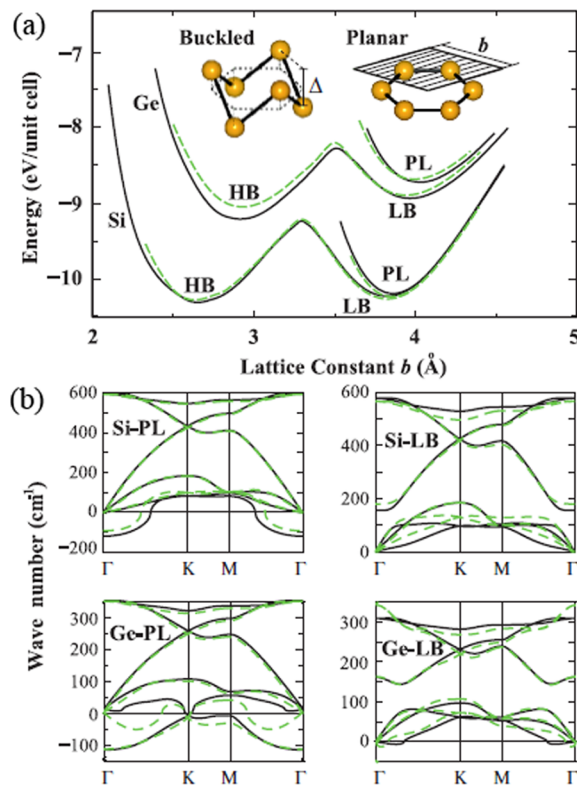


Figure 15. (a) Energy versus hexagonal lattice constant of 2D Si and Ge calculated for various honeycomb structures. Black and dashed green curves of energy were calculated by LDA using PAW potential and ultrasoft pseudopotentials, respectively. Planar and buckled geometries together with buckling distance (Δ) and lattice constant of the hexagonal primitive unit cell b are shown by inset. (b) Phonon dispersion curves obtained by force-constant and linear response theory are presented by black and dashed green curves, respectively. Reproduced with permission from ref 32. Copyright 2009 American Physical Society.

low-buckled (LB) honeycomb structures can be stable with an equilibrium buckling of Δ_{LB} of 0.044 nm.³² The band structures in the LB configurations of Si and Ge are ambipolar, and their charge carrier can behave like a massless Dirac fermion at the K point because of the π and π^* bands that linearly cross at the Fermi level. It also was found that the electronic and magnetic properties of silicene and germanene nanoribbons show size and geometry dependence.^{33,297} By using the ABINIT software DFT package with pseudopotentials and a plane wave basis set, the Fermi velocities in the vicinity of the Dirac point were estimated to be 6.3×10^5 m/s, 5.1×10^5 m/s and 3.8×10^5 m/s for graphene, silicene, and germanene, respectively.²⁹⁸ Most of the other known features of silicene and germanene resemble those of graphene. However, the unique features of silicene have the potential to provide a new future for the electronics industry, which is currently Si-based.

The sp^3 hybridization present in silicon, which leads to the common covalent Si–Si bonds, is the most favorable

configuration with respect to the sp^2 or the mixed sp^2 - sp^3 orbitals. Guzman-Verri et al.²⁹⁹ derived a TB Hamiltonian of buckled silicene from the structure of a monatomic sheet of Si(111) and determined, based on a second-nearest neighbor sp^3 orthogonal tight-binding model, that the silicene is a zero band gap semiconductor with electrons that behave like massless Dirac fermions around the K point. Using the generalized gradient approximation (GGA) functional, Kara et al.⁴² also reported that the LB structure is slightly preferred over a high-buckling one. The presence of buckling suggests a clear preference for sp^3 rather than sp^2 hybridization. Wang³⁰⁰ performed a comparative DFT study on the orbital hybridization behaviors of the 2D phases of carbon, silicon, and germanium. The evolutions in lattice configuration and chemical bonding from 3D to 2D structures were investigated by stretching the spacing between the basal layers in their lonsdaleite phases. During the stretching process, there was a transition from sp^3 to sp^2 hybridization in carbon. However, a corresponding transition was not observed in the silicon and germanium phases. Further investigation into the atomic angular-momentum projected density of states and the electronic energy band spectra of the three materials verified that the chemical bonds are sp^3 -like (partial hybridization of s and p_z) in silicene and germanene. The result is the existence of different lattice configurations compared to graphene. In the case of the LB geometry of silicene (germanene), the lattice constant (a) and the nearest neighbor atom–atom distance (d) are 3.86 Å (4.02 Å) and 2.28 Å (2.42 Å), respectively.³⁰¹

The above analyses suggest that the most stable form of a 2D silicon and germanium sheet is buckled due to the larger atom–atom distance-induced weakening of the π – π overlaps. Hence, according to quantum chemistry, the production of siliceous sp^2 -like analogues becomes impossible.³⁰² Despite this, flat germanene^{303,304} and silicene³⁰⁵ structures with sp^2 hybridization were also studied using DFT calculations, within the local density approximation (LDA). It was shown that, unlike the gapless semiconductor silicene, planar germanene is metallic with a low density of states at the Fermi level. Planar silicene, which has sp^2 hybridized atomic orbitals, is a very reactive surface. The reactivity originates from the weak overlap between the $3p_z$ orbitals of the neighboring Si atoms. The weak π bonds can be easily broken on exposure to foreign species such as oxygen and hydrogen and subsequently they go on to form chemical bonds with these. This leads to an sp^2 to sp^3 -like hybridization as observed in bulk Si.³⁰⁵ De Padova et al. reported sp^2 -like hybridization of silicon valence orbitals in silicene nanoribbons grown on a Ag(110) substrate.³⁰⁶ It has been shown that reflection electron energy loss spectroscopy (REELS), which contains features corresponding to discrete losses of energy of the reflected electrons as a function of the electron beam incidence angle, proved useful for investigating the valence orbitals in the silicene nanoribbons. The REELS Si absorption spectra (1.840 keV) revealed the presence of two distinct loss structures attributed to the transitions $1s \rightarrow \pi^*$ (1.835 keV) and $1s \rightarrow \sigma^*$ (1.840 keV). This is based on their intensity dependence on the electron beam incidence angle. Because of the isotropic character of the tetragonal sp^3 Si valence orbitals, the Si $1s \rightarrow \sigma^*\pi^*$ absorption transition is not angular dependent. The results indicate that the valence silicon orbitals in the silicene nanoribbons formed on Ag(110) exhibit sp^2 -like hybridization similar to that of the carbon atomic bonds of graphene. However, such unusual sp^2 -like hybridization, instead of the more usual sp^3 -like hybridization of freestanding

sheets, can most probably be attributed to the Ag(110) substrate.³⁰⁶ On the other hand, the theoretically predicted reactivity of sp^2 -hybridized silicene with foreign chemicals³⁰⁵ contrasts strongly with the remarkable stability observed for pristine silicene nanoribbons grown on Ag(110). The latter showed a strong resistance to oxidation.³⁰⁶ The oxidation process began at very high oxygen exposure levels: approximately 10^4 times higher than a clean Si(111)-(7 \times 7) surface at room temperature. Defects in the silicene sheets were found to enhance oxygen uptake.

6.2. Functionalization of Silicene and Germanene

Similar to the experimental findings that silicene is unreactive to molecular oxygen, based on the binding energy (-2.4 eV) calculated using the DFT generalized-gradient approximation (DFT-GGA) methodology, the adsorption of a single hydrogen atom on LB silicene is thermodynamically unstable. This suggests that the silicene surface is unreactive toward the dissociation of hydrogen.⁴² Despite the chemical inertia of silicene to hydrogen, hydrogenated silicene and germanene, i.e., silicane or germanane (which are analogs of graphane), have been investigated in several studies.^{298,306,308} Houssa et al.³⁰⁸ performed first-principles calculations of silicane and germanane using DFT. The optimization of the structural parameters and total energy calculations were performed within LDA for the exchange-correctional functional using the SIESTS package. Because DFT-LDA consistently underestimates energy band structures compared to the more accurate GW approximation, the hybrid functional Heyd–Scuseria–Ernzerof (HSE), as implemented in the QUANTUM ESPRESSO package, was used for the computation of the energy band structures. The results were compared to the energy gap using the many-body perturbation theory within the G_0W_0 (GW) approximation, as implemented in the ABINIT code. The chairlike and boat-like³⁰⁹ silicane and germanane configurations were determined to be stable. In contrast, the chairlike configuration of graphane was shown to be more stable than the boat-like one. Upon adsorption of hydrogen, because of the transition from sp^2 to sp^3 hybridization of the Si or Ge atoms, an energy gap opens in silicene and germanene (Table 3). Furthermore, the germanane is a direct band gap semiconductor, whereas, depending on their atomic configurations, chairlike and boat-like silicane were determined to be indirect and direct semiconductors, respectively. By using the TB model, Guzman-Verri et al.³¹⁰ determined that the lowest point of the conduction bands occurs at the M point and the highest point of the valence bands occurs at the Γ point of fully hydrogenated silicene. This indicates that silicene is an indirect band gap (approximately 2.2 eV) semiconductor. Using the DFT-GGA approach, Osborn et al.³¹¹ determined that the hydrogenation energy of silicene increases as the hydrogenation ratio increases. It reaches 3.01 eV per hydrogen atom for complete hydrogenation. The partial hydrogenation configuration was determined to be more energetically favorable. There is a small band gap for 25% hydrogenated silicene but no energy band gap for 50% and 75% hydrogenation. This phenomenon indicates that control of the gap using hydrogenation would be difficult experimentally. It was theoretically shown that the half-hydrogenated silicene and germanene *would* exhibit a ferromagnetic semiconductor behavior.^{312,313} Garcia et al.³¹⁴ performed a systematic DFT-GGA investigation of the group-IV elements extending to Sn and fluorinated graphene-like samples. Fluorinated structures were determined to be more

Table 3. Band Gaps of Group-IV Graphene-Like Sheets and Hydrogenated Graphene-Like (Graphane-Like) or Fluorinated Graphene-Like Sheets Are Collected^a

2D sheets	E_g (eV) by DFT-GGA	E_g (eV) by LDA	E_g (eV) by the many-body GW method
graphene (C_2)	0		
graphane (C_2H_2)	3.47 [ref 314]	3.50 [ref 59]	5.40 [ref 33]
fluorographene (C_2F_2)	3.10 [ref 314]	3.07 [ref 314]	3.0 [ref 64]
silicene (Si_2)	0		
silicane (Si_2H_2)	2.11 [ref 314]	2.1 (chairlike, indirect) [ref 308]	3.8 (chairlike, indirect) [ref 308]
		1.6 (boat-like, direct) [ref 308]	2.9 (boat-like, direct) [ref 308]
fluorinated silicene (C_2F_2)	0.70 [ref 314]		
germanene (Ge_2)	0 [ref 314]		
germanane (Ge_2H_2)	0.95 [ref 314]	1.4 (chairlike, direct) [ref 308]	3.5 (chairlike, direct) [ref 308]
		1.3 (boat-like, direct) [ref 308]	2.9 (boat-like, direct) [ref 308]
fluorinated germanene (Ge_2F_2)	0.19 [ref 314]		
Sn_2	0 [ref 314]		
Sn_2H_2	0.45 [ref 314]		
Sn_2F_2	0 [ref 314]		

^aA brief discussion of the computational estimation of the gaps can be found in ref 146 and 285.

energetically stable than the corresponding hydrogenated structures. No band gap was observed for the fluorinated Sn structure. This is in contrast to fluorinated graphene, silicene, and germanene (Table 3).

Morishita et al.^{315,316} performed DFT-GGA investigations of the electronic structures of a double-layer silicene (DL-Si) system with dangling bonds (DBs), saturated DBs by hydrogenation (DL-Si:H) and substitutional doping of phosphorus (P) for the surface Si atoms (DL-SiP). The electronic properties were found to be sensitive to the amount of DBs on the surface of the Si atoms. The band structure and density of states (DOS) of the DL-Si, where all surface Si atoms were three-coordinated (one DB for one Si atom), showed metallic behavior. Saturation of the DBs by hydrogenation and substitutional doping of P led to an indirect band gap of 1.2 eV for DL-Si:H. This is narrower than that of silicene (>2.0 eV), or that of DL-SiP (1.5 eV). If the DBs were partially saturated, the system was predicted to be either *n*-type or *p*-type.

6.3. Synthesis of Silicene Nanosheets

Despite the intense theoretical investigations of the electronic and structural properties of silicene and germanene, there are currently only a few experimental reports on silicene sheets but no experimental report on germanene. This is due to the inaccessibility of samples. The exploration of epitaxial growth of silicon on silver resulted in the formation of Si nanowires on Ag(110) with similar widths (approximately 1.6 nm) and heights (approximately 0.2 nm) but of varying lengths. The Si nanowires were formed by direct-current flashing a piece of Si wafer in a UHV chamber. As observed by STM, the nanowires were all aligned along the [110] direction of the Ag substrate.³¹⁷ These Si nanowires were reinvestigated,³¹ revealing four silicon hexagons in a honeycomb arrangement

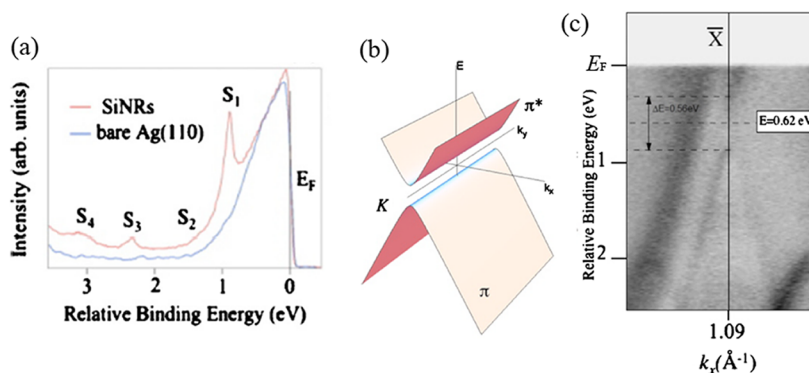


Figure 16. (a) Electron energy distribution curves for bare Ag(110) and for the array of Si nanoribbons. (b) The 1D projection of the π and π^* cones around the Dirac points. (c) Horizontal slice $I(E, k_x)$ along the $[̄10]$ Ag direction integrated on k_y from 0.55 to 0.7 \AA^{-1} for the dense array of Si nanoribbons on Ag(110). Reproduced with permission from ref 318. Copyright 2010 American Institute of Physics.

inside the nanowires. Such a complex structure of the asymmetric nanowires was elucidated using *ab initio* DFT calculations. After full atomic relaxation, the Si honeycomb structure presented a noticeable buckling as observed in the STM image. This is responsible for the asymmetric corrugation in the charge density profile (approximately 0.2 nm). As a result, the silicon nanowires grown on Ag(110) were described as silicene nanoribbons forming an arc with a height of approximately 0.2 nm. This is the first evidence of silicene possibly growing on Ag(110) or even of the physical existence of silicene.

The electronic properties of the silicene nanoribbons grown on Ag(110) were investigated using various techniques.³¹⁸ Angle-resolved photoelectron spectroscopy (ARPES) measurements showed that compared to the surface state of pristine Ag(110), the spectrum of the silicene nanoribbons exhibits prominent electronic states in the proximity of the Fermi level at approximately 0.92, 1.45, 2.37, and 3.12 eV (Figure 16). These states along the Ag [001] direction originated from lateral confinement within the 1.6 nm nanoribbons because they did not disperse at the normal emission as a function of the photon energy. Two branches of highly dispersive Si bands were found to be separated by a gap of approximately 0.5 eV and centered at 0.6 eV below the Fermi level. This is of course reminiscent of the theoretical π^* and π bands of silicene.³² Similar to graphene on different surfaces,³¹⁹ the observed downward shift of the bands was attributed to the charge transfer from the Ag(110) substrate to the silicene nanoribbons. In addition, the opening of the gap was due to the arched honeycomb architecture of the nanoribbons on the substrate. This study suggests that the silicene nanoribbons displayed quantum confined electronic states of 1D character, which were mediated by the silver surface.

On the basis of STM observations, a continuous monolayer silicene sheet was later reported to have been successfully grown on a Ag(111) surface.³²⁰ Under UHV conditions, the Ag(111) substrate was cleaned by several sputtering cycles; this was followed by annealing at 400 °C until a sharp (1×1) pattern of the Ag surface was obtained. The silicene sheet was formed by depositing Si from a piece of Si wafer onto the Ag(111) substrate which was heated at approximately 250 °C. The experimental conditions for producing the silicene sheet were reported to be quite stringent in that the substrate temperature must be maintained between 220–250 °C and the deposition rate of Si must be lower than 0.1 monolayer/min. The STM image revealed a honeycomb structure formed by

two silicon sublattices occupying positions at different heights. The difference of approximately 0.02 nm might possibly indicate $\text{sp}^2\text{-sp}^3$ hybridization. The Si–Si nearest-neighbors distance of 0.19 ± 0.01 nm, derived from the line analysis of the STM image, was approximately 17% shorter than that for bulk Si (0.235 nm), which suggests that the Ag substrate may play a catalytic role in the formation and stabilization of the silicene sheet or there may have been strong interaction between the silicene and the Ag(111) substrate. However, it was suggested by the authors that the weak electronic coupling between the silicene sheet and the Ag(111) substrate was most likely because the epitaxial $(2\sqrt{3} \times 2\sqrt{3})\text{R}30^\circ$ LEED pattern (not shown in the paper) was not observed in the STM images. Recently, De Padova et al.^{43,321} questioned Lalmi et al.'s assignment of their STM results as being in fact silicene. Their reasoning is based on the much smaller Si–Si distance in the STM image than that observed for bulk Si and also the fact that there was no chemical characterization of the sample. This issue has also been raised by other independent groups.^{322,323} However, various Si-based superstructures with different rotations relative to the Ag substrate, including (4×4) , $(2\sqrt{3} \times 2\sqrt{3})\text{R}30^\circ$, $(\sqrt{13} \times \sqrt{13})\text{R}13.9^\circ$, have been observed by STM. It was reported that these strongly depend on the substrate temperature and deposition rate of Si atoms onto the substrate.^{324,325} It should also be noted that according to theoretical calculations, the Si–Si nearest neighbor distance varies between 0.228 and 0.25 nm and the apparent (lateral) Si–Si distance can be as low as 0.189 nm due to buckling in a silicene sheet.³²⁶

In order to provide compelling evidence for the existence of silicene, Vogt et al. performed a systematic investigation of the Si superstructures deposited on Ag(111) using a suite of techniques including STM, ARPES, and LEED in conjunction with DFT calculations.³²¹ They deposited Si atoms on an Ag(111) substrate that was kept at 220–260 °C. By measuring the Si 2p core level and the Ag 4d band emission, they found that the Si/Ag ratio increased linearly with the deposition of Si. The LEED results confirmed a (4×4) symmetry with respect to the bare Ag(111)-(1×1) surface, which is in good agreement with the STM results indicated structures with a periodicity of 1.14 nm (Figure 17). These results suggest formation of a (4×4) Si adlayer, in other words a 2D silicene, on the Ag(111) surface. From the ARPES data it appears that the apex of the Si cone on Ag(111) is approximately 0.3 eV below the Fermi level. This is a result of an interaction with the Ag(111). They also determined the bond angles of the Si atoms

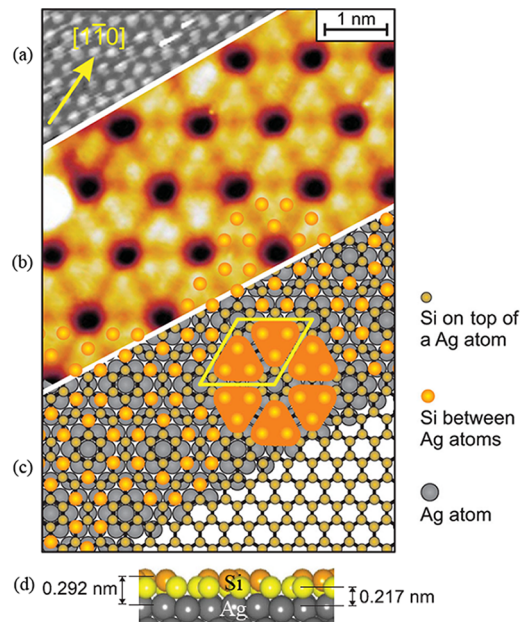


Figure 17. Construction of the atomic structure model for the 2D Si adlayer. (a) Filled-states STM images of the initial clean Ag(111)-(1 × 1) surface. (b) Filled-states STM images of the (4 × 4) silicene sheet on Ag(111). (c) Model of silicene on Ag(111). Si atoms sitting on top of Ag atoms are highlighted as larger orange balls, resembling the measured STM image. In the bottom right corner, the ball-and-stick model for the freestanding silicene layer is shown with a Si–Si distance of 0.22 nm. (d) Side view of a DFT results for silicene on Ag(111). Reproduced with permission from ref 321. Copyright 2012 American Physical Society.

with a view to providing information on the hybridization states. For the six top Si atoms of the (4 × 4) unit cell, the bond angle is approximately 110°, which is close to that of an ideally sp^3 hybridized Si atom of 109.5°. Of the remaining 12 lower Si atoms, six are purely sp^2 hybridized (bond angle of approximately 120°) and six have approximate bond angles between 112° and 118°. This indicates sp^3 - sp^2 hybridization. These different bond angles of the Si atoms result from the displacement of the Si atoms in the z direction which is caused by the interaction with the Ag(111) substrate.

Using STM Feng et al.³²⁷ observed Si superstructures with a periodicity of 1.18 nm. This is almost exactly four times that of the lattice constant of the Ag(111)-(1 × 1) surface, 0.29 nm, or three times that of silicene, 0.38 nm, when Si is deposited on an Ag(111) surface. They concluded that the observed structures were in the form of a (3 × 3) reconstruction with respect to the (1 × 1) silicene lattice. They found that a honeycomb structure and disordered protrusions can coexist at substrate temperatures of 143 °C. In addition, at 227 °C a dense honeycomb structure, silicene, was formed. However, above 327 °C, no silicon structure was observed. Also, with an increase in the coverage of silicon, stacked multilayer silicon structures could also be formed. The similarity of the local density of states between the monolayer silicene and bilayer silicene may indicate weak interactions between the monolayer silicene and the Ag(111) substrate.

Chen et al.³²³ observed a ($\sqrt{3} \times \sqrt{3}$)R30° reconstruction of Si atoms on Ag(111) surface by STM. Pronounced quasiparticle interference patterns originating from intervalley and intravalley scattering of the charge carriers were also observed. On the basis of these observations, a linear energy-

momentum dispersion relation and a Fermi velocity of as large as 10⁶ m/s were derived. These results prove that the quasiparticles in silicene behave as massless Dirac fermions. The derived features are similar to those found for graphene. However, the nature of the electron coupling¹² of the Ag substrate or substrate contribution to the observed characteristics remains unclear.

In addition to these reported superstructures of Si atoms on Ag substrate, there is now also a report of Si superstructures synthesized on a ZrB₂ surface.³²⁸ The reconstructed Si sheet on the ZrB₂ was formed by a surface segregation method from the Si substrate, onto which the ZrB₂ was deposited. A direct π -electron band gap at the Γ point was formed due to buckling of the silicene which was in turn induced by the epitaxial strain with the ZrB₂ surface. On the basis of STM results it was also reported that the electronic properties of the reconstructed Si sheets depended on the local Si phases.³²⁵ It should be noted that further verification of all the reported Si-based superstructures is needed and the interaction between the substrate and deposited Si atoms also needs further investigation. Despite these reports, there is no evidence that a free-standing silicene sheet has been produced so far.

Spherical Si nanomaterials comprised of 2D freestanding Si nanosheets with a thickness of less than 2 nm (Figure 18) were prepared using the CVD process.³²⁹ The X-ray diffraction patterns of the nanosheets suggest a Si diamond-like structure. The Si nanomaterials dispersed in ethanol were a semiconductor with a direct band gap of approximately 2.8 eV and an indirect band gap of approximately 1.73 eV. These Si nanomaterials were synthesized on various substrates such as Si, sapphire, GaN, and quartz using the CVD process in a high flux H₂ environment. In order to grow the Si nanomaterials at 1000 °C, silicon chloride (SiCl₄) was introduced into a horizontal tube under a H₂/Ar atmosphere by bubbling the SiCl₄ with the H₂ carrier gas at a flow rate of 20 sccm. The individual 2D Si nanosheets were formed by the formation of frameworks, first along six different ⟨110⟩ directions normal to the zone axis [111] and then by filling in the spaces between the frameworks along the ⟨112⟩ direction. A high flux of H₂ is the critical factor for the formation of the 2D Si nanosheets. A low flux of H₂ resulted only in Si nanowires whereas a high flux of helium or Ar resulted in the growth of thin films. The Si nanomaterials that were grown on a Si substrate were subsequently dispersed in an ethanol solution, which exhibited a blue emission at 435 nm. The PL was attributed to the enhanced direct band transition at the Γ point of bulk Si in the 2D Si nanosheets.

2D Si-based sheets can also be fabricated using a solution-based method.⁴¹ To synthesize silicon sheets using hexagonal layered calcium disilicide (CaSi₂), Nakamo et al.³³⁰ first doped the CaSi₂ with Mg so that the charge on the negatively charged silicon layers could be reduced. The CaSi_{0.85}Mg_{0.15} was then exfoliated in a solution of propylamine hydrochloride (PA·HCl). Finally, the authors obtained a product with a composition of Si: Mg: O = 7.0: 1.3: 7.5 as determined using X-ray photoelectron spectroscopy. That is, products were Mg-doped monolayer sheets with a predominating ⟨110⟩ orientation and included oxidized Si. To synthesize oxygen-free silicon nanosheets, Okamoto et al.³³¹ exfoliated a layered polysilane (Si₆H₆) through a reaction with *n*-decylamine. This reaction led to nanosheets with the Si(111) planes covalently bound to amines. The thickness of the “free-standing” sheets was less than 2 nm. The nanosheets exhibited PL emission at 435 nm, which clearly indicates that the nanosheets are direct

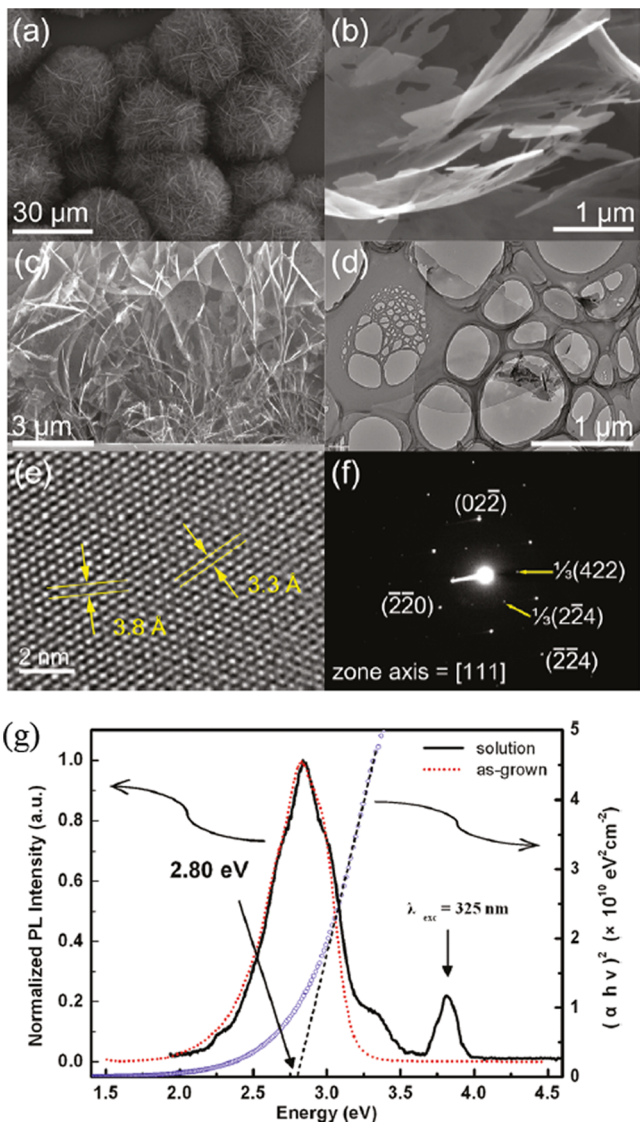


Figure 18. (a, b) Typical SEM images of Si-based nanospheres grown on a Si substrate by CVD. (c) SEM image of cross-sectioned substrate. (d) Typical TEM image of Si nanosheets contained in the nanospheres. (e) High-resolution TEM image of Si nanosheets, showing the single-crystalline nature of the Si nanosheets. (f) Selected area electron diffraction pattern of Si nanosheets, indicating that its stacking axis is in the [111] direction, and showing the $\frac{1}{3}(422)$ forbidden spots. (g) Room-temperature PL spectra of Si-based nanospheres dispersed in an ethanol solution (black, solid) and as-grown Si-based nanospheres (red, dotted) excited by a wavelength of 325 nm (indicated by a vertical arrow) using a He–Cd laser. Two PL emissions at 435 nm are similar to the optical band gap for direct transition of approximately 2.80 eV (blue circle) as calculated from the absorbance measurements. Reproduced with permission from ref 329. Copyright 2011 American Chemical Society.

band gap materials. In addition, monolayer organosilicon nanosheets, $\text{Si}_6\text{H}_x\text{Ph}_{6-x}$, were also synthesized by the reaction of Si_6H_6 with phenyl magnesium bromide.³³² These efforts suggest that silicon-based nanosheets can be obtained by the chemical modification of Si_6H_6 , in which the interlayer interaction is weaker than that of CaSi_2 . However, these efforts also imply that the synthesis of pure 2D silicon nanosheets by solution-based methods is more difficult than the corresponding synthesis of other layered materials.

7. LAYERED BINARY COMPOUNDS OF GROUP-IV ELEMENTS AND GROUP III–V

There is also interest in the 2D honeycomb structures of binary compounds of the group-IV elements and group III–V compounds.^{333–338} On the basis of *ab initio* structure optimization and calculations of phonon modes, Sahin et al.³³³ revealed that for these binary compounds, monolayers of 22 honeycomb structures can be stable in a local minimum on the Born–Oppenheimer surface as either 2D infinite periodic crystals or finite-size flakes (see Figure 3). It was predicted that while SiC, GeC, and SnC are planar, like graphene and BN, as a necessity for stabilization, SnSi, SnGe, and SiGe are all buckled like silicene and germanene. It was found that all the III–V compounds containing the first row elements B, C, or N, have planar stable structures. However, the binary compounds formed from a combination of Al, Ga, In and P, As, Sb were found to be stable in low buckled structure. It should be noted that the above study did not exclude the occurrence of other local minima which may be more energetic than for these 2D honeycomb structures. The atomic structures, elastic, and electronic properties of these stable honeycomb structures were also studied and all the binary compounds were found to be semiconductors with a variety of band gaps (see Figure 3).

Solution-based exfoliation was employed to separate layers of SiC crystals and led to the formation of 2D SiC nanoflakes with thicknesses down to 0.5–1.5 nm. The PL spectra for these ultrathin SiC nanosheets showed a strong light-emitting ability and a quantum-confinement-induced emission peak at 373 nm.³³⁸

The bulk crystals of these materials dominate a great range of applications in the microelectronic and opto-electronics industries. Their diverse properties together with their capabilities of functionalization by vacancy defects or adatoms of these 2D sheets³³⁴ may also prove promising for nanoelectronic applications.

8. VALLEY PHYSICS AND SPIN EFFECT IN MONOLAYERS OF 2D SHEETS

8.1. Valley Physics in Monolayer TMDs

Electronic and spintronic devices exploit either the electric charge or the spin of electrons in semiconductors. Successful manipulation of spin could impact on the exotic field of quantum computing since many of the current proposals envision spin as the quantum bit (qubit) of information.³³⁹ Another property of electrons, namely, their valley degree of freedom (valley index), in a semiconductor where they occupy multiple conduction band minima (valleys) with equal energies but at different positions in momentum space,³⁴⁰ could also be exploited for potential valleytronics applications or valley-based electronic applications, such as valley filler, valley valve, and optoelectronic Hall devices. Recently, a simple scheme based on inversion symmetry breaking was proposed in order to realize the manipulation of the valley index through electric, magnetic, and optical means.^{341–343}

Graphene, with its two prominent K and K' valleys, has been considered theoretically for valley index control.^{341,344} However, the inherent inversion symmetry breaking of the monolayer and bilayer graphene has not yet been realized experimentally. In contrast, the 2D monolayers discussed in this review, such as TMDs,³⁴² silicene, germanene, the binary compounds of the group-IV elements, and the group III–V compounds, all have explicitly broken inversion symmetry. For

instance, monolayer MoS₂ consists of a single layer of Mo atoms sandwiched between two layers of S atoms in a trigonal prismatic structure. Inversion symmetry is broken because the two sublattices are occupied, by one Mo and two S atoms (see Figure 4b) respectively. The edges of the conduction and valence bands in monolayer MoS₂ are located at the K points of the 2D hexagonal Brillouin zone. Thus, the two inequivalent valleys constitute a binary index for low energy carriers. Inversion symmetry breaking can give rise to the valley Hall effect where carriers in different valleys flow to opposite transverse edges when an in-plane electric field is applied.³⁴¹ This leads to valley-dependent optical selection rules for interband transitions at K points.³⁴⁴ Under the mechanism of the valley-dependent optical selection rule, it was shown that circularly polarized light can be used to establish valley polarization in monolayer MoS₂ (see Figure 19).^{345,346} It was also found³⁴⁵ that the circularly and linearly polarized components of the luminescence spectra gradually decreased

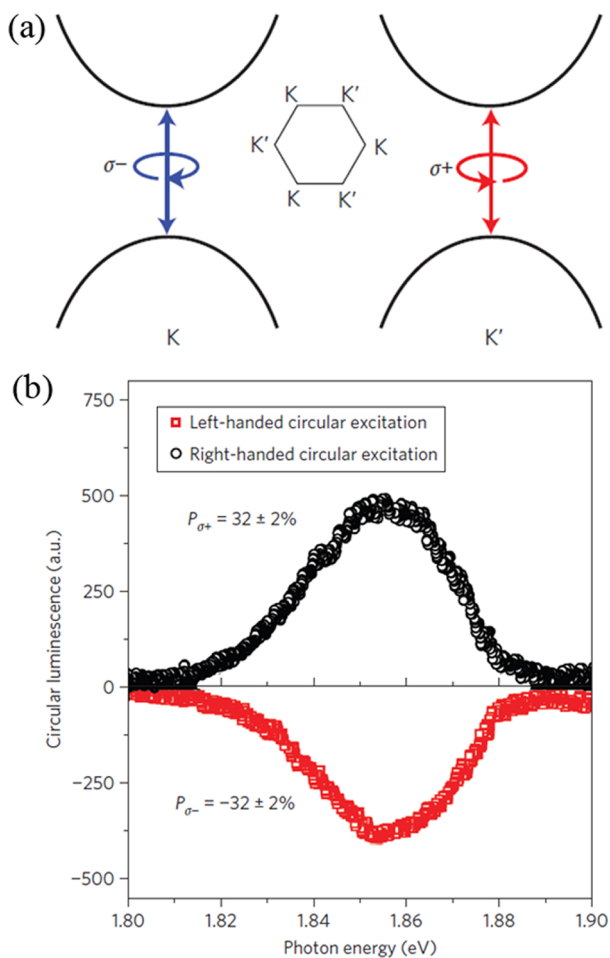


Figure 19. Valley polarization in monolayer MoS₂. (a) Schematic of valley-dependent selection rules at K and K' points in crystal momentum space: left (right)-handed circularly polarized light $\sigma+$ ($\sigma-$) only couples to the band-edge transition at K (K') points for the sake of angular momentum conservation and time reversal symmetry. (b) Polarization resolved luminescence spectra under circularly polarized excitation from a HeNe laser at 1.96 eV and -263°C . Circular polarizations of P were observed along the out-of-plane direction with right- and left-handed circular excitation, respectively. Reproduced with permission from ref 345. Copyright 2012 Nature Publishing Group.

at temperatures above -163°C .³⁴⁵ The broken inversion symmetry effect in these 2D materials are predicted only in thin films with odd numbers of layers and when the inversion symmetry is preserved in films with an even number of layers.³⁴² Another important distinction of TMDs from graphene is that TMDs, such as MoS₂, have a strong spin-orbit coupling (SOC) originating from the d orbitals of the metal atoms.^{347,348} Because of the broken inversion symmetry, spin-orbit interactions split the valence bands. This implies that in monolayer MoS₂, the valley and spin of the valence bands are inherently coupled. Therefore, these 2D systems can be an interesting platform for the exploration of the valley and spin phenomena for those valleytronics and spintronics applications which are absent in graphene.^{344,346}

8.2. Quantum Spin Hall Effect in Silicene and Germanene

Although silicene and germanene have similar electronic properties to graphene, their buckled geometry makes them strikingly different from graphene. This buckling creates new possibilities for manipulating the dispersion of electrons in silicene and germanene³⁰¹ and opening up an electrically controlled sublattice-asymmetry band gap.³⁴⁹ One of the most interesting phenomena is the quantum spin Hall effect (QSHE) or the 2D topological insulator.^{301,350} The QSHE is a new quantum state of matter with a nontrivial topological property. Its scientific importance as a novel quantum state and the technological applications in spintronics is recognized. This novel electronic state, with time-reversal invariance, is characterized by a full insulating gap in the bulk and conducting charge and spin in gapless edge states without dissipation at the sample boundaries. The existence of QSHE was first proposed in 2005 by Kane and Mele for graphene in which the SOC opens a band gap at the Dirac point.³⁵¹ It was theoretically predicted in 2006 (ref 352) and experimentally observed in 2D HgTe-CdTe semiconductor quantum wells³⁵³ and other systems.^{24–27} There have recently been a number of excellent reviews on topological insulators.^{350,354–356} Here we will briefly review the QSHE in silicene and germanene, since these were not addressed in those Reviews.

It was predicted by first-principles calculations that a band gap of 1.55 meV, which corresponds to -255°C , can be opened at the Dirac point in silicene due to SOC.³⁰¹ This is much higher than that of graphene which occurred at an unrealistically low temperature.³⁵⁷ In addition, the spin-orbit band gap will increase to 2.9 meV (corresponding to -239°C) under pressure strain (-6%) without destroying the nontrivial topological properties of silicene. In the case of an LB stable germanene structure, the magnitude of the gap induced by effective SOC for the π orbital at the K point is 23.9 meV, corresponding to 4 °C. These spin-orbit opened energy gaps can be observed experimentally. Furthermore, it was also shown that an external electric field (E_z) perpendicular to the silicene atomic plane produces a tunable band gap in silicene and germanene.³⁴⁹ The interplay at an electric field between the electrically tunable band gap, which is specific to electrons on a honeycomb lattice, and the SOC could induce a transition from a topological insulator to a band insulator in silicene and germanene.^{358,359} As shown in Figure 20a, silicene is a topological insulator for $|E_z| < E_c$ (critical electric field (E_c) of approximately 17 mV/Å), a band insulator for $|E_z| > E_c$, and a semimetal for $|E_z| = E_c$. These results suggest that if an inhomogeneous electric field is applied to a single silicene sheet, the local regions can become a topological insulator,

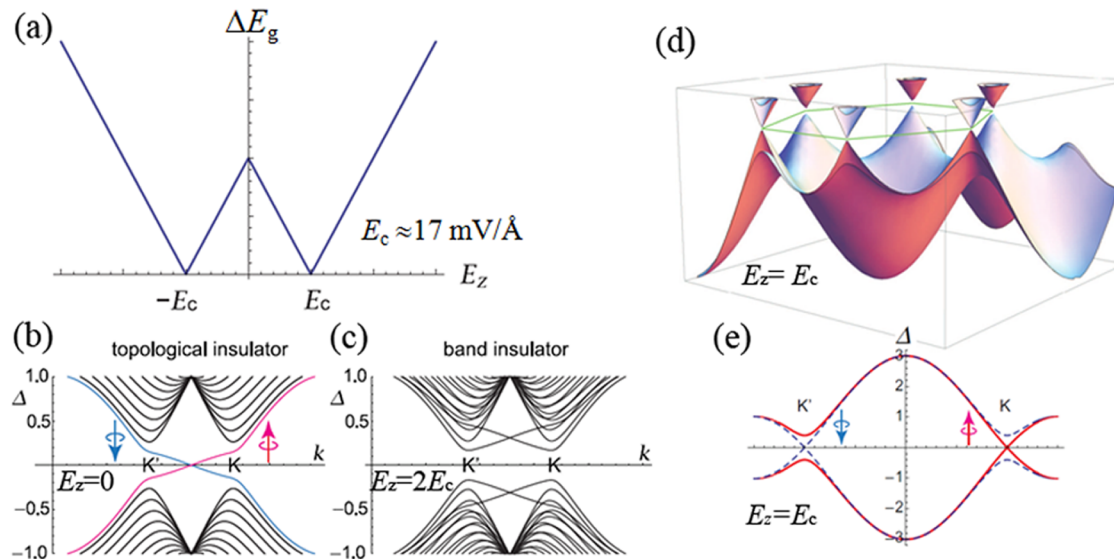


Figure 20. (a) The band gap as a function of the external electric field E_z . (b) At $E_z = 0$, the bands crossing the gap are edge states, demonstrating that it is a topological insulator. There are two edge states since a nanoribbon has two edges (red and blue lines for the left and right edges). (c) At $E_z = 2E_c$ (E_c : critical electric field), all states are gapped, demonstrating that it is a band insulator. (d) A bird's eye view of band structure of silicene at the E_c . Dirac cones are found at six corners of the hexagonal Brillouin zone. (e) The cross section containing a pair of K and K' points at the critical electric field E_c . The solid red (dashed blue) band is for up-spin (down-spin) electrons, which are gapless (gapped) at the K point but gapped (gapless) at the K' point. Reproduced with permission from ref 359. Copyright 2012 IOP Publishing.

band insulator, or metal (Figure 20b–d). These important results open up the possibility for future spintronics applications.

9. CONCLUDING REMARKS AND OUTLOOK

Hopefully in this review we have helped the reader to understand that derived from its 2D honeycomb shape, graphene has unique electronic, optical, mechanical, thermal, and chemical properties. Not only have the fundamental properties of graphene been discovered, but many interesting applications of graphene have also been demonstrated. However, to date, there has been no practical method for the large-scale and scalable production of graphene sheets with fine control over the number and the structure of the layers over an entire substrate. A technique for the transferring of large-scale graphene sheets also needs to be developed. Low-temperature synthesis and catalyst-free synthesis are highly desirable for practical applications. In principle, graphene could be considered as a prototypical material used to investigate the fundamental physics and chemistry of other 2D systems and to explore their applications. The subject of graphene-like 2D crystals is now one of the most active fields of research in materials science, condensed matter physics, and chemistry, and is developing at a rapid pace. Although these 2D systems have been studied for only a couple of years, the findings thus far indicate that these 2D materials either exhibit electronic properties that are strikingly different from graphene or have properties that are similar to graphene. We also know that the physical and chemical properties of these 2D crystals can be modified by chemical doping, by application of strain, by intercalation with different types of atoms and molecules, and by electric fields. Together with graphene³⁶⁰ or the many alternatives to graphene, there is no doubt that these 2D materials with large specific surface areas and versatile and superb electronic and optical properties will soon be potentially useful for an enormous range of applications. These include

electronic circuits, spintronics, light-emitting diodes, nonlinear optical devices, THz generation and detection devices, supercapacitors, lithium ion batteries, solar cells, chemical and biosensors, and catalysts.

Despite the theoretical investigation of the electronic properties of *h*-BN, TMDs, silicene, and germanene, the other fundamental properties, including optical, mechanical, thermal, and chemical properties, of these 2D systems remain unexplored. To date there have only been a few studies on metal chalcogenides in addition to TMDs. The unique properties so far revealed by theoretical studies will speed up more intensive experimental investigations. Compared to the preparation of graphene and *h*-BN, a method for the large-scale growth of continuous single- and few-layer prototypes of these 2D materials is still not currently available. Thus, the most important task now is to make these graphene-like 2D materials with predefined numbers of layers and with large areas. Apart from exfoliation, there are other ways to produce these 2D materials. CVD related methods, surface segregation, van der Waals epitaxy, and chemical reaction may be feasible because there is already positive evidence. For example, the CVD growth of single- and few-layer *h*-BN sheets and few-layer MoS₂ thin films, growth of *h*-BN using surface segregation, and van der Waals growth of MoS₂ and SnS₂ layers.

One of the most pronounced properties of monolayer TMD materials, such as MoS₂ and WS₂, is their direct band gap. The direct band gaps are different not only from graphene but also from their bilayer, few-layer, and bulk phases of TMD counterparts. Within the ballistic regime, the performance of monolayer MX₂ transistors is better than those of the corresponding silicon transistors if a thin high- κ gate dielectric is used.¹⁷⁴ Because of the fact that monolayer MoS₂ is a direct band gap semiconductor, very strong PL emission was observed for mechanically exfoliated monolayer MoS₂ sheets with respect to bilayer and other numbers of MoS₂ sheets. Such a PL phenomenon is not found for crystalline Si. The inversion symmetry breaking, together with spin-orbit coupling, leads to

coupled spin and valley physics in monolayers of TMDs. This makes it possible to control the spin and valley occurrence in these 2D materials. These results indicate that the semiconducting monolayer TMD sheets offer novel and exciting opportunities for semiconductor industries. Despite several experimental studies of 2D MoS₂ sheets, there are only a limited number of experimental studies on the electronic and optical properties of other semiconducting monolayer and few-layer sheets of metal chalcogenides.

Theoretical calculations show that buckled silicene and germanene are more energetically stable than their planar counterparts and show similar electronic properties to those of graphene. Despite the increasing number of theoretical studies on the structures and electronic properties of silicene and germanene, the number of independent experimental investigations of silicene and germanene is very limited. Currently, there is no experimental report on germanene. There are still no freestanding silicene and germanene nanosheets available for the exploration of their intrinsic properties or to really confirm their existence as in the case of graphene. The existence of silicene now appears to be evident through STM observations and the chemical characterization of continuous sheets on Ag(111). However, questions still remain. How does a substrate influence the synthesis, structure, and the intrinsic properties of silicene and other group-IV graphene-like sheets? Is it possible to synthesize large-scale 2D sheets by using methods learned from the production of graphene with scalable dimensions and by the wealth of experience in the synthesis of Si nanowires? The theoretical prediction of the QSHE in silicene and germanene is more realistic than in graphene and its experimental discovery would appear to be imminent once appropriate samples are available. Because modern microelectronics are primarily based on exploiting the properties of Si and an enormous amount of knowledge is available to assist in the design and fabrication of Si-based devices, group-IV graphene-like 2D nanosheets (particularly silicene) might provide a fruitful new avenue of research in Si-based nanoelectronics.

Although the study of graphene-like 2D systems is still in its infancy, the known outstanding properties of such materials provide excellent motivation for expanding research activities in this rapidly emerging field. For example, the Chinese government has just initiated a major program for innovation in 2D crystals technologies. The possible topics for fundamental research are many and include the development of new techniques for synthesizing sheets with predefined numbers of layers and improving the structural quality of the synthesized layers. The exploration of the fundamental physical and chemical properties of monolayer, bilayer, and few-layer sheets; the engineering of interfacial properties between heterojunctions; and the modification of fundamental properties by doping, functionalization, electric field, and strain engineering are all open to investigation. The diverse possibilities for creating new 2D crystals and discovering exotic properties make this field of 2D crystals a fertile one for future investigation and emerging technological applications with precisely tailored properties.

AUTHOR INFORMATION

Corresponding Author

*Address: Department of Polymer Science and Engineering, Zhejiang University, #38 Zheda Road, Hangzhou 310027, China. E-mail: msxu@zju.edu.cn.

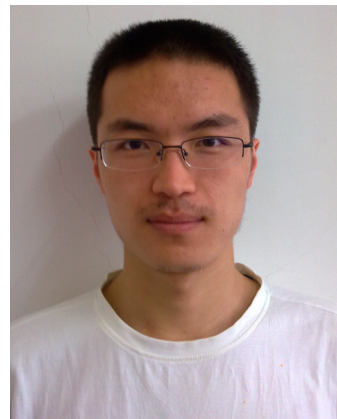
Notes

The authors declare no competing financial interest.

Biographies



Mingsheng Xu obtained his Ph.D. in Department of Electronic Engineering from The Chinese University of Hong Kong in 2003. After obtaining his Ph.D., he worked as a researcher at The University of Tokyo (2003–2007) and at Chiba University (2005–2007), and as an NIMS Postdoc (2007–2008) and ICYS researcher (2008–2011) at National Institute for Materials Science (NIMS), Japan. In 2010, he joined Zhejiang University as a full professor in the Department of Polymer Science and Engineering and a Senior Researcher in the State Key Laboratory of Silicon Materials. His research interests cover two-dimensional nanomaterials, optoelectronics, nanotoxicity, and electronic DNA sequencing.



Tao Liang received his B.S. degree from Tongji University in 2011. He is now a Master Degree candidate in Department of Polymer Science and Engineering, Zhejiang University. His current research interests focus on controllable synthesis of two-dimensional nanomaterials and their applications.



Minmin Shi received his B.S. degree in chemistry from University of Science & Technology of China in 1993. He obtained his Ph.D. degree in material science from Zhejiang University in 2003. Then he joined Department of Polymer Science and Engineering of Zhejiang University as an assistant professor and was promoted to associate professor in 2006. His research interests focus on organic and organic–inorganic hybrid functional materials for electronic and optoelectronic applications.



Hongzheng Chen is a professor in the Department of Polymer Science and Engineering at Zhejiang University. She received her Ph.D. degree (1994) in Polymer Chemistry from the Zhejiang University. Then, she was promoted to a full professor in 1999. She was a visiting researcher at Antwerpen University and Interuniversities MicroElectronic Center (IMEC) in Belgium (1999–2001), and a visiting Professor at Stanford University in 2005 and 2007. Her current research interest focuses on organic (organic/inorganic) optoelectronic materials for photovoltaics, photodetectors, and biosensors applications.

ACKNOWLEDGMENTS

The work was partially supported by the National Natural Science Foundation of China (Grants 50990063, 50973095, and 51011130028), by the Zhejiang Provincial National Science Foundation of China (Youth Talent Program: R4110030), Science and Technology Department of Zhejiang Province (Qianjiang Talent Program: 2011R10077), the Fundamental Research Funds for the Central Universities (No.: 2011QNA4030), and the Program for 14th China-Japan S & T Cooperation (No. 0S2013GR0459). The authors thank the editors of *Chemical Reviews* for their careful reading and language editing of this manuscript.

ABBREVIATIONS

0D	zero-dimensional
----	------------------

1D	one-dimensional
2D	two-dimensional
3D	three-dimensional
ARPES	angle-resolved photoelectron spectroscopy
B–C–N	boron–carbon–nitrogen
CBM	conduction band minimum
CVD	chemical vapor deposition
DBs	dangling bonds
DFT	density functional theory
DL-Si	double-layer silicene
DMF	dimethylformamide
DOS	density of states
E_c	critical electric field
E_g	band gap
E_z	external electric field
FETs	field-effect transistors
h -BN	hexagonal boron nitride
GGA	generalized gradient approximation
HOPG	highly oriented pyrolytic graphite
HMDS	hexamethyldisilazane
H–S–E	Heyd–Scuseria–Ernzerof
IFIGSs	interface-induced gap states
LB	low-buckled
LDA	local density approximation
LEED	low-energy electron-diffraction
LEEM	low-energy electron microscopy
MBE	molecular beam epitaxy
MSA	methanesulfonic acid
MX ₂	metal atoms (M) and chalcogen atoms (X)
ODA	octadecylamine
PEG	Polyethylene glycol
PL	photoluminescence
QSHE	quantum spin Hall effect
REELS	reflection electron energy loss spectroscopy
SOC	spin–orbit coupling
STM	scanning tunnelling microscopy
TB	tight binding
TCNQ	tetracyanoquinodimethane
TEM	transmission electron microscopy
TEM-EDS	transmission electron microscopy-based energy dispersive spectroscopic
THF	tetrahydrofuran
THz	terahertz
TMDs	transition metal dichalcogenides
TTF	tetrathiafulvalene
UHV	ultrahigh vacuum
VBM	valence band maximum

REFERENCES

- (1) Novoselov, K. S.; Geim, A. K.; Morozov, S. V.; Jiang, D.; Katsnelson, M. I.; Grigorieva, I. V.; Dubonos, S. V.; Firsov, A. A. *Nature* **2005**, 438, 197.
- (2) Geim, A. *Nat. Mater.* **2007**, 6, 183.
- (3) (a) Novoselov, K. S.; Falko, V. I.; Colombo, L.; Gellert, P. R.; Schwab, M. G.; Kim, K. *Nature* **2012**, 490, 192. (b) Georgakilas, V.; Otyepka, M.; Bourlinos, A. B.; Chandra, V.; Kim, N.; Christian Kemp, K.; Hobza, P.; Zboril, R.; Kim, K. S. *Chem. Rev.* **2012**, 112, 6156.
- (4) Lin, Y. M.; Dimitrakopoulos, C.; Jenkins, K. A.; Farmer, D. B.; Chiu, H. Y.; Grill, A.; Avouris, P. *Science* **2010**, 327, 662.
- (5) Liu, M.; Yin, X. B.; Ulin-Avila, E.; Geng, B. S.; Zentgraf, T.; Lu, L.; Wang, F.; Zhang, X. *Nature* **2011**, 474, 64.
- (6) Kim, K. S.; Zhao, Y.; Jang, H.; Lee, S. Y.; Kim, J. M.; Kim, K. S.; Ahn, J. Y.; Kim, P.; Choi, J. Y.; Hong, B. H. *Nature* **2009**, 457, 706.

- (7) Zhu, Y. W.; Murali, S.; Stoller, M. D.; Ganesh, K. J.; Cai, W. W.; Ferreira, P. J.; Pirkle, A.; Wallace, R. M.; Cychoz, K. A.; Thommes, M.; Su, D.; Stach, E. A.; Ruoff, R. S. *Science* **2011**, *332*, 1537.
- (8) El-Kady, M. F.; Strong, V.; Dubin, S.; Kaner, R. B. *Science* **2012**, *335*, 6074.
- (9) Yang, X.; Xu, M. S.; Qiu, W. M.; Chen, X. Q.; Deng, M.; Zhang, J. L.; Iwai, H.; Watanabe, E.; Chen, H. Z. *J. Mater. Chem.* **2011**, *21*, 8096.
- (10) Gao, Y.; Chen, X.; Xu, H.; Zou, Y.; Gu, R.; Xu, M. S.; Jen, A. K. Y.; Chen, H. Z. *Carbon* **2010**, *48*, 4475.
- (11) Deng, M.; Yang, X.; Silke, M.; Qiu, W. M.; Xu, M. S.; Borghs, G.; Chen, H. Z. *Sensors Actuators B: Chem.* **2011**, *158*, 176.
- (12) Xu, M. S.; Fujita, D.; Hanagata, N. *Small* **2009**, *5*, 2638.
- (13) Garaj, S.; Hubbard, W.; Reina, A.; Kong, J.; Branton, D.; Golovchenko, J. A. *Nature* **2010**, *467*, 190.
- (14) Xu, M. S.; Gao, Y.; Yang, X.; Chen, H. Z. *Chin. Sci. Bull.* **2012**, *57*, 3000.
- (15) Rümmeli, M. H.; Rocha, C. G.; Ortmann, F.; Ibrahim, I.; Sevincli, H.; Börrnert, F.; Kunstmüller, J.; Bachmatiuk, A.; Pötschke, M.; Shiraishi, M.; Meyyappan, M.; Büchner, B.; Roche, S.; Cuniberti, G. *Adv. Mater.* **2011**, *23*, 4471.
- (16) Kim, K.; Choi, J. Y.; Kim, T.; Cho, S. H.; Chung, H. J. *Nature* **2011**, *479*, 338.
- (17) Fujita, D. *Sci. Technol. Adv. Mater.* **2011**, *12*, 044611.
- (18) Park, J.; Mitchel, W. C.; Grazulis, L.; Smith, H. E.; Eyink, K. G.; Boeckl, J. J.; Tomich, D. H.; Pacley, S. D.; Hoelscher, J. E. *Adv. Mater.* **2010**, *22*, 4140.
- (19) Xu, M. S.; Fujita, D.; Sagisaka, K.; Watanabe, E.; Hanagata, N. *ACS Nano* **2011**, *5*, 1522.
- (20) Wilson, J. A.; Yoffe, A. D. *Adv. Phys.* **1969**, *18*, 193.
- (21) Osada, M.; Sasaki, T. *Adv. Mater.* **2012**, *24*, 210.
- (22) Hozoi, L.; Siurakshina, L.; Fulde, P.; van der Brink, J. *Sci. Rep.* **2011**, *1*, 65.
- (23) Golberg, D.; Bando, Y.; Huang, Y.; Terao, T.; Mitome, M.; Tang, C. C.; Zhi, C. Y. *ACS Nano* **2010**, *4*, 2979.
- (24) Zhang, H. J.; Liu, C. X.; Qi, X. L.; Dai, X.; Fang, Z.; Zhang, S. C. *Nat. Phys.* **2009**, *5*, 438.
- (25) Tao, H.; Liang, D.; Qiu, R. L.; Gao, X. P. A. *ACS Nano* **2011**, *5*, 7510.
- (26) Lang, M. R.; He, L.; Xiu, F. X.; Yu, X. X.; Tang, J. X.; Wang, Y.; Kou, X. F.; Jiang, W. J.; Fedorov, A. V.; Wang, K. L. *ACS Nano* **2012**, *6*, 295.
- (27) Zhang, H. B.; Yu, H. L.; Bao, D. H.; Li, S. W.; Wang, C. X.; Yang, G. W. *Adv. Mater.* **2012**, *24*, 132.
- (28) Gamble, F. R.; Silbernanagel, B. G. *J. Chem. Phys.* **1975**, *63*, 2544.
- (29) Tang, X. F.; Xie, W. J.; Li, H.; Zhao, W. Y.; Zhang, Q. J.; Niino, M. *Appl. Phys. Lett.* **2007**, *90*, 012102.
- (30) Takeda, K.; Shiraishi, K. *Phys. Rev. B* **1994**, *50*, 14916.
- (31) Aufray, B.; Kara, A.; Vizzini, S.; Oughaddou, H.; Léandri, C.; Ealet, B.; Le Lay, G. *Appl. Phys. Lett.* **2010**, *96*, 183102.
- (32) Cahangirov, S.; Topsakal, M.; Aktürk, E.; Sahin, H.; Ciraci, S. *Phys. Rev. Lett.* **2009**, *102*, 236804.
- (33) Dean, C. R.; Young, A. F.; Meric, I.; Lee, C.; Wang, L.; Sorgenfrei, S.; Watanabe, K.; Taniguchi, T.; Kim, P.; Shepard, K. L.; Hone, J. *Nat. Nanotechnol.* **2010**, *5*, 722.
- (34) Radisavljevic, B.; Whitwick, M. B.; Kis, A. *ACS Nano* **2011**, *5*, 9934.
- (35) Mak, K. F.; Lee, C.; Hone, J.; Shan, J.; Heinz, T. F. *Phys. Rev. Lett.* **2010**, *105*, 136805.
- (36) Radisavljevic, B.; Radenovic, A.; Brivio, J.; Giacometti, V.; Kis, A. *Nat. Nanotechnol.* **2011**, *6*, 147.
- (37) Novoselov, K. S.; Geim, A. K.; Morozov, S. V.; Jiang, D.; Zhang, Y.; Dubonos, S. V.; Grigorieva, I. V.; Firsov, A. A. *Science* **2004**, *306*, 666.
- (38) Rogers, J. A.; Lagally, M. G.; Nuzzo, R. G. *Nature* **2011**, *477*, 45.
- (39) Hochbaum, A. I.; Yang, P. D. *Chem. Rev.* **2010**, *110*, 527.
- (40) Schmidt, V.; Wittemann, J. V.; Gosele, U. *Chem. Rev.* **2010**, *110*, 361.
- (41) Okamoto, H.; Sugiyama, Y.; Nakano, H. *Chem.—Eur. J.* **2011**, *17*, 9864.
- (42) Kara, A.; Enriquez, H.; Seitsonen, A. P.; Lew Yan Voon, L. C.; Vizzini, S.; Aufray, B.; Oughaddou, H. *Surf. Sci. Rep.* **2012**, *67*, 1.
- (43) De Padova, P.; Perfetti, P.; Olivieri, B.; Quaresima, C.; Ottaviani, C.; Le Lay, G. *J. Phys.: Condens. Matter.* **2012**, *24*, 223001.
- (44) Xu, M. S.; Fujita, D.; Gao, J. H.; Hanagata, N. *ACS Nano* **2010**, *4*, 2937.
- (45) Gao, J. H.; Fujita, D.; Xu, M. S.; Onishi, K.; Miyamoto, S. *ACS Nano* **2010**, *4*, 1026.
- (46) Xu, M. S.; Fujita, D.; Hanagata, N. *Nanotechnology* **2010**, *21*, 265705.
- (47) Gao, Y.; Yip, H. L.; Chen, K. S.; O'Malley, K. M.; Acton, O.; Sun, Y.; Ting, G.; Chen, H. Z.; Jen, A. K. Y. *Adv. Mater.* **2011**, *23*, 1903.
- (48) Xu, M. S.; Fujita, D.; Chen, H. Z.; Hanagata, N. *Nanoscale* **2011**, *3*, 2854.
- (49) Gao, J. H.; Sagisaka, K.; Kitahara, M.; Xu, M. S.; Miyamoto, S.; Fujita, D. *Nanotechnology* **2012**, *23*, 055704.
- (50) Castellanos-Gomez, A.; Poot, M.; Steele, G. A.; van der Zant, H. E. J.; Agrait, N.; Rubio-Bollinger, G. *Adv. Mater.* **2012**, *24*, 772.
- (51) Cahangirov, S.; Ataca, C.; Topsakal, M.; Sahin, H.; Ciraci, S. *Phys. Rev. Lett.* **2012**, *108*, 126103.
- (52) Kubota, Y.; Watanabe, K.; Tsuda, O.; Taniguchi, T. *Science* **2007**, *317*, 932.
- (53) Ponomarenko, L. A.; Geim, A. K.; Zhukov, A. A.; Jalil, R.; Morozov, S. V.; Novoselov, K. S.; Grigorieva, I. V.; Hill, E. H.; Cheianov, V. V.; Fal'ko, V. I.; Watanabe, K.; Taniguchi, T.; Gorbachev, R. V. *Nat. Phys.* **2011**, *7*, 958.
- (54) Martin, J.; Akerman, N.; Ulbricht, G.; Lohmann, T.; Smet, J. H.; Von Klitzing, K.; Yacoby, A. *Nat. Phys.* **2008**, *4*, 144.
- (55) Xu, M. S.; Fujita, D.; Chen, P. L.; Ma, X. Y.; Yang, D. R. *Curr. Nanosci.* **2010**, *6*, 219.
- (56) Xu, M. S.; Fujita, D.; Onishi, K. *Rev. Sci. Instrum.* **2009**, *80*, 043703.
- (57) Lee, G. H.; Yu, Y. J.; Lee, C. G.; Dean, C.; Shepard, K. L.; Kim, P.; Hone, J. *Appl. Phys. Lett.* **2011**, *99*, 243114.
- (58) Britnell, L.; Gorbachev, R. V.; Jalil, R.; Belle, B. D.; Schedin, F.; Mishchenko, A.; Georgiou, T.; Katsnelson, M. I.; Eaves, L.; Morozov, S. V.; Peres, N. M. R.; Leist, J.; Geim, A. K.; Novoselov, K. S.; Ponomarenko, L. A. *Science* **2012**, *335*, 947.
- (59) Sofo, J. O.; Chaudhari, A. S.; Barber, G. D. *Phys. Rev. B* **2007**, *75*, 153401.
- (60) Elias, D. C.; Nair, R. R.; Mohiuddin, T. M. G.; Morozov, S. V.; Blake, P.; Halsall, M. P.; Ferrari, A. C.; Boukhvalov, D. W.; Katsnelson, M. I.; Geim, A. K.; Novoselov, K. S. *Science* **2009**, *323*, 610.
- (61) Zhou, J.; Wang, Q.; Sun, Q.; Chen, X. S.; Kawazoe, Y.; Jena, P. *Nano Lett.* **2009**, *9*, 3867.
- (62) Kharche, N.; Nayak, S. K. *Nano Lett.* **2011**, *11*, 5274.
- (63) Jaiswal, M.; Lim, C. H. Y. X.; Bao, Q.; Toh, C. T.; Loh, K. P.; Ozylmaz, B. *ACS Nano* **2011**, *5*, 888.
- (64) Nair, R. R.; Ren, W. C.; Jalil, R.; Riaz, I.; Kravets, V. G.; Britnell, L.; Blake, P.; Schedin, F.; Mayorov, A. S.; Yuan, S. J.; Katsnelson, M. I.; Cheng, H. M.; Strupinski, W.; Bulusheva, L. G.; Okotrub, A. V.; Grigorieva, I. V.; Grigorenko, A. N.; Novoselov, K. S.; Geim, A. K. *Small* **2010**, *6*, 2877.
- (65) Kim, K. K.; Hsu, A.; Jia, X. T.; Kim, S. M.; Shi, Y. M.; Hofmann, M.; Nezich, D.; Rodriguez-Nieva, J. F.; Dresselhaus, M.; Palacios, T.; Kong, J. *Nano Lett.* **2012**, *12*, 161.
- (66) Chen, W.; Li, Y. F.; Yu, G. T.; Li, C. Z.; Zhang, S. B. B.; Zhou, Z.; Chen, Z. F. *J. Am. Chem. Soc.* **2010**, *132*, 1699.
- (67) Ataca, C.; Ciraci, S. *Phys. Rev. B* **2010**, *82*, 165402.
- (68) Tang, Q.; Zhou, Z.; Chen, Z. F. *J. Phys. Chem. C* **2011**, *115*, 18531.
- (69) Krivanek, O. L.; Chisholm, M. F.; Nicolosi, V.; Pennycook, T. J.; Corbin, G. J.; Dellby, N.; Murfitt, M. F.; Own, C. S.; Szilagyi, Z. S.; Oxley, M. P.; Pantelides, S. T.; Pennycook, S. J. *Nature* **2010**, *464*, 571.
- (70) Ci, L. J.; Song, L.; Jin, C. H.; Jariwala, D.; Wu, D. X.; Li, Y. J.; Srivastava, A.; Wang, Z. F.; Storr, K.; Balicas, L.; Liu, F.; Ajayan, P. M. *Nat. Mater.* **2010**, *9*, 430.

- (71) Wei, X. L.; Wang, M. S.; Bando, Y.; Golberg, D. *ACS Nano* **2011**, *5*, 2916.
- (72) Nakamura, J.; Nitta, T.; Natori, A. *Phys. Rev. B* **2005**, *72*, 205429.
- (73) Ding, Y.; Wang, Y. L.; Ni, J. *Appl. Phys. Lett.* **2009**, *94*, 233107.
- (74) Pacilé, D.; Meyer, J. C.; Girit, C. Ö.; Zettl, A. *Appl. Phys. Lett.* **2008**, *92*, 133107.
- (75) Li, L. H.; Chen, Y.; Behan, G.; Zhang, H. Z.; Petracic, M.; Glushenkov, A. M. *J. Mater. Chem.* **2011**, *21*, 11862.
- (76) Lin, Y.; Williams, T. V.; Cao, W.; Elsayed-Ali, H. E.; Connell, J. W. *J. Phys. Chem. C* **2010**, *114*, 17434.
- (77) Coleman, J. N.; Lotya, M.; O'Neill, A.; Bergin, S. D.; King, P. J.; Khan, U.; Young, K.; Gaucher, A.; De, S.; Smith, R. J.; Shvets, I. V.; Arora, S. K.; Stanton, G.; Kim, H. Y.; Lee, K.; Kim, G. T.; Duesberg, G. S.; Hallam, T.; Boland, J. J.; Wang, J. J.; Donegan, J. F.; Grunlan, J. C.; Moriarty, G.; Shmeliov, A.; Nicholls, R. J.; Perkins, J. M.; Grieveson, E. M.; Theuwissen, K.; McComb, D. W.; Nellist, P. D.; Nicolosi, V. *Science* **2011**, *331*, 568.
- (78) Smith, R. J.; King, P. J.; Lotya, M.; Wirtz, C.; Khan, U.; De, S.; O'Neill, A.; Duesberg, G. S.; Grunlan, J. C.; Moriarty, G.; Chen, J.; Wang, J. Z.; Minett, A. I.; Nicolosi, V.; Coleman, J. N. *Adv. Mater.* **2011**, *23*, 3944.
- (79) Zhou, K. G.; Mao, N. N.; Wang, H. X.; Peng, Y.; Zhang, H. L. *Angew. Chem., Int. Ed.* **2011**, *50*, 10839.
- (80) Ni, G. X.; Zheng, Y.; Bae, S.; Tan, C. Y.; Kahya, O.; Wu, J.; Hong, B. H.; Yao, K.; Ozylmaz, B. *ACS Nano* **2012**, *6*, 3935.
- (81) Wang, Y.; Shi, Z. X.; Yin, J. *J. Mater. Chem.* **2011**, *21*, 11371.
- (82) Han, W. Q.; Wu, L. J.; Zhu, Y. M.; Watanabe, K.; Taniguchi, T. *Appl. Phys. Lett.* **2008**, *93*, 223103.
- (83) Warner, J. H.; Rümmeli, M. H.; Bachmatiuk, A.; Büchner, B. *ACS Nano* **2010**, *4*, 1299.
- (84) Zhi, C. Y.; Bando, Y.; Tang, C. C.; Kuwahara, H.; Golberg, D. *Adv. Mater.* **2009**, *21*, 2889.
- (85) Lin, Y.; Williams, T. V.; Connell, J. W. *J. Phys. Chem. Lett.* **2010**, *1*, 277.
- (86) Lin, Y.; Williams, T. V.; Xu, T. B.; Cao, W.; Elsayed-Ali, H. E.; Connell, J. W. *J. Phys. Chem. C* **2011**, *115*, 2679.
- (87) Nag, A.; Raidongia, K.; Hembram, K. P. S. S.; Datta, R.; Waghmare, U. V.; Rao, C. N. R. *ACS Nano* **2010**, *4*, 1539.
- (88) Li, X. S.; Cai, W. W.; An, J.; Kim, S.; Nah, J.; Yang, D. X.; Piner, R.; Velamakanni, A.; Jung, I.; Tutuc, E.; Banerjee, S. K.; Colombo, L.; Ruoff, R. S. *Science* **2009**, *324*, 1312.
- (89) (a) Bae, S.; Kim, H.; Lee, Y.; Xu, X. F.; Park, J. S.; Zheng, Y.; Balakrishnan, J.; Lei, T.; Kim, H. R.; Song, Y. I.; Kim, Y. J.; Kim, K. S.; Özylmaz, B.; Ahn, J. H.; Hong, B. H.; Iijima, S. *Nat. Nanotechnol.* **2010**, *5*, 574. (b) Hesjedal, T. *Appl. Phys. Lett.* **2011**, *98*, 133106. (c) Yamada, T.; Ishihara, M.; Kim, J.; Hasegawa, M.; Iijima, S. *Carbon* **2012**, *50*, 2615. (d) Xu, M. S. Chinese Patents CN201220143736.0, 2012; CN 201220197015.8, 2012; and CN201220234443.3, 2012. (e) Xu, M. S.; Chen, H. Z.; Wu, G.; Shi, M. M.; Wang, M. Chinese Patent CN201010249002.6, 2012.
- (90) Pierson, H. O. *J. Compos. Mater.* **1975**, *9*, 228.
- (91) Rozenberg, A. S.; Sinenko, Y. A.; Chukanov, N. V. *J. Mater. Sci.* **1993**, *28*, 5528.
- (92) Middleman, S. *Mater. Sci. Eng., A* **1993**, *163*, 135.
- (93) Adams, A. C. *J. Electrochem. Soc.* **1981**, *128*, 1378.
- (94) Constant, G.; Feurer, R. *J. Less-Common Met.* **1981**, *82*, 113.
- (95) Auwärter, W.; Suter, H. U.; Sachdev, H.; Greber, T. *Chem. Mater.* **2004**, *16*, 343.
- (96) Müller, F.; Stöwe, K.; Sachdev, H. *Chem. Mater.* **2005**, *17*, 3464.
- (97) Paffett, M. T.; Simonson, R. J.; Papin, P.; Paine, R. T. *Surf. Sci.* **1990**, *232*, 286.
- (98) Nagashima, A.; Tejima, N.; Gamou, Y.; Kawai, T.; Oshima, C. *Phys. Rev. B* **1995**, *51*, 4606.
- (99) Nagashima, A.; Tejima, N.; Gamou, Y.; Kawai, T.; Oshima, C. *Surf. Sci.* **1996**, *357–358*, 307.
- (100) Rokuta, E.; Hasegawa, Y.; Suzuki, K.; Gamou, Y.; Oshima, C.; Nagashima, A. *Phys. Rev. Lett.* **1997**, *79*, 4609.
- (101) Corso, M.; Auwärter, W.; Muntwiler, M.; Tamai, A.; Greber, T.; Osterwalder, J. *Science* **2004**, *303*, 217.
- (102) Morscher, M.; Corso, M.; Greber, T.; Osterwalder, J. *Surf. Sci.* **2006**, *600*, 3280.
- (103) Čavar, E.; Westerström, R.; Mikkelsen, A.; Lundgren, E.; Vinogradov, A. S.; Ng, M. L.; Preobrajenski, A. B.; Zakharov, A. A.; Mårtensson, N. *Surf. Sci.* **2008**, *602*, 1722.
- (104) Shi, Y. M.; Hamsen, C.; Jia, X. T.; Kim, K. K.; Reina, A.; Hofmann, M.; Hsu, A. L.; Zhang, K.; Li, H. N.; Juang, Z. Y.; Dresselhaus, M. S.; Li, L. J.; Kong, J. *Nano Lett.* **2010**, *10*, 4134.
- (105) Song, L.; Ci, L. J.; Lu, H.; Sorokin, P. B.; Jin, C. H.; Ni, J.; Kvashnin, A. G.; Kvashnin, D. G.; Lou, J.; Yakobson, B. I.; Ajayan, P. M. *Nano Lett.* **2010**, *10*, 3209.
- (106) Chatterjee, S.; Luo, Z. T.; Acerce, M.; Yates, D. M.; Johnson, A. T. C.; Sneddon, L. G. *Chem. Mater.* **2011**, *23*, 4414.
- (107) Qin, L.; Yu, J.; Li, M. Y.; Liu, F.; Bai, X. D. *Nanotechnology* **2011**, *22*, 215602.
- (108) Dahal, R.; Li, J.; Majety, S.; Pantha, B. N.; Cao, X. K.; Lin, J. Y.; Jiang, H. X. *Appl. Phys. Lett.* **2011**, *98*, 211110.
- (109) Li, X. S.; Magnuson, C. W.; Venugopal, A.; Tromp, R. M.; Hannon, J. B.; Vogel, E. M.; Colombo, L.; Ruoff, R. S. *J. Am. Chem. Soc.* **2011**, *133*, 2816.
- (110) Vlassiouk, I.; Regmi, M.; Fulvio, P.; Dai, S.; Datskos, P.; Eres, G.; Smirnov, S. *ACS Nano* **2011**, *5*, 6069.
- (111) Sutter, P.; Lahiri, J.; Albrecht, P.; Sutter, E. *ACS Nano* **2011**, *5*, 7303.
- (112) Fujita, D.; Yoshihara, K. *J. Vac. Sci. Technol. A* **1994**, *12*, 2134.
- (113) Fujita, D.; Homma, T. *J. Vac. Sci. Technol. A* **1988**, *6*, 230.
- (114) Suzuki, S.; Pallares, R. M.; Hibino, H. *J. Phys. D: Appl. Phys.* **2012**, *45*, 385304.
- (115) Liu, Z.; Song, L.; Zhao, S. Z.; Huang, J. Q.; Ma, L. L.; Zhang, J. N.; Lou, J.; Ajayan, P. M. *Nano Lett.* **2011**, *11*, 2032.
- (116) Son, M.; Lim, H.; Hong, M. S.; Choi, H. C. *Nanoscale* **2011**, *3*, 3089.
- (117) Lee, K. H.; Shin, H. J.; Lee, J.; Lee, I. Y.; Kim, G. H.; Choi, J. Y.; Kim, S. W. *Nano Lett.* **2012**, *12*, 714.
- (118) Postma, H. W. C. *Nano Lett.* **2010**, *10*, 420.
- (119) Nelson, T.; Zhang, B.; Prezhdo, O. V. *Nano Lett.* **2010**, *10*, 3237.
- (120) Pennisi, E. *Science* **2012**, *336*, 534.
- (121) Garaj, S.; Liu, S.; Branton, D.; Golvochenko, J. A. *arXiv* 1204.4361v2.
- (122) Xu, M. S.; Endres, R. G.; Arakawa, Y. *Small* **2007**, *3*, 1539.
- (123) Tsutsui, M.; Taniguchi, M.; Yokota, K.; Kawai, T. *Nat. Nanotechnol.* **2010**, *5*, 286.
- (124) Merchant, C. A.; Healy, K.; Wanunu, M.; Ray, V.; Peterman, N.; Bartel, J.; Fischbein, M. D.; Venta, K.; Luo, Z.; Johnson, A. T. C.; Drndic, M. *Nano Lett.* **2010**, *10*, 2915.
- (125) He, Y. H.; Scheicher, R. H.; Drigorive, A.; Ahuja, R.; Long, S. B.; Huo, Z. L.; Liu, M. *Adv. Funct. Mater.* **2011**, *21*, 2674.
- (126) Shishidou, T.; Freeman, A.; Asahi, R. *Phys. Rev. B* **2001**, *64*, 180401.
- (127) Takada, K.; Sakurai, H.; Takayama-Muromachi, E.; Izumi, F.; Dilanian, R.; Sasaki, T. *Nature* **2003**, *422*, 53.
- (128) Withers, R. L.; Wilson, J. A. *J. Phys. C: Solid State Phys.* **1986**, *19*, 4809.
- (129) Lee, C.; Li, Q.; Kalb, W.; Liu, X. Z.; Berger, H.; Carpick, R. W.; Hone, J. *Science* **2010**, *328*, 76.
- (130) Laursen, A. B.; Kegnas, S.; Dahl, S.; Chorkendorff, I. *Energy Environ. Sci.* **2012**, *5*, 5577.
- (131) Puthussery, J.; Seefeld, S.; Berry, N.; Gibbs, M.; Law, M. *J. Am. Chem. Soc.* **2011**, *133*, 716.
- (132) Feng, J.; Sun, X.; Wu, C. Z.; Peng, L. L.; Lin, C. W.; Hu, S. L.; Yang, J. L.; Xie, Y. *J. Am. Chem. Soc.* **2011**, *133*, 17832.
- (133) Chatzitheodorou, G.; Fiechter, S.; Kunst, M.; Luck, J.; Tributsch, H. *Mater. Res. Bull.* **1988**, *23*, 1261.
- (134) Ding, S. J.; Zhang, D. Y.; Chen, J. S.; Lou, X. W. *Nanoscale* **2012**, *4*, 95.

- (135) Podberezskaya, N.; Magarill, S.; Pervukhina, N.; Borisov, S. *J. Struct. Chem.* **2001**, *42*, 654.
- (136) Todorova, T.; Prins, R.; Weber, T. *J. Catal.* **2007**, *246*, 109.
- (137) Merki, D.; Hu, X. *Energy Environ. Sci.* **2011**, *4*, 3878.
- (138) Li, Y. G.; Wang, H. L.; Xie, L. M.; Liang, Y. Y.; Hong, G. S.; Dai, H. J. *J. Am. Chem. Soc.* **2011**, *133*, 7296.
- (139) Gourmelon, E.; Lignier, O.; Hadouda, H.; Couturier, G.; Bernède, J. C.; Tedd, J.; Pouzed, J.; Salardenne, J. *Sol. Energy Mater. Sol. Cells.* **1997**, *46*, 115.
- (140) Fortin, E.; Sears, W. M. *J. Phys. Chem. Solids* **1982**, *43*, 881.
- (141) Helveg, S.; Lauritsen, J. V.; Lægsgaard, E.; Stensgaard, I.; Nørskov, J. K.; Clausen, B. S.; Topsøe, H.; Besenbacher, F. *Phys. Rev. Lett.* **2000**, *84*, 951.
- (142) Remskar, M.; Mrzel, A.; Skraba, Z.; Jesih, A.; Ceh, M.; Demšar, J.; Stadelmann, P.; Lévy, F.; Mihailovic, D. *Science* **2001**, *292*, 479.
- (143) Dolui, K.; Pemmaraju, C. D.; Sanvito, S. *ACS Nano* **2012**, *6*, 4823.
- (144) Splendiani, A.; Sun, L.; Zhang, Y. B.; Li, T. S.; Kim, J.; Chim, C. Y.; Galli, G.; Wang, F. *Nano Lett.* **2010**, *10*, 1271.
- (145) Korn, T.; Heydrich, S.; Hirmer, M.; Schmutzler, J.; Schüller, C. *Appl. Phys. Lett.* **2011**, *99*, 102109.
- (146) (a) Eda, G.; Yamaguchi, H.; Voiry, D.; Fujita, T.; Chen, M. W.; Chhowalla, M. *Nano Lett.* **2011**, *11*, 5111. (b) Tongay, S.; Zhou, J.; Ataca, C.; Lo, K.; Matthews, T. S.; Li, J. B.; Grossman, J. G.; Wu, J. Q. *Nano Lett.* **2012**, *12*, 5576.
- (147) Kuc, A.; Zibouche, N.; Heine, T. *Phys. Rev. B* **2011**, *83*, 245213.
- (148) Ma, Y. D.; Dai, Y.; Guo, M.; Niu, C. W.; Lu, J. B.; Huang, B. B. *Phys. Chem. Chem. Phys.* **2011**, *13*, 15546.
- (149) Böker, Th.; Severin, R.; Müller, A.; Janowitz, C.; Manzke, R.; Voß, D.; Krüger, P.; Mazur, A.; Pollmann, J. *Phys. Rev. B* **2001**, *64*, 235305.
- (150) Klein, A.; Tiefenbacher, S.; Eyert, V.; Pettenkofer, C.; Jaegermann, W. *Phys. Rev. B* **2001**, *64*, 205416.
- (151) Ramasubramaniam, A.; Naveh, D.; Towe, E. *Phys. Rev. B* **2011**, *84*, 205325.
- (152) Sanchez-Perez, J. R.; Boztug, C.; Chen, F.; Sudradjat, F. F.; Paskiewicz, D. M.; Jacobson, R. B.; Lagally, M. G.; Paiella, R. P. *Proc. Natl. Acad. Sci. U.S.A.* **2011**, *108*, 18893.
- (153) Johari, P.; Shenoy, V. B. *ACS Nano* **2012**, *6*, 5449.
- (154) Pereira, V. M.; Castro Neto, A. H. *Phys. Rev. Lett.* **2009**, *103*, 046801.
- (155) Choi, S. M.; Jhi, S. H.; Son, Y. W. *Phys. Rev. B* **2010**, *81*, 081407.
- (156) Guinea, F.; Katsnelson, M. I.; Geim, A. K. *Nat. Phys.* **2010**, *6*, 30.
- (157) Yun, W. S.; Han, S. W.; Hong, S. C.; Kim, I. G.; Lee, J. D. *Phys. Rev. B* **2012**, *85*, 033305.
- (158) Zhang, J.; Soon, J. M.; Loh, K. P.; Yin, J. H.; Ding, J.; Sullivan, M. B.; Wu, P. *Nano Lett.* **2007**, *7*, 2370.
- (159) Rao, C. N. R.; Ramakrishna, H. S. S.; Subrahmanyam, K. S.; Maitra, U. *Chem. Sci.* **2012**, *3*, 45.
- (160) Fuhr, J. D.; Saúl, A.; Sofo, J. O. *Phys. Rev. Lett.* **2004**, *92*, 026802.
- (161) He, J. G.; Wu, K. C.; Sa, R. J.; Li, Q. H.; Wei, Y. Q. *Appl. Phys. Lett.* **2010**, *96*, 082504.
- (162) Ataca, C.; Ciraci, S. *J. Phys. Chem. C* **2011**, *115*, 13303.
- (163) Shidpour, R.; Manteghian, M. *Nanoscale* **2010**, *2*, 1429.
- (164) Ma, Y. D.; Dai, Y.; Guo, M.; Niu, C. W.; Zhu, Y. T.; Huang, B. B. *ACS Nano* **2012**, *6*, 1695.
- (165) Castro Neto, A. H.; Novoselov, K. *Rep. Prog. Phys.* **2011**, *74*, 082501.
- (166) Zhou, J.; Wang, Q.; Sun, Q.; Chen, X. S.; Kawazoe, Y.; Jena, P. *Nano Lett.* **2009**, *9*, 3867.
- (167) Wang, H.; Yu, L. L.; Lee, Y. H.; Shi, Y. M.; Hsu, A.; Chin, M. L.; Li, L. J.; Dubey, M.; Kong, J.; Palacios, T. *Nano Lett.* **2012**, *12*, 4674.
- (168) Novoselov, K. S.; Jiang, D.; Schedin, F.; Booth, T. J.; Khotkevich, V. V.; Morozov, S. V.; Geim, A. K. *Proc. Natl. Acad. Sci. U.S.A.* **2005**, *102*, 10451.
- (169) Ghatak, S.; Pal, A. N.; Ghosh, A. *ACS Nano* **2011**, *5*, 7707.
- (170) Fivaz, R.; Mooser, E. *Phys. Rev.* **1967**, *163*, 743.
- (171) Kaasbjerg, K.; Thygesen, K. S.; Jacobsen, K. W. *Phys. Rev. B* **2012**, *85*, 115317.
- (172) Yoon, Y.; Ganapathi, K.; Salahuddin, S. *Nano Lett.* **2011**, *11*, 3768.
- (173) Yin, Z. Y.; Li, H.; Li, H.; Jiang, L.; Shi, Y. M.; Sun, Y. H.; Lu, G.; Zhang, Q.; Chen, X. D.; Zhang, H. *ACS Nano* **2012**, *6*, 74.
- (174) Liu, L. T.; Kumar, S. B.; Ouyang, Y. J.; Guo, J. *IEEE Trans. Electron Devices* **2011**, *58*, 3042.
- (175) Liu, H.; Neal, A. T.; Ye, P. D. *ACS Nano* **2012**, *6*, 8563.
- (176) Hwang, W. S.; Remskar, M.; Yan, R.; Protasenko, V.; Tahy, K.; Chae, S. D.; Zhao, P.; Konar, A.; Xing, H. G.; Seabaugh, A.; Jena, D. *Appl. Phys. Lett.* **2012**, *101*, 013107.
- (177) Podzorov, V.; Gershenson, M. E.; Kloc, C.; Zeis, R.; Bucher, E. *Appl. Phys. Lett.* **2004**, *84*, 3301.
- (178) Fang, H.; Chuang, S.; Chang, T. C.; Takei, K.; Takahashi, T.; Javey, A. *Nano Lett.* **2012**, *12*, 3788.
- (179) Levendorf, M. P.; Kim, C. J.; Brown, L.; Huang, P. Y.; Havener, R. W.; Müller, D. A.; Park, J. *Nature* **2012**, *488*, 627.
- (180) Komsa, H. P.; Kotakoski, J.; Kurash, S.; Lehtinen, O.; Kaiser, U.; Krasheninnikov, A. V. *Phys. Rev. Lett.* **2012**, *109*, 035503.
- (181) Kang, J.; Shin, D.; Bae, S. K.; Hong, B. H. *Nanoscale* **2012**, *4*, 5527.
- (182) Li, H.; Yin, Z. Y.; He, Q. Y.; Li, H.; Huang, X.; Lu, G.; Fam, D. W. H.; Tok, A. I. Y.; Zhang, Q.; Zhang, H. *Small* **2012**, *8*, 63.
- (183) Lee, H. S.; Min, S. W.; Chang, Y. G.; Park, M. K.; Nam, T.; Kim, H.; Kim, J. H.; Ryu, S.; Im, S. *Nano Lett.* **2012**, *12*, 3695.
- (184) Zeng, Z. Y.; Yin, Z. Y.; Huang, X.; Li, H.; He, Q. Y.; Lu, G.; Boey, F.; Zhang, H. *Angew. Chem., Int. Ed.* **2011**, *50*, 11093.
- (185) Jäger-Waldau, A.; Lux-Steiner, M. Ch.; Bucher, E.; Scandella, L.; Schumacher, A.; Prins, R. *Appl. Surf. Sci.* **1993**, *65–66*, 465.
- (186) Regula, M.; Ballif, C.; Moser, J. H.; Lévy, F. *Thin Solid Films* **1996**, *280*, 67.
- (187) Pramanik, P.; Bhattacharya, S. *Mater. Res. Bull.* **1990**, *25*, 15.
- (188) Zabinski, J. S.; Donley, M. S.; Prasad, S. V.; McDevitt, N. T. *J. Mater. Sci.* **1994**, *29*, 4834.
- (189) Hofmann, W. K. *J. Mater. Sci.* **1988**, *23*, 3981.
- (190) Balendhran, S.; Ou, J. Z.; Bhaskaran, M.; Sriram, S.; Ippolito, S.; Vasic, Z.; Kats, E.; Bhargava, S.; Zhuiykov, S.; Kalantar-zadeh, K. *Nanoscale* **2012**, *4*, 461.
- (191) Kim, D.; Sun, D. Z.; Lu, W. H.; Cheng, Z. H.; Zhu, Y. M.; Le, D.; Rahman, T. S.; Bartels, L. *Langmuir* **2011**, *27*, 11650.
- (192) Zhan, Y. J.; Liu, Z.; Najmaei, S.; Ajayan, P. M.; Lou, J. *Small* **2012**, *8*, 966.
- (193) Lee, Y. S.; Zhang, X. Q.; Zhang, W. J.; Chang, M. T.; Lin, C. T.; Chang, K. D.; Yu, Y. C.; Wang, J. T.; Chang, C. S.; Li, L. J.; Lin, T. W. *Adv. Mater.* **2012**, *24*, 2320.
- (194) Liu, K. K.; Zhang, W. J.; Lee, Y. H.; Lin, Y. C.; Chang, M. T.; Su, C. Y.; Chang, C. S.; Li, H.; Shi, Y. M.; Zhang, H.; Lai, C. S.; Li, K. J. *Nano Lett.* **2012**, *12*, 1538.
- (195) Helveg, S.; Lauritsen, J. V.; Lægsgaard, E.; Stensgaard, I.; Nørskov, J. K.; Clausen, B. S.; Topsøe, H.; Besenbacher, F. *Phys. Rev. Lett.* **2000**, *84*, 952.
- (196) Kibsgaard, J.; Lauritsen, J. V.; Lægsgaard, E.; Clausen, B. S.; Topsøe, H.; Besenbacher, F. *J. Am. Chem. Soc.* **2006**, *128*, 13950.
- (197) Lauritsen, J. V.; Kibsgaard, J.; Helveg, S.; Topsøe, H.; Clausen, B. S.; Lægsgaard, E.; Besenbacher, F. *Nat. Nanotechnol.* **2007**, *2*, 53.
- (198) Lauritsen, J. V.; Nyberg, M.; Vang, R. T.; Bollinger, M. V.; Clausen, B. S.; Topsøe, H.; Jacobsen, K. W.; Lægsgaard, E.; Nørskov, J. K.; Besenbacher, F. *Nanotechnology* **2003**, *14*, 283.
- (199) Karunadasa, H. I.; Montalvo, E.; Sun, Y. J.; Majda, M.; Long, J. R.; Chang, C. J. *Science* **2012**, *335*, 698.
- (200) Kobayashi, K.; Yamauchi, J. *Phys. Rev. B* **1995**, *51*, 17085.
- (201) Seo, J. W.; Jun, Y. W.; Park, S. W.; Nah, H.; Moon, T.; Park, B.; Kim, J. G.; Kim, Y. J.; Cheon, J. *Angew. Chem., Int. Ed.* **2007**, *46*, 8828.

- (202) Altavilla, C.; Sarno, M.; Ciambelli, P. *Chem. Mater.* **2011**, *23*, 3879.
- (203) Ataca, C.; Sahin, H.; Ciraci, S. *J. Phys. Chem. C* **2012**, *116*, 8983.
- (204) Mitzi, D. B. *Adv. Mater.* **2009**, *21*, 3141.
- (205) Seo, J. W.; Jang, J. T.; Park, S. W.; Kim, C.; Park, B.; Cheon, J. *Adv. Mater.* **2008**, *20*, 4269.
- (206) Galy, J.; Meunier, G.; Andersson, S.; Astrom, A. *J. Solid State Chem.* **1975**, *13*, 142.
- (207) Makinistian, L.; Albanesi, E. A. *Phys. Rev. B* **2006**, *74*, 045206.
- (208) Lefebvre, I.; Szymanski, M. A.; Olivier-Fourcade, J.; Jumas, J. C. *Phys. Rev. B* **1998**, *58*, 1896.
- (209) Car, R.; Ciucci, G.; Quartapelle, L. *Phys. Status Solidi B* **1978**, *86*, 471.
- (210) Dantas, N. S.; da Silva, A. F.; Persson, C. *Opt. Mater.* **2008**, *30*, 1451.
- (211) Waghmare, U. V.; Spaldin, N. A.; Kandpal, H. C.; Seshadri, R. *Phys. Rev. B* **2003**, *67*, 125111.
- (212) Walsh, A.; Watson, G. W. *Phys. Rev. B* **2004**, *70*, 235114.
- (213) Pannetier, J.; Denes, G. *Acta Crystallogr., Sect. B: Struct. Crystallogr. Cryst. Chem.* **1980**, *36*, 2763.
- (214) Batzill, M.; Diebold, U. *Prog. Surf. Sci.* **2005**, *79*, 47.
- (215) Polatoglu, H. M. *Phys. Rev. B* **1986**, *33*, 5865.
- (216) Makinistian, L.; Albanesi, E. A. *J. Phys.: Condens. Matter* **2007**, *19*, 186211.
- (217) Xue, D. J.; Tan, J. H.; Hu, J. S.; Hu, W. P.; Guo, Y. G.; Wan, L. *J. Adv. Mater.* **2012**, *24*, 4528.
- (218) Jiang, T.; Ozin, G. A. *J. Mater. Chem.* **1998**, *8*, 1099.
- (219) Chang, H.; In, E.; Kong, K. J.; Lee, J. O.; Choi, Y.; Ryu, B. H. *J. Phys. Chem. B* **2005**, *109*, 30.
- (220) Palosz, B.; Steurer, W.; Schulz, H. *Acta Crystallogr. Sect. B* **1990**, *46*, 449.
- (221) Greenaway, D. L.; Nitsche, R. *J. Phys. Chem. Solids* **1965**, *26*, 1445.
- (222) Robertson, J. *J. Phys. C: Solid State Phys.* **1979**, *12*, 4753.
- (223) Lokhande, C. D. *J. Phys. D: Appl. Phys.* **1990**, *23*, 1703.
- (224) Schlaf, R.; Armstrong, N. R.; Parkinson, B. A.; Pettenkofer, C.; Jaegermann, W. *Surf. Sci.* **1997**, *385*, 1.
- (225) Cheng, B.; Russell, J. M.; Shi, W. S.; Zhang, L.; Samulski, E. T. *J. Am. Chem. Soc.* **2004**, *126*, 5972.
- (226) Sharifi, S.; Behzadi, S.; Laurent, S.; Forrest, M. L.; Stroeve, P.; Mahmoudi, M. *Chem. Soc. Rev.* **2012**, *41*, 2323.
- (227) Xu, M. S.; Fujita, D.; Kajiwara, S.; Minowa, T.; Li, X. L.; Takemura, T.; Iwai, H.; Hanagata, N. *Biomaterials* **2010**, *31*, 8022.
- (228) Hanagata, N.; Zhuang, F.; Connolly, S.; Li, J.; Ogawa, N.; Xu, M. S. *ACS Nano* **2011**, *5*, 9326.
- (229) (a) Xu, M. S.; Li, J.; Iwai, H.; Mei, Q. S.; Fujita, D.; Su, H. X.; Chen, H. Z.; Hanagata, N. *Sci. Rep.* **2012**, *2*, 406. (b) Harivardhan Reddy, L.; José, L.; Arias, J. L.; Nicolas, J.; Couvreur, P. *Chem. Rev.* **2012**, *112*, 5818.
- (230) Johnson, J. B.; Jones, H.; Latham, B. S.; Parker, J. D.; Engelken, R. D.; Barber, C. *Semicond. Sci. Technol.* **1999**, *14*, 501.
- (231) Hillhouse, H. W.; Beard, M. C. *Curr. Opin. Colloid Interface Sci.* **2009**, *14*, 245.
- (232) Antunez, P. D.; Buckley, J. J.; Brutchey, R. L. *Nanoscale* **2011**, *3*, 2399.
- (233) Mitzi, D. B.; Kosbar, L. L.; Murray, C. E.; Copel, M.; Afzali, A. *Nature* **2004**, *428*, 299.
- (234) Xu, M. S.; Nakamura, M.; Sakai, M.; Kudo, K. *Adv. Mater.* **2007**, *19*, 371.
- (235) Hickey, G. G.; Waurisch, C.; Rellinghaus, B.; Eychmuller, A. *J. Am. Chem. Soc.* **2008**, *130*, 14978.
- (236) Xu, Y.; Al-Salim, N.; Bumby, C. W.; Tilley, R. D. *J. Am. Chem. Soc.* **2009**, *131*, 15990.
- (237) Franzman, M. A.; Schlenker, C. W.; Thompson, M. E.; Brutchey, R. L. *J. Am. Chem. Soc.* **2010**, *132*, 4060.
- (238) Baumgardner, W. J.; Choi, J. J.; Lim, Y. F.; Hanrath, T. *J. Am. Chem. Soc.* **2010**, *132*, 9519.
- (239) Yoon, S. M.; Song, S. J.; Choi, H. C. *Adv. Mater.* **2010**, *22*, 2164.
- (240) Lai, C. H.; Lu, M. Y.; Chen, L. J. *J. Mater. Chem.* **2012**, *22*, 19.
- (241) Qiu, W. M.; Xu, M. S.; Yang, X.; Chen, F.; Nan, Y. X.; Chen, H. Z. *J. Alloys Compd.* **2011**, *509*, 8413.
- (242) Qiu, W. M.; Xu, M. S.; Yang, X.; Nan, Y. X.; Zhang, J. L.; Chen, H. Z. *CrystEngComm* **2011**, *12*, 4689.
- (243) Whittingham, M. S. *Chem. Rev.* **2004**, *104*, 4271.
- (244) Ji, L. W.; Lin, Z.; Alcoutlabi, M.; Zhang, X. W. *Energy Environ. Sci.* **2011**, *4*, 2682.
- (245) Frumar, M.; Frumarova, B.; Nemec, P.; Wagner, T.; Jedelsky, J.; Hrdlicka, M. *J. Non-Cryst. Solids* **2006**, *352*, 544.
- (246) Liu, R.; Duay, J.; Lee, S. B. *Chem. Commun.* **2011**, *47*, 1384.
- (247) Wang, Q.; O'Hare, D. *Chem. Rev.* **2012**, *112*, 4124.
- (248) Zhang, Y. J.; Lu, J.; Shen, S. L.; Xu, H. R.; Wang, Q. B. *Chem. Comm.* **2011**, *47*, 5226.
- (249) (a) Vaughn, D. D.; Patel, R. J.; Hickner, M. A.; Schaak, R. E. *J. Am. Chem. Soc.* **2010**, *132*, 15170. (b) Li, C.; Huang, L.; Snigdha, G. P.; Yu, Y. F.; Cao, L. Y. *ACS Nano* **2012**, *6*, 8868.
- (250) Vaughn, D. D.; In, S.; Schaak, R. E. *ACS Nano* **2011**, *5*, 8852.
- (251) Kim, T. J.; Kim, C. J.; Son, D. Y.; Choi, M.; Park, B. *J. Power Sources* **2007**, *167*, 529.
- (252) Du, W. M.; Deng, D. H.; Han, Z. T.; Xiao, W.; Bian, C.; Qian, X. F. *CrystEngComm* **2011**, *13*, 2071.
- (253) Zhai, C. X.; Du, L.; Zhang, H.; Yang, D. R. *Chem. Commun.* **2011**, *47*, 1270.
- (254) Luo, B.; Fang, Y.; Wang, B.; Zhou, J. S.; Song, H. H.; Zhi, L. J. *Energy Environ. Sci.* **2012**, *5*, 5226.
- (255) Zhong, H. X.; Yang, G. Z.; Song, H. W.; Liao, Q. Y.; Cui, H.; Shen, P. K.; Wang, C. X. *J. Phys. Chem. C* **2012**, *116*, 9319.
- (256) Brousses, T.; Lee, S. M.; Pasquereau, L.; Defives, D.; Schleich, D. M. *Solid State Ionics* **1998**, *51*, 113.
- (257) Plucinski, L.; Johnson, R. L.; Kowalski, B. J.; Kopalko, K.; Orlowski, B. A.; Kovalyuk, Z. D.; Lashkarev, G. V. *Phys. Rev. B* **2003**, *68*, 125304.
- (258) Depersinge, Y.; Balderesch, A. *Physica* **1981**, *105B*, 324.
- (259) Kamat, P. V.; Meisel, D.; Eds. *Semiconductor Nanoclusters – Physical, Chemical and Catalytic Aspects*; Elsevier: Amsterdam, 1997.
- (260) Shim, M.; Wang, C.; Guyot-Sionnest, P. *J. Chem. B* **2001**, *105*, 2369.
- (261) Fan, Y.; Bauer, M.; Kador, L.; Allakhverdiev, K. R.; Salaev, E. Yu. *J. Appl. Phys.* **2002**, *91*, 1081.
- (262) Depersinge, Y.; Balderesch, A. *Physica* **1981**, *105B*, 324.
- (263) Rak, Zs.; Mahanti, S. D.; Mandal, K. C.; Fernelius, N. C. *J. Phys. Chem. Solids* **2009**, *70*, 344.
- (264) Kuhn, A.; Chevy, A.; Chevalier, R. *Phys. State Solids* **1975**, *82*, 469.
- (265) Schluter, M.; Carnassell, J.; Kohn, S.; Voitchovsky, J. P.; Shen, Y. R.; Cohen, M. L. *Phys. Rev. B* **1976**, *13*, 3534.
- (266) Chikan, V.; Kelley, D. F. *Nano Lett.* **2002**, *2*, 141.
- (267) Allakhverdiev, K. R.; Yetis, M. O.; Özbek, S.; Baykara, T. K.; Salaev, E. Yu. *Laser Phys.* **2009**, *19*, 1092.
- (268) Shi, W.; Ding, Y. J.; Fernelius, N.; Vodopyanov, K. *Opt. Lett.* **2002**, *27*, 1454.
- (269) Aulich, E.; Brebner, J. L.; Mooser, E. *Phys. Status Solidi* **1969**, *31*, 129.
- (270) Ho, C. H.; Lin, S. L. *J. Appl. Phys.* **2006**, *100*, 083508.
- (271) Rybkovskiy, D. V.; Arutyunyan, N. R.; Orekhov, A. S.; Gromchenko, I. A.; Vorobiev, I. V.; Osadchy, A. V.; Salaev, E. Yu.; Baykara, T. K.; Allakhverdiev, K. R.; Obraztsova, E. D. *Phys. Rev. B* **2011**, *84*, 085314.
- (272) Tu, H.; Mogyorosi, K.; Kelley, D. F. *Phys. Rev. B* **2005**, *72*, 205306.
- (273) Peng, H.; Meister, S.; Chan, C. K.; Zhang, X. F.; Cui, Y. *Nano Lett.* **2007**, *7*, 199.
- (274) Gautam, U. K.; Vivekchand, S. R. C.; Govindaraj, A.; Rao, C. N. R. *Chem. Commun.* **2005**, 3995.
- (275) Shen, G.; Chen, D.; Chen, P.; Zhou, C. *ACS Nano* **2009**, *3*, 1115.

- (276) Hua, J. Q.; Band, Y.; Zhan, J. H.; Liu, Z. W.; Golberg, D. *Appl. Phys. Lett.* **2005**, *87*, 153112.
- (277) Kohler, T.; Frauenheim, T.; Hajnal, Z.; Seifert, G. *Phys. Rev. B* **2004**, *69*, 193403.
- (278) Panda, S. K.; Datta, A.; Sinha, G.; Chaudhuri, S.; Chavan, P. G.; Patil, S. S.; More, A. A.; Joag, D. S. *J. Phys. Chem. C* **2008**, *112*, 6240.
- (279) Late, D. J.; Liu, B.; Ramakrishna Matte, S. S.; Rao, C. N. R.; Dravid, V. P. *Adv. Funct. Mater.* **2012**, *22*, 1894.
- (280) Hu, P. A.; Wen, Z. H.; Wang, L. F.; Tan, P. H.; Xiao, K. *ACS Nano* **2012**, *6*, 5988.
- (281) Late, D. J.; Liu, B.; Luo, J. J.; Yan, A. M.; Ramakrishna Matte, H. S. S.; Grayson, M.; Rao, C. N. R.; Dravid, V. P. *Adv. Mater.* **2012**, *24*, 3549.
- (282) Koma, A. *Thin Solid Films* **1992**, *216*, 72.
- (283) Monch, W. *Appl. Phys. Lett.* **1998**, *72*, 1899.
- (284) Wang, W.; Leung, K. K.; Fong, W. K.; Wang, S. F.; Hui, Y. Y.; Lau, S. P.; Chen, Z.; Shi, L. J.; Cao, C. B.; Surya, C. *J. Appl. Phys.* **2012**, *111*, 093520.
- (285) Ueno, K.; Shimada, T.; Saiki, K.; Koma, A. *Appl. Phys. Lett.* **1990**, *56*, 327.
- (286) Koebel, A.; Zheng, Y.; Petroff, J. F.; Boulliard, J. C.; Capelle, B.; Eddrief, M. *Phys. Rev. B* **1997**, *56*, 12296.
- (287) Koma, A.; Yoshimura, Y. *Surf. Sci.* **1986**, *174*, 556.
- (288) Lang, O.; Schlaf, R.; TOMM, Y.; Pettenkofer, C.; Jaegermann, W. *J. Appl. Phys.* **1994**, *75*, 7805.
- (289) Shi, Y. M.; Zhou, W.; Lu, A. Y.; Fang, W. J.; Lee, Y. H.; Hsu, A. L.; Kim, S. M.; Kim, K. K.; Yang, H. Y.; Li, L. J.; Idrobo, J. C.; Kong, J. *Nano Lett.* **2012**, *12*, 2784.
- (290) Hughes, H. P.; Starnberg, H. I. *Electronic Spectroscopies Applied to Low-Dimensional Materials: Physics and Chemistry of Materials with Low-Dimensional Structures*; Kluwer Academic Publishers: Netherland, 2002.
- (291) Parkinson, B. A.; Ohuchi, F. S.; Ueno, K.; Koma, A. *Appl. Phys. Lett.* **1991**, *58*, 472.
- (292) Marchini, S.; Günther, S.; Wintterlin, J. *Phys. Rev. B* **2007**, *76*, 075429.
- (293) Nagashima, A.; Ito, H.; Ichinokawa, T.; Oshima, C. *Phys. Rev. B* **1994**, *50*, 4756.
- (294) Nagashima, A.; Tejima, N.; Gamou, Y.; Kawai, T.; Oshima, C. *Phys. Rev. Lett.* **1995**, *75*, 3918.
- (295) Preobrajenski, A. B.; Vinogradov, A. S.; Martensson, N. *Phys. Rev. B* **2004**, *70*, 165404.
- (296) Durgun, E.; Tongay, S.; Ciraci, S. *Phys. Rev. B* **2005**, *72*, 075420.
- (297) Ding, Y.; Ni, J. *Appl. Phys. Lett.* **2009**, *95*, 083115.
- (298) Lew Yan Voon, L. C.; Sandberg, E.; Aga, R. S.; Farajian, A. A. *Appl. Phys. Lett.* **2010**, *97*, 163114.
- (299) Guzmán-Verri, G. G.; Lew Yan Voon, L. C. *Phys. Rev. B* **2007**, *76*, 075131.
- (300) Wang, S. Q. *Phys. Chem. Chem. Phys.* **2011**, *13*, 11929.
- (301) Liu, C. C.; Feng, W. X.; Yao, Y. G. *Phys. Rev. Lett.* **2011**, *107*, 076802.
- (302) Sheka, E. F. *Int. J. Quantum Chem.* **2012**, DOI: 10.1002/qua.24081.
- (303) Lebègue, S.; Eriksson, O. *Phys. Rev. B* **2009**, *79*, 115409.
- (304) Houssa, M.; Pourtois, G.; Afanas'ev, V. V.; Stesmans, A. *Appl. Phys. Lett.* **2010**, *96*, 082111.
- (305) Houssa, M.; Pourtois, G.; Afanas'ev, V. V.; Stesmans, A. *Appl. Phys. Lett.* **2010**, *97*, 112106.
- (306) De Padova, P.; Quaresima, C.; Olivieri, B.; Perfetti, P.; Le Lay, G. *Appl. Phys. Lett.* **2011**, *98*, 081909.
- (307) Takeda, K.; Shiraishi, K. *Phys. Rev. B* **1989**, *39*, 11028.
- (308) Houssa, M.; Scalise, E.; Sankaran, K.; Pourtois, G.; Afanas'ev, V. V.; Stesmans, A. *Appl. Phys. Lett.* **2011**, *98*, 223107.
- (309) Sofo, J. O.; Chaudhari, A. S.; Barber, G. D. *Phys. Rev. B* **2007**, *75*, 153401.
- (310) Guzmán-Verri, G. G.; Lew Yan Voon, L. C. *J. Phys.: Condens. Matter* **2011**, *23*, 145502.
- (311) Osborn, T. H.; Farajian, A. A.; Pupysheva, O. V.; Aga, R. S.; Lew Yan Voon, L. C. *Chem. Phys. Lett.* **2011**, *511*, 101.
- (312) Zhang, P.; Li, X. D.; Hu, C. H.; Wu, S. Q.; Zhu, Z. Z. *Phys. Lett. A* **2012**, *376*, 1230.
- (313) Wang, X. Q.; Li, H. D.; Wang, J. T. *Phys. Chem. Chem. Phys.* **2012**, *14*, 3031.
- (314) Garcia, J. C.; de Lima, D. B.; Assali, L. V. C.; Justo, J. F. *J. Phys. Chem. C* **2011**, *115*, 13242.
- (315) Morishita, T.; Russo, S. P.; Snook, I. K.; Spencer, M. J. S.; Nishio, K.; Mikami, M. *Phys. Rev. B* **2010**, *82*, 045419.
- (316) Spencer, M. J. S.; Morishita, T.; Snook, I. K. *Nanoscale* **2012**, *4*, 2906.
- (317) Leandri, C.; Le Lay, G.; Aufray, B.; Girardeaux, C.; Avila, J.; Dávila, M. E.; Asensio, M. C.; Ottaviani, C.; Criventi, A. *Surf. Sci.* **2005**, *574*, L9.
- (318) De Padova, P.; Quaresima, C.; Ottaviani, C.; Sheverdyeva, P. M.; Moras, P.; Carbone, C.; Topwal, D.; Olivieri, B.; Kara, A.; Oughaddou, H.; Aufray, B.; Le Lay, G. *Appl. Phys. Lett.* **2010**, *96*, 261905.
- (319) Wintterlin, J.; Bocquet, M. L. *Surf. Sci.* **2009**, *603*, 1841.
- (320) Lalmi, B.; Oughaddou, H.; Enriquez, H.; Kara, A.; Vizzini, S.; Ealet, B.; Aufray, B. *Appl. Phys. Lett.* **2010**, *97*, 223109.
- (321) Vogt, P.; De Padova, P.; Quaresima, C.; Avila, J.; Frantzeskakis, E.; Asensio, M. C.; Resta, A.; Ealet, B.; Le Lay, G. *Phys. Rev. Lett.* **2012**, *108*, 155501.
- (322) Lin, C. L.; Arafune, R.; Kawahara, K.; Tsukahara, N.; Minamitani, E.; Kim, Y.; Takagi, N.; Kawai, M. *Appl. Phys. Express* **2012**, *5*, 045802.
- (323) Chen, L.; Liu, C. C.; Feng, B. J.; He, X. Y.; Cheng, P.; Ding, Z. J.; Meng, S.; Yao, Y. G.; Wu, K. H. *Phys. Rev. Lett.* **2012**, *109*, 056804.
- (324) Jamgotchian, H.; Colignon, Y.; Hamzaoui, N.; Ealet, B.; Hoarau, J. Y.; Aufray, B.; Biberian, J. P. *J. Phys.: Condens. Matter* **2012**, *24*, 172001.
- (325) Chiappe, D.; Grazianetti, C.; Tallarida, G.; Fanciulli, M.; Molle, A. *Adv. Mater.* **2012**, *24*, 5088.
- (326) Enriquez, H.; Vizzini, S.; Kara, A.; Lalmi, B.; Oughaddou, H. *J. Phys.: Condens. Matter* **2012**, *24*, 314211.
- (327) Feng, B. J.; Ding, Z. J.; Meng, S.; Yao, Y. G.; He, X. Y.; Cheng, P.; Chen, L.; Wu, K. H. *Nano Lett.* **2012**, *12*, 3507.
- (328) Fleurence, A.; Friedlein, R.; Ozaki, T.; Kawai, H.; Wang, Y.; Yamada-Yakamura, Y. *Phys. Rev. Lett.* **2012**, *108*, 245501.
- (329) Kim, U.; Kim, I.; Park, Y.; Lee, K. Y.; Yim, S. Y.; Park, J. G.; Ahn, H. G.; Park, S. H.; Choi, H. J. *ACS Nano* **2011**, *5*, 2176.
- (330) Nakano, H.; Mitsuoka, T.; Harada, M.; Horibuchi, K.; Nozaki, H.; Takahashi, N.; Nonaka, T.; Seno, Y.; Nakamura, H. *Angew. Chem.* **2006**, *118*, 6451.
- (331) Okamoto, H.; Kumai, Y.; Sugiyama, Y.; Mitsuoka, T.; Nakanishi, K.; Ohta, T.; Nozaki, H.; Yamaguchi, S.; Shirai, S.; Nakano, H. *J. Am. Chem. Soc.* **2010**, *132*, 2710.
- (332) Sugiyama, Y.; Okamoto, H.; Mitsuoka, T.; Morikawa, T.; Nakanishi, K.; Ohta, T.; Nakano, H. *J. Am. Chem. Soc.* **2010**, *132*, 5946.
- (333) Sahin, H.; Cahangirov, S.; Topsakal, M.; Bekaroglu, E.; Akturk, E.; Senger, R. T.; Ciraci, S. *Phys. Rev. B* **2009**, *80*, 155453.
- (334) Bekaroglu, E.; Topsakal, M.; Cahangirov, S.; Ciraci, S. *Phys. Rev. B* **2009**, *81*, 075433.
- (335) Pan, L.; Liu, H. J.; Wen, Y. W.; Lv, H. Y.; Shi, J.; Tang, X. F. *Phys. Lett. A* **2011**, *375*, 614.
- (336) Xiao, W. Z.; Wang, L. L.; Xu, L.; Wan, Q.; Pan, A. L.; Deng, H. Q. *Phys. Status Solidi B* **2011**, *248*, 1442.
- (337) Hsueh, H. C.; Guo, G. Y.; Louie, S. G. *Phys. Rev. B* **2011**, *84*, 085404.
- (338) Lin, S. S. *J. Phys. Chem. C* **2012**, *116*, 3951.
- (339) Kane, B. E. *Nature* **1998**, *393*, 133.
- (340) Gunawan, O.; Shkolnikov, Y. P.; Vakili, K.; Gokmen, T.; De Poortere, E. P.; Shayegan, M. *Phys. Rev. Lett.* **2006**, *97*, 186404.
- (341) Xiao, D.; Yao, W.; Niu, Q. *Phys. Rev. Lett.* **2007**, *99*, 236809.
- (342) Xiao, D.; Liu, G. B.; Feng, W.; Xu, X. D.; Yao, W. *Phys. Rev. Lett.* **2012**, *108*, 196802.
- (343) Cao, T.; Feng, J.; Shi, J.; Niu, Q.; Wang, E. *arXiv* 1112.4013.

- (344) Yao, W.; Xiao, D.; Niu, Q. *Phys. Rev. B* **2008**, *77*, 235406.
- (345) Zeng, H. L.; Dai, J. F.; Yao, W.; Xiao, D.; Cui, X. D. *Nature Nanotechnol* **2012**, *7*, 490.
- (346) Mak, K. F.; He, K. L.; Shan, J.; Heinz, T. F. *Nature Nanotechnol* **2012**, *7*, 494.
- (347) Zhu, Z. Y.; Cheng, Y. C.; Schwingenschlogl, U. *Phys. Rev. B* **2011**, *84*, 153402.
- (348) Cheiwchanwannagij, T.; Lambrecht, W. R. L. *Phys. Rev. B* **2012**, *84*, 205302.
- (349) Ni, Z. Y.; Liu, Q. H.; Tang, K. C.; Zheng, J. X.; Zhou, J.; Qin, R.; Gao, Z. X.; Yu, D. P.; Lu, J. *Nano Lett.* **2012**, *12*, 113.
- (350) Qi, X. L.; Zhang, S. C. *Rev. Mod. Phys.* **2011**, *83*, 1057.
- (351) Kane, C. L.; Mele, E. J. *Phys. Rev. Lett.* **2005**, *95*, 226801.
- (352) Bernevig, B. A.; Hughes, T. L.; Zhang, S. C. *Science* **2006**, *314*, 1757.
- (353) König, M.; Wiedmann, S.; Brüne, C.; Roth, A.; Buhmann, H.; Molenkamp, L. W.; Qi, X. L.; Zhang, S. C. *Science* **2007**, *318*, 766.
- (354) Hasan, M. Z.; Kane, C. L. *Rev. Mod. Phys.* **2010**, *82*, 3045.
- (355) Moore, J. E. *Nature* **2010**, *464*, 194.
- (356) Qi, X. L.; Zhang, S. C. *Phys. Today* **2010**, *63*, 33.
- (357) Min, H.; Hill, J. E.; Sinitsyn, N. A.; Sahu, B. R.; Kleinman, L.; MacDonald, A. H. *Phys. Rev. B* **2006**, *74*, 165310.
- (358) Drummond, N. D.; Zólyomi, V.; Fal'ko, V. I. *Phys. Rev. B* **2012**, *85*, 075423.
- (359) Ezawa, M. *New J. Phys.* **2012**, *14*, 033003.
- (360) Britnell, L.; Gorbachev, R. V.; Jalil, R.; Belle, B. D.; Schedin, F.; Mishchenko, A.; Georgiou, T.; Katsnelson, M. I.; Eaves, L.; Morozov, S. V.; Peres, N. M. R.; Leist, J.; Geim, A. K.; Novoselov, K. S.; Ponomarenko, L. A. *Science* **2012**, *335*, 947.
- (361) Ismach, A.; Chou, H.; Ferrer, D. A.; Wu, Y.; McDonnell, S.; Floresca, H. C.; Covacevich, A.; Pope, C.; Piner, R.; Kim, M. J.; Wallace, R. M.; Colombo, L.; Ruoff, R. S. *ACS Nano* **2012**, *6*, 6378.
- (362) (a) Ji, H.; Hao, Y.; Ren, Y.; Charlton, M.; Lee, W. H.; Wu, Q.; Li, H.; Zhu, Y.; Wu, Y.; Piner, R.; Ruoff, R. S. *ACS Nano* **2011**, *5*, 7656. (b) Wan, X.; Chen, K.; Liu, D. Q.; Chen, J.; Miao, Q.; Xu, J. B. *Chem. Mater.* **2012**, *24*, 3906.
- (363) Sutter, P.; Lahiri, J.; Zahl, P.; Wang, B.; Sutter, E. *Nano Lett.* [10.1021/nl304080y](https://doi.org/10.1021/nl304080y).
- (364) Du, Y. P.; Yin, Z. Y.; Rui, X. H.; Zeng, Z. Y.; Wu, X. J.; Liu, J. Q.; Zhu, Y. Y.; Yan, Q. Y.; Zhang, H. *Nanoscale* [10.1039/C2NR3458E](https://doi.org/10.1039/C2NR3458E).
- (365) De, D.; Manongdo, J.; See, S.; Zhang, V.; Guloy, A.; Peng, H. B. *Nanotechnology* **2013**, *24*, 025202.
- (366) Zeng, Z. Y.; Sun, T.; Zhu, J. X.; Huang, X.; Yin, Z. Y.; Lu, G.; Fan, Z. X.; Yan, Q. Y.; Hng, H. H.; Zhang, H. *Angew. Chem. Int. Ed.* **2012**, *51*, 9052.
- (367) Li, H.; Lu, G.; Wang, Y. L.; Cong, C. X.; He, Q. Y.; Wang, L.; Ding, F.; Yu, T.; Zhang, H. *Small* [10.1002/smll.201202919](https://doi.org/10.1002/smll.201202919).
- (368) Gutiérrez, H. R.; Perea-López, N.; Elías, A. L.; Berkdemir, A.; Wang, B.; Lv, R.; López-Urías, F.; Crespi, V. H.; Terrones, H.; Terrones, M. *Nano Lett.* [10.1021/nl3026357](https://doi.org/10.1021/nl3026357).
- (369) (a) Liu, J. Q.; Zeng, Z. Y.; Cao, X. H.; Lu, G.; Wang, L. H.; Fan, Q. L.; Huang, W.; Zhang, H. *Small* **2012**, *8*, 3517. (b) Yin, Z. Y.; Zeng, Z. Y.; Liu, J. Q.; He, Q. Y.; Chen, P.; Zhang, H. *Small* [10.1002/smll.201201940](https://doi.org/10.1002/smll.201201940).
- (370) Mak, K. F.; He, K.; Lee, C.; Lee, G. H.; Hone, J.; Heinz, T. F.; Shan, J. *Nat. Mater.* [10.1038/NMAT3035](https://doi.org/10.1038/NMAT3035).
- (371) Woo Jong Yu, W. J.; Li, Z.; Zhou, H. L.; Chen, Y.; Wang, Y.; Huang, Y.; Duan, X. F. *Nat. Mater.* [10.1038/NMAT3518](https://doi.org/10.1038/NMAT3518).
- (372) Wang, O.; Kalantar-Zadeh, K.; Kis, A.; Coleman, J. N.; Strano, M. S. *Nat. Nanotechnol.* **2012**, *7*, 699.
- (373) Quhe, R.; Fei, R.; Liu, Q.; Zheng, J.; Li, H.; Xu, C.; Ni, Z.; Wang, Y.; Yu, D.; Gao, Z.; Lu, J. *Sci. Rep.* **2012**, *2*, 853.
- (374) Chen, L.; Li, H.; Feng, B. J.; Ding, Z. J.; Qiu, J. L.; Cheng, P.; Wu, K. H.; Meng, S. [arXiv:1212.3679](https://arxiv.org/abs/1212.3679).

NOTE ADDED IN PROOF

Low-pressure CVD growth of layer-controlled *h*-BN sheets was reported.³⁶¹ In contrast to CVD method, physical vapor

deposition (PVD) techniques, such as magnetron sputtering and electron beam evaporation, were exploited to synthesize graphene^{89e,362} and *h*-BN layers.³⁶³

A facile, environmentally friendly, and economical route for large-amount synthesis of 2D SnS₂ nanoplates and the use of such nanoplates as the electrode of lithium-ion battery were reported.³⁶⁴

FETs based on mechanically exfoliated SnS₂ nanosheets on SiO₂ platform was reported to exhibit *n*-type behavior with an on/off ratio exceeding 2×10^6 and a carrier mobility of approximately $1 \text{ cm}^2 \text{ V}^{-1} \text{ s}^{-1}$.³⁶⁵

NbSe₂, WSe₂, *h*-BN as well as Sb₂Se₃ and Bi₂Te₃ were prepared from their layered bulk precursors by using an electrochemical lithium intercalation process.³⁶⁶ Few-layer TaS₂ and TaSe₂ nanosheets were prepared by mechanical exfoliation.³⁶⁷

Monolayer triangular WS₂ sheets synthesized by sulfurization of the WO₃ films exhibited room-temperature PL and enhancement of PL towards the edges of triangular platelets was observed.³⁶⁸

Memory devices based on nanocomposites of MoS₂ with graphene oxide or polyvinylpyrrolidone were demonstrated.³⁶⁹

Without analogue in conventional semiconductors, tightly bound negative trions, a quasiparticle composed of two electrons and a hole, was identified in monolayer MoS₂ FETs. These quasiparticles possess a large binding energy, approximately 20 meV, which is nearly an order of magnitude larger than that found in conventional quasi-2D systems.³⁷⁰

Vertically stacked multi-heterostructures comprising of graphene, few-layer MoS₂ (*n*-type), metal films, and Bi₂Sr₂Co₂O₈ (*p*-type) were fabricated.³⁷¹

A review article related to TMD with emphasis on MoS₂ was recently published.³⁷²

DFT calculations showed that an impressive maximum band gap up to 0.50 eV can be opened by controlling adsorption coverage of alkali atoms on one-side surface of silicene, and on/off current ratio up to 10^8 can be obtained from a bottom-gated FET using a sodium-covered silicene as the active channel based on ab initio quantum transport simulation.³⁷³

Intriguing physics, which is unique to silicene but not ever found in graphene, was reported.³⁷⁴ The $\sqrt{3} \times \sqrt{3}$ superstructure of silicene on Ag(111) was observed to undergo a phase transition to two mirror-symmetric rhombic phases at temperature below 40 K by STM, which is due to the weak van der Waals interactions between the silicene and the Ag(111) substrate according to first-principles calculations.

NOTE ADDED AFTER ASAP PUBLICATION

This paper was published to the Web on January 3, 2013, with an error in the caption of Figure 14. This was corrected in the version published on January 17, 2013.